DENGUE RAPID DIAGNOSTICS VIA SURFACE PLASMON RESONANCE BIOSENSOR

PEYMAN JAHANSHAHI

THESIS SUBMITTED IN FULFILMENT OF THE REQUIREMENTS
FOR THE DEGREE OF DOCTOR OF PHILOSOPHY

FACULTY OF ENGINEERING
UNIVERSITY OF MALAYA
KUALA LUMPUR
2015

UNIVERSITI MALAYA

ORIGINAL LITERARY WORK DECLARATION

Name of Candidate: Peyman Jahanshahi (I.C/Passport No:
Registration/Matric No: KHA100120
Name of Degree: DOCTOR OF PHILOSOPHY
Title of Project Paper/Research Report/Dissertation/Thesis ("this Work"):

Dengue Rapid Diagnostics via Surface Plasmon Resonance Biosensor

Field of Study: Photonic (Electronics and Automation)
I do solemnly and sincerely declare that:

(1) I am the sole author/writer of this Work;
(2) This Work is original;
(3) Any use of any work in which copyright exists was done by way of fair dealing and for permitted purposes and any excerpt or extract from, or reference to or reproduction of any copyright work has been disclosed expressly and sufficiently and the title of the Work and its authorship have been acknowledged in this Work;
(4) I do not have any actual knowledge nor do I ought reasonably to know that the making of this work constitutes an infringement of any copyright work;
(5) I hereby assign all and every rights in the copyright to this Work to the University of Malaya ("UM"), who henceforth shall be owner of the copyright in this Work and that any reproduction or use in any form or by any means whatsoever is prohibited without the written consent of UM having been first had and obtained;
(6) I am fully aware that if in the course of making this Work I have infringed any copyright whether intentionally or otherwise, I may be subject to legal action or any other action as may be determined by UM.

Candidate's Signature Date

Subscribed and solemnly declared before,

Witness's Signature Date
Name:
Designation:

Dedication

I dedicate this curriculum to my wife,

MANIYA

, who did more than her share around the house as I sat at the computer. Without her tireless love, support, and patience, I could not really enjoy my scientific researches and complete my PhD.

ABSTRACT

The aim of this thesis is to introduce an optical technique which can be utilized in detection of dengue virus rapidly. This technique involves the application of analytical and numerical electromagnetic simulations led by physical insight and theoretical knowledge. As a part of this study, the most common permittivity function models are compared and the best model is identified for the proposed biosensor structure. The best model (Brendel-Bormann) is found to have an accuracy of ~94.4% with respect to experimental data. On the other hand, Finite Element Method (FEM) is found to be a valuable tool in the numerical solutions of the proposed biosensor structure throughout this thesis.

Beside of simulation, the experiment is implemented through the Biacore device which is based on the surface plasmon resonance (SPR) technique. According to the experimental results, a serum volume of only 1 μl from a dengue patient (as a minimized volume) is required to determine the ratio of each dengue serotype in samples with 83-93% sensitivity and 100% specificity.

The Biacore device is considered in an effort to demonstrate a rapid diagnostic test of dengue virus and the application of the intended technique in this detection. An immobilization of dengue antigen is properly performed on the chip surface, and all samples in four serotypes of dengue virus are examined through the chip. Beside the determination of sensitivity and specificity of our detection method, an optimization of sample volume is studied with different concentrations of samples. In addition, the theoretical calculations are validated in comparison with experimental results. According to the sample from each category of dengue serotypes 2 (low, mid, and highly positive), the error ratio of ~5.35%, 6.54%, and 3.72% is obtained at the end.

ABSTRAK

Tujuan tesis ini adalah untuk memperkenalkan teknik optik yang boleh digunakan dalam mengesan virus denggi dengan cepat. Teknik ini melibatkan penggunaan simulasi elektromagnet dan analisis berangka yang diterajui oleh wawasan fizikal dan pengetahuan teori. Sebagai sebahagian daripada kajian ini, pelbagai model fungsi ketelusan telah dibandingkan dan model yang terbaik untuk struktur biosensor dikenalpasti. Model tersebut (Brendel-Bormann) menunjukkan ketepatan ~ 94.4% dibandingkan dengan data eksperimen. Selain itu, didapati bahawa Kaedah Unsur Terhingga (KUT) merupakan kaedah yang bernilai dalam penyelesaian berangka struktur biosensor yang dicadangkan di seluruh tesis ini.

Selain daripada simulasi, eksperimen yang dilaksanakan melalui peralatan Biacore berdasarkan teknik plasmon resonans permukaan. Menurut hasil kajian, hanya 1 μl isipadu serum daripada pesakit denggi (jumlah minimum) diperlukan untuk menentukan nisbah setiap serotype denggi dalam sampel dengan kepekaan 83-93% dan penkhususan 100%.

Biacore telah dipertimbangkan dalam usaha kami untuk mendemonstrasikan ujian diagnostik yang cepat untuk pengesanan virus denggi. Pernahanan antigen denggi dilaksanakan di atas permukaan cip, dan semua sampel yang mengandungi empat serotype virus denggi akan diteliti melalui cip. Selain menentukan kepekaan dan pengkhususan bagi kaedah pengesanan kami, pengoptimuman isipadu sampel telah dikaji dengan kepekatan yang berbeza sampel. Di samping itu, pengiraan teori telah disahkan melalui perbandingan dengan keputusan eksperimen. Menurut sampel dari setiap kategori serotype denggi 2 (rendah, pertengahan, dan sangat positif), nisbah ralat sekitar ~ 5.35%, 6.54% dan 3.72% diperolehi.

ACKNOWLEDGEMENTS

I would like to express my deep gratitude and appreciation to my supervisor, Professor Dr. Faisal Rafiq Mahamd Adikan for his valuable guidance, support and encouragement in both my academic work and life in general. I consider myself fortunate to have had the chance to learn from such an excellent mentor.

I would like to thank the Integrated Lightwave Research Group previously known as Photonics Research Group (especially Mostafa Ghomeishi, Saleh Seyedzadeh, Syed Reza Sandoghchi) that helped me during my PhD. I would also like to thank the University of Malaya High Impact Research Grant (MOHE-HIRG A000007-50001) at UM for funding research and tuition fees.

I am very thankful to Professor Dr. Shamala Devi Sekaran from Faculty of Medicine, UM, my research advisor, for all of her patience, and for her guidance in my research work and other matters. I have very much enjoyed working and collaborating with her and her group (especially Ms. Adeline Yeo Kin Lian) for assisting in laboratorial works.

Finally, I cannot thank my family enough. Shamsi and Mohammad Jalil, my dear parents / Zahra and Mohammad Hadi, my dear parents in-law, my dear brothers (Mahdi, Kamran, and Pooriya), my dear sisters (Zahra, Nadiya and Shima), without your continuous love and encouragement, I never could have accomplished my dreams. I can only say that I love you with all my heart. Meanwhile, welcome to Saniya, my daughter, that has been born recently. My life would be incomplete without the blessing of your continuous patience, support, and love.

Thanks you, Almighty God, for giving me all these wonderful people in my life.

LIST OF CONTENTS

LIST OF TABLES

LIST OF FIGURES

LIST OF SYMBOLS

Ab	Antibody
ADE	Antibody-Dependent Enhancement
AFM	Atomic Force Microscopy
Ag	Antigen
ATR	Attenuated Total Reflection
ATR	Attenuated Total Reflection
B	Magnetic-Flux Density
B-B	Brendel Bormann Model
D	Drude Model
D	Flux Density
DF	Dengue Fever
DHF	Dengue Hemorrhagic Fever
D-L	Drude-Lorentz Model
DMD	Dielectric-Metal-Dielectric
DSS	Dengue Shock Syndrome
E	Electric Field
EELS	Electron Energy Loss Spectrometry
EIM	Effective Index Method
ELISA	Enzyme-Linked Immune-Sorbent Assay
EM	Electromagnetic
FDTD	Finite-Difference Time-Domain
FEM	Finite Element Method
H	Magnetic Field
HC	Hepatitis C
HCT	Hematocrit

IgG	Immunoglobulin G
IgM	Immunoglobulin M
MDM	Metal- Dielectric-Metal
M-O	Multi Oscillator Model
NS1	Non Structural protein 1
PCR	Polymerase Chain Reaction
POC	Point of Care
R	Reflectance
RDTs	Rapid Diagnostic Tests
RU	Resonance Units
S	Poynting vector
SEM	Scanning Electron Microscopy
SP	Surface Plasmon
SPP	Surface Plasmon Polariton
SPR	Surface Plasmon Resonance
TBE	Tick-Borne Encephalitis
TE	Transverse Electric
TEM	Transmission Electron Microscope
TM	Transverse Magnetic
WHO	World Health Organization
ε	Dielectric Constant
μ	Magnetic Permeability

1 CHAPTER I: INTRODUCTION

1.1 Introduction

Infectious diseases or communicable diseases are caused by the presence of pathogenic microorganisms, such as bacteria, viruses, fungi or parasites. The diseases can be spread, directly or indirectly, from one person to another (Cheesbrough, 2006). The disease transmission may occur through one or more of diverse pathways including physical contact with infected individuals. These infecting agents may also be transmitted through liquids, food, body fluids, contaminated objects, airborne inhalation, or through vector-borne spread. The dominant cases of infectious diseases include lower respiratory infections, HIV/AIDS, Tetanus and tropical diseases such as dengue fever, malaria, and tuberculosis(Lim, 2009; Mathers, Fat, & Boerma, 2008).

Dengue and dengue hemorrhagic fever (DHF) are caused by one of four closely related, but antigenically distinct, virus serotypes (DEN-1, DEN-2, DEN-3, and DEN-4), of the genus *Flavivirus* (Gubler & Clark, 1995). Infection with one of these serotypes does not cross-protect, so persons living in a dengue-endemic area can have up to four dengue infections during their lifetimes. Dengue is an urban disease of the tropics and subtropics, and its causative agent can be maintained in a cycle that involves humans and its vectors (*Aedes aegypti* and *aedes albopictus*). Dengue has been chosen as the test bed for this project as it is one of the local and emerging diseases in the tropical and subtropical regions with high fatality rate (Dutra, de Paula, de Oliveira, de Oliveira, & De Paula, 2009). Infection with a dengue virus can generate a spectrum of clinical sickness from non-specific viral syndromes to critical and fatal hemorrhagic illness. Significant risk factors for DHF consist of the strain and the virus serotype involved, immune status, genetic predisposition, and age of the patient (Bhatt et al., 2013).

There is an annual report that estimated hundred million cases of the dengue fever (DF) and 250,000 - 500,000 cases of the DHF with the average case fatality rate being 5% in the world (Guzman et al., 2010; Honório et al., 2009). The half of world's population lives in zones with high risk of dengue infection and these zones are common destinations as well. The world's population is estimated to be 8.3 billion on 2025 with the increase happening in urban settlements. This has caused an unplanned and uncontrolled urbanization of the developing countries particularly in tropical areas (D. S. Shamala, 2005). The first case of occurred dengue epidemic was reported in 1779-1780 in Asia, Africa, and North America (Gubler & Clark, 1995).

In the latest report 2013, national and subnational evidence consensus on complete absence (green) through to complete presence (red) of dengue (Figure 1.1 (a)), probability of dengue occurrence at 5 km × 5 km spatial resolution of the mean predicted map from 336 boosted regression tree models (Figure 1.1 (b) and (c)) cartogram of the annual number of infections for all ages as a proportion of national or subnational (China) geographical area (Figure 1.1 (c)) are presented (Bhatt et al., 2013).

Malaysia is one of the tropical countries with notably high mortality and morbidity cases of tropical diseases especially of dengue fever. The Dengue virus is a typical tropical disease because the mosquitos that carry the virus require a warm and hot climate (Special Programme for Research, Training in Tropical Diseases, 2009).

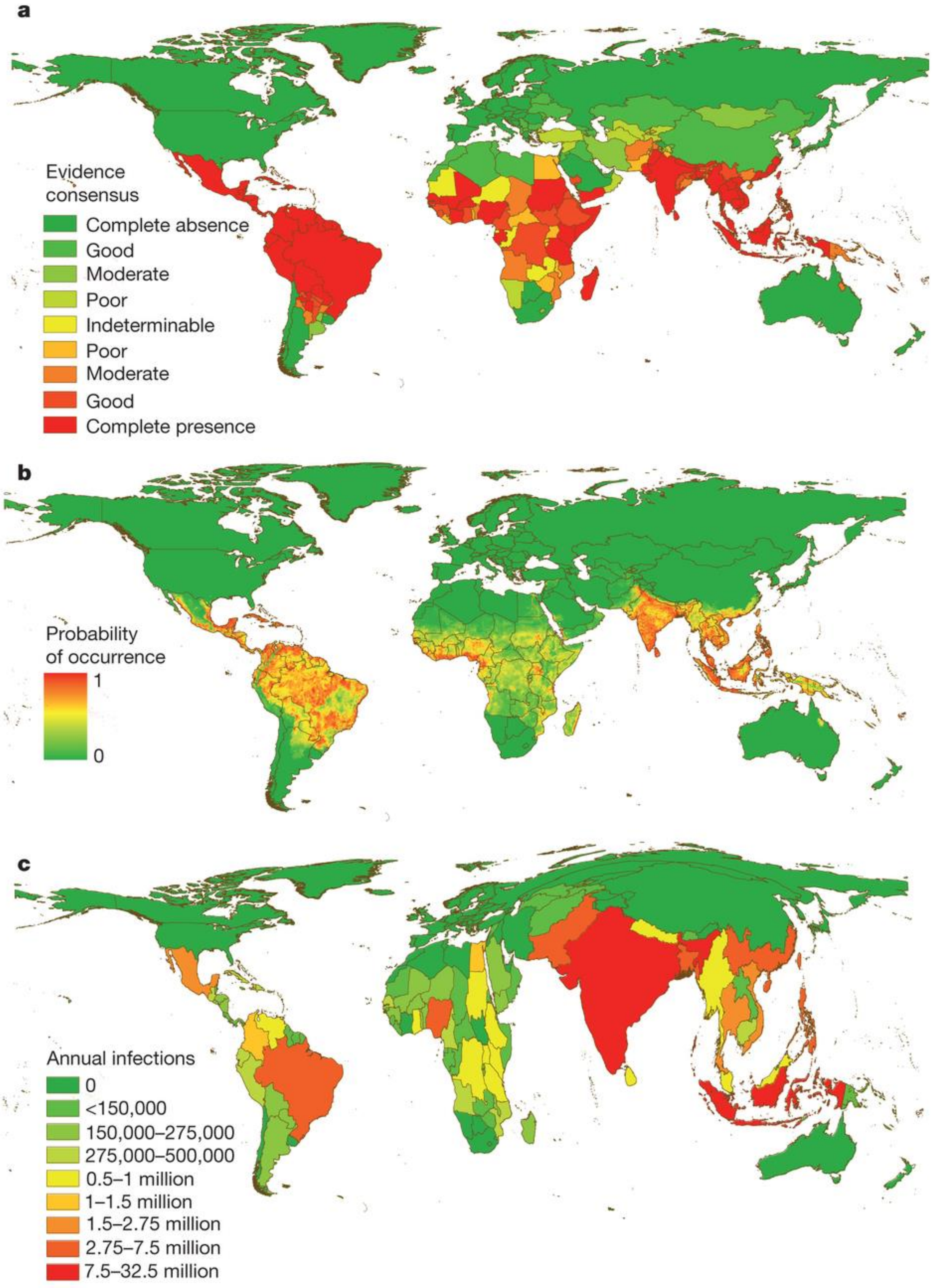

Figure 1.1 Global evidence consensus, risk and burden of dengue in 2010. Courtesy (Bhatt et al., 2013)

In 1902, the first case of dengue fever in Malaysia was reported through the dengue outbreak in Penang by Skae. More reports were published on dengue outbreaks in numerous states of Peninsular Malaysia mostly in large cities and ports in 1904, 1932 and

1933 subsequently (D. S. Shamala, 2005). For the first time, the dengue virus was isolated by Smithburn in 1950. In 1953, the laboratory confirmation was first performed by the Institute of Medical Research in Malaysia. Since that time, the pockets of outbreaks began to appear in urban zones of Peninsular Malaysia, and the dengue fever is become a notifiable disease in this tropical region. From then on increasing the numbers of dengue patient were recorded in Malaysia (D. S. Shamala, 2005; D. Shamala, 2008).

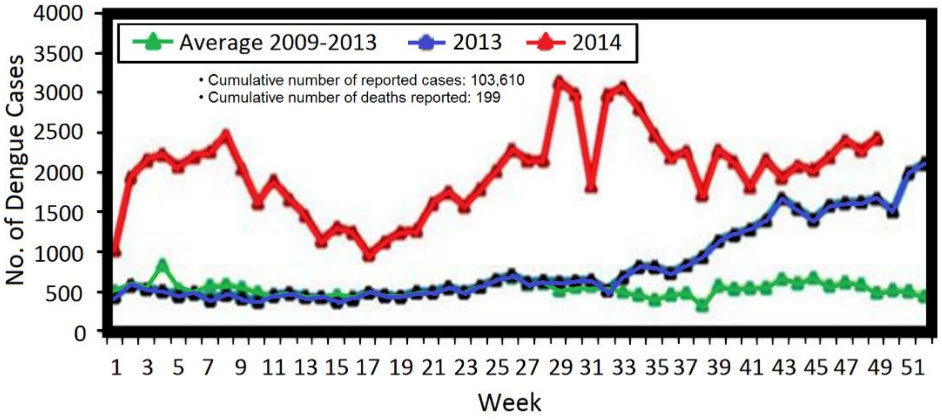

Figure 1.2 Number of dengue cases by week, Department of Health, Malaysia

According to the latest report as of 20th December 2014 (reported by WHO), the number of dengue cases in Malaysia is still higher than for the same period in 2013. There has been an increase of 16.4% in the number of reported new cases compared with the previous week (Figure 1.2).

1.2 Research background

Dengue fever and its more serious forms, dengue hemorrhagic fever and dengue shock syndrome (DSS), are becoming important public health problems and were formally included within the disease portfolio of the of World Health Organization (WHO) special program for research and training in tropical disease by the Joint Coordination Board in June 1999. The global prevalence of dengue has grown dramatically in recent decades (Lee, 2008; Shu & Huang, 2004). According to the WHO, around 3.6 billion people are now at risk from Dengue (Dussart et al., 2008; Guzman et al., 2010; Organization & others, 2011; Osman, Fong, & Devi, 2007). Currently, the disease is endemic in over 100 tropical and sub-tropical countries and it is estimated that there are 390 million cases of Dengue infections worldwide every year (Bhatt et al., 2013; Murray, Quam, & Wilder-Smith, 2013).

Dengue infection may be without symptoms or cause to a series of clinical presentations even in death level. Its incubation period is 4 to 7 days in the range of 3 to 14 days. The clinical symptoms consist of an itchy rash, nausea, sudden onset of fever, muscle and joint pain, depression, frontal headache, weakness, vomiting and retro-orbital pain (Figure 1.3). The feverish painful period of dengue fever continues 5 to 7 days, and may leave the tired feeling in dengue patients for more than expected days (Rigau-Pérez et al., 1998; D. S. Shamala, 2005).

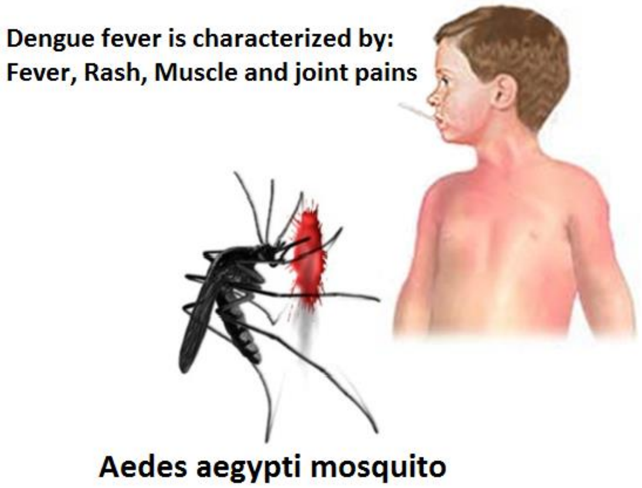

Figure 1.3 Characterization of dengue fever

DSS is the most serious form and is specified as DHF with symptoms of frank shock, circulatory failure, hypotension, and narrowing pulse pressure. The expansion of these kinds of symptoms or any sign of hypotension presents the indications for hospital admission and then managing patient. Prognosis is related to the prevention or rapid diagnosis, and after that treatment of shock. According to the experience of specialists, the case fatality rate (CFR) can be as low as 0.2% in hospitals. Once shock has appointed in the CFR, it may be as high as 12 to 44%. There have been some uncommon but well described indications of dengue fever like dengue infection with severe haemorrhage, liver injuries, encephalopathy, and cardiomyopathy that the risk of death is high. Neurological indications such as convulsions, altered consciousness, and coma have been also reported (Ranjit & Kissoon, 2011; Rigau-Pérez et al., 1998; D. S. Shamala, 2005).

The risk of DHF is higher when two or more viruses circulate at the same time. In addition, the presence of dengue antibodies obtained either actively by previous infection or passive by maternal antibodies in the milk or in the uterus are some of the contributing factors. Therefore antibodies actually enhance viral infectivity in the non-neutralising concentrations. This assumption is termed by antibody-dependent enhancement (ADE) is the process in which the virus is mixture with specific antibodies to enhance its absorption by mononuclear cells (the primary part for replicating virus). The replication of the virus in these cells affects the release of vasoactive mediators that increases vascular permeability and the hemorrhagic symptoms that can observe in DHF (Rigau-Pérez et al., 1998). But this assumption is inconsistent as there is a small but unanimous percentage of the DHF/DSS cases which are caused by the primary infections. There is no pre-existing antibodies in these persons (D. S. Shamala, 2005).

1.2.1 Laboratory Diagnosis

Conventional methods as laboratory diagnosis and rapid diagnostic tests (RDTs) are two significant categories for use in biomedical diagnostics. For the laboratory diagnosis of dengue fever as a common way, when a patient is suspected with dengue, he/she has to go to a hospital to get a battery of diagnostic tests which require expensive equipment and expertise which is not necessarily available if the patient came from a rural background. The test is usually done in batches and results typically take time around 3-

7 days. By that time, the patient might be in critical stage and may not be referred to the hospital on time for optimum clinical management (Rigau-Pérez et al., 1998).

Dengue virus belongs to the family *Flaviviridae*, a family which consists of around 70 viruses that have a cross-react in the serological tests. Since those share the blood group antigens, therefore there is a complicating diagnosis. The laboratory diagnosis is dependent upon the virus isolation and the serologic tests. There is a circulating virus that remains detectable in blood during a feverish period after which those are recognized and then cleared rapidly with appearance of the specific antibody. The virus isolation is performed using the mosquito cell line. After a few days incubation, the virus is detected through an indirect fluorescent antibody test.

The serological diagnosis is dependent on the presence of the immunoglobulin M (IgM) antibodies or an increase in the immunoglobulin G (IgG) antibodies in paired acute and convalescent phase serum. Over 90% of patients have the IgM positive test by the 4th day of sickness, but the IgM antibodies may be due to infection up to three months earlier. The commercial biochemical kits for the measurement of antibodies contain the enzyme-linked immune-sorbent assay (ELISA), dipstick, and rapid dot blot tests. There is not necessary to require a specialized training for these tests, but their specificity and sensitivity are not steady state, reliable, and mainly low. It is true that the specificities of ELISA kits are almost 100%, but the sensitivities of these kits have been examined around 87–90%. In rapid diagnostic tests, the sensitivity is in the range of 75–80% while these types of rapid tests have not significantly enough specificity to distinguish between cross-reactivity in the serological tests (Wang & Sekaran, 2010).

The polymerase chain reaction (PCR) is a biochemical method in the molecular biology used to replicate a single or a few pieces of the DNA upon several orders of magnitude, producing the millions of identical copies of a unique DNA sequence. The multiplex PCR which was developed at the University of Malaya Medical Centre, is capable to detect the serotype of virus detection in an approximate time 3-4 hours with ~75% sensitivity. The real time multiplex test that is capable to detect the dengue serotype and viral RNA quantity, can examine a patient sample within an approximate time of two and half hours with sensitivity ~89%. Both tests can be developed to amplify a virus RNA from the onset of the infection. The detection of NS1 protein has been presented by few researchers that show an applicable assay within acute phase of an illness (D. S. Shamala, 2005; Yager, Domingo, & Gerdes, 2008).

It is true that the use of PCR technique may make to detect in the short time with significantly high sensitivity and specificity, but this technique cannot be applicable when the virus is completely gone in patient blood. In this phase, detection is performed through the anti-virus existing in the blood (Fatemeh et al., 2014; Ramirez et al., 2009; Sabatino, Botto, Borghini, Turchi, & Andreassi, 2013; D. S. Shamala, 2005).

Currently few commercial kits are available for dengue detection, but all kits need to be extensively validated to assess their role in routine dengue diagnosis (Hunsperger et al., 2009). Hence with these assays available it appears that two or more assays have to be done to ensure maximal detection of the disease which yearly results in sporadic outbreaks. The number of cases in the country warrants the need for diagnosis not only to be precise but also sensitive and be able to diagnose with just one sample. The cost of individual assays as well as confirmation makes this disease an expensive one to diagnose. There are a lot of techniques to detect either virus specific proteins or antibodies, but those can detect intact viral particles rarely. The ELISA is one of the most conventional techniques for detection of viruses and viral specific antigens (Nunes et al., 2011; He et al., 2009; Young, Hilditch, Bletchly, & Halloran, 2000).

The ELISA technique (Duzgun, Schuntner, Wright, Leatch, & Waltisbuhl, 1988), however, has some limitations, such as cannot distinguish the source of antigen directly, and needs laboratory sequential steps to detect the viruses. These steps consist of injection some solutions to samples, incubation times, and keeping samples to specific temperature (Figure 1.4).

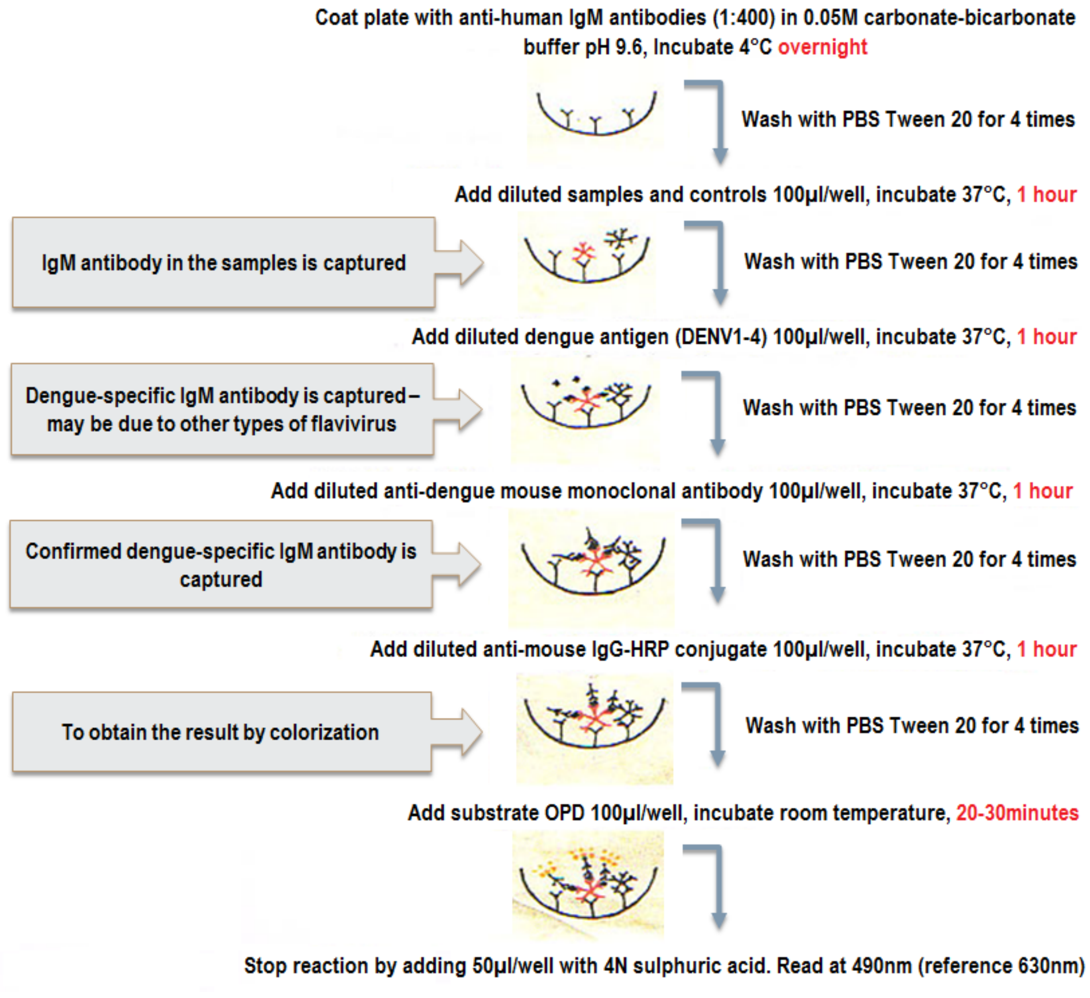

Figure 1.4 Flowchart of dengue IgM capture enzyme linked imunosorbent assay method

The manifestation of the dengue disease is complex; however, the treatment of the disease can be simple, inexpensive and effective as long as correct and early detection is performed. This can only be achieved if understanding of the clinical problems and the phases of the disease is known especially when patients are first seen and evaluated through triage. Triage is a process of screening suspected patients to identify the severity of the dengue patient's condition. For proper management of the disease, a full blood count should be done at the first visit or triage. While a hematocrit (HCT) test establishes the patient's own baseline, a decreasing white blood cell count indicates high likelihood of dengue. A rapid decrease in platelet with rising HCT suggests progress to the critical phase of the disease.

Up to now, the ELISA technique has been used to quantify various concentrations of antibody or antigen in biological sample. It is commonly used for dengue detection of Non Structural protein 1 (NS1) (Kumarasamy, Chua, et al., 2007; Kumarasamy, Wahab, et al., 2007), Immunoglobulin M (IgM) (Guzman et al., 2010; Nunes et al., 2011; Shu et al., 2003), and Immunoglobulin G (IgG) (Wang & Sekaran, 2010).

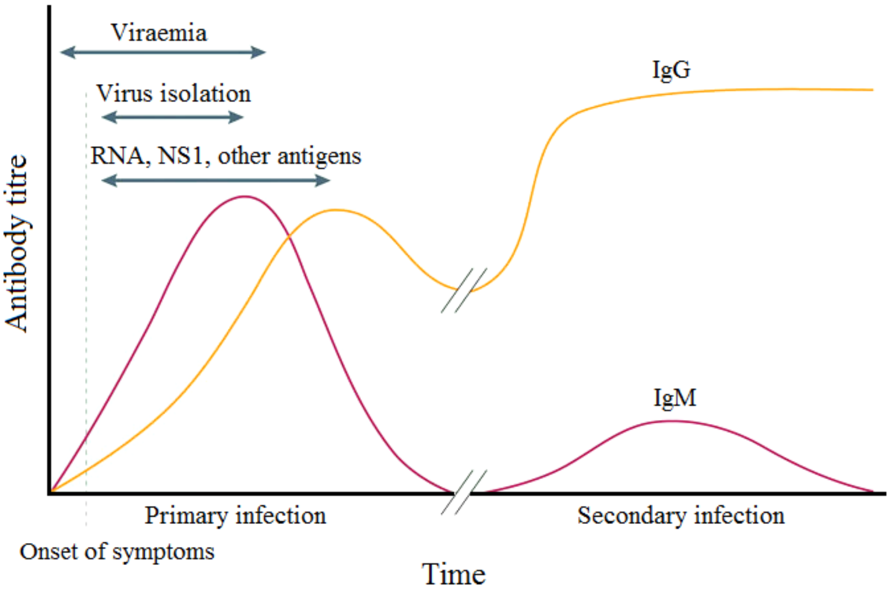

Figure 1.5 Major diagnostic markers for dengue infection (Peeling et al., 2010)

In serological approach, creation of immunoglobulins (IgM, IgG, and IgA) is the reaction of the immune system to infections. These immunoglobulins are particular to virus (E) protein. Depending on the patient's condition, namely, whether or not they have a primary or secondary infection, the sharpness of the response changes (Schilling, Ludolfs, Van An, & Schmitz, 2004). Usually, the IgM response in the primary infection has higher titre in comparison to the secondary one as shown in Figure 1.5 (Guzman et al., 2010; Peeling et al., 2010).

However, common ELISA method is a slow process due to the required incubation times (from a few hours to 2 days), and does not provide enough sensitive method in non-laboratory settings typical of the point of care (POC) (Yager et al., 2008). The automated ELISA system requires high-level expertise, expensive bulky equipment not available at many hospitals and consumes considerable amount of chemicals (Guzman et al., 2010; Hunsperger et al., 2009; Peeling et al., 2010).

Table 1.1 shows several commercial kits for the detection of antibody for identification of dengue virus (Hunsperger et al., 2009). For screening purposes, immunoassay method (ELISA), dipstick and also rapid test using the immune-chromatographic dot blot are the most popular. The sensitivity of ELISA kits is around 96-98% with almost 100% specificity. For rapid diagnostic tests (Table 1.2), sensitivities were obtained in range of 65-84% (C T Sang, Hoon, Cuzzubbo, & Devine, 1998).

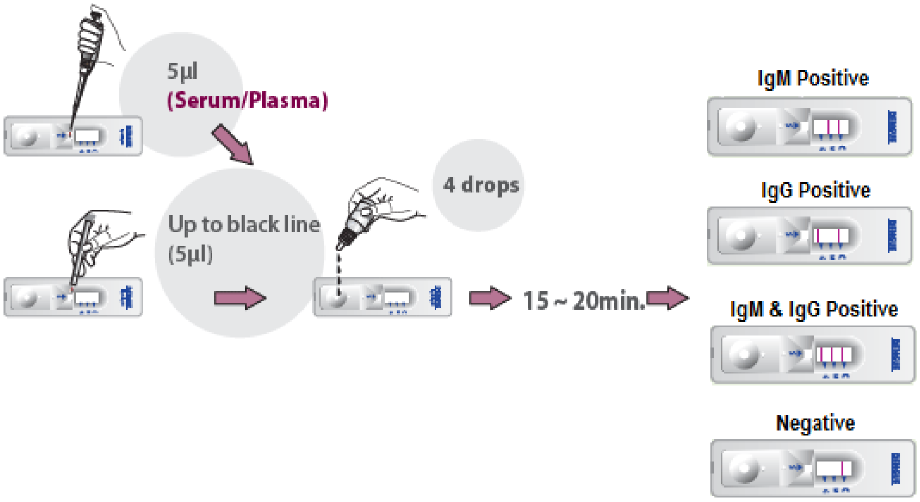

Figure 1.6 Test procedure of the rapid dengue fever diagnosis, adapted from Standard Diagnostics (SD) Inc. database

Table 1.1 Laboratory Methods (ELISAs)

Company, location	Panbio Diagnostics, Windsor, Queensland, Australia	Bio-rad, HERCULES, CA, USA	Omega Diagnostics, Alva, UK	Focus Diagnostics, Cypress, CA, USA	Standard Diagnostics, Kyonggi-do, South Korea[i]
Existing Tests	IgM and IgG	NS1, IgM and IgG	IgM and IgG	IgM and IgG	NS1, IgM and IgG
Technique	Biochemical	Biochemical	Biochemical	Biochemical	Biochemical
Format	12 strips of 8 wells	12 strips of 8 wells	12 strips of 8 wells	12 strips of 8 wells	12 strips of 8 wells
No. tests/package	96	96	96	96	96
Antigen	Recombinant DENV 1–4	Purified DENV 2	DENV 1–4	DENV 1–4	DENV 1–4
Sample volume, µL	10	10	20	10	10
Total incubation time	130 min at 37°C	120 min at 37°C	110 min at 37°C	240 min at room temperature	130 min at 37°C
Storage conditions, °C	2–30	2–8	2–8	2–8	2–8
Specimen type	Only Serum	Only Serum	Only Serum	Only Serum	Only Serum
Sensitivity (%)	99.0	70-84	62.3	98.6	98.2 for NS1 96.4 for IgM 98.1 for IgG
Specificity (%)	79.9-86.6	94-100	97.8	79.9-86.6	100 for NS1 96.7 for IgM 98.9 for IgG

Rapid immune chromatography method also known as rapid diagnostic test (RDT) is another option for detection of dengue infection (Initiative & others, 2005; Chew Theng Sang, Hoon, Cuzzubbo, & Devine, 1998; Vaughn et al., 1998). The method is characterized by its ease of use and rapid detection rate, requiring only a drop of serum/plasma for diagnosis as shown in Figure 1.6.

---

[i] SD kits currently used in UM Medical Centre.

Table 1.2 Commercial rapid diagnostic tests for detection of dengue virus

Company, location	Panbio Diagnostics, Australia	Bio-rad, HERCULES, CA, USA	Pentax, Tokyo, Japan	Zephyr Biomedicals, Panaji, India	Standard Diagnostics, South Korea
Existing Tests	IgM and IgG	NS1, IgM and IgG	IgM and IgG	IgM and IgG	NS1, NS1/IgM and NS1/IgM/IgG
Assay principle	Particle flow	Particle flow	Lateral flow	Lateral flow	Lateral flow
Format	Cassette	Cassette	12 strips of 8 wells	Cassette	Cassette
No. tests/package	25	25	96	25	25
Antigen	Recombinant DENV 1–4	Recombinant DENV 1–4	DENV 1–4	Recombinant DENV (serotype not specified)	Recombinant DENV 1–4 envelope protein
Specimen type	Serum, plasma, or whole blood	Serum or plasma	Serum or plasma	Serum, plasma, or whole blood	Serum or plasma
Sample volume, µL	10	10	1	5	5
Duration of test	15 min	15 min	90 min	15 min	15–20 min
Storage conditions, °C	2–30	2–30	2–8	4-30	1-30
Additional equipment required	No	No	Yes (e.g., micropipette)	No	No
Sensitivity (%)	77.8	54-71	97.7	< 90	65 for NS1 78 for NS1/IgM 84 for NS1/IgM/IgG
Specificity (%)	90.6	94-100	76.6	< 90	94-100 for NS1 94-100 for NS1/IgM 89-100 for NS1/IgM/IgG

There are several commercial antibody detection kits for identification of dengue virus (Table 1.2). The most popular methods for screening purposes are immunoassay method (ELISA), dipstick and also rapid testing using the immune-chromatographic dot blot. The ELISA kits sensitivity range is 96-98% while their specification is close to 100%. For the rapid tests, sensitivity is in the range of 65-84% which can make it relatively unreliable (Hunsperger et al., 2009).

In the last few decades, researchers (Boltovets et al., 2004; Kumbhat, Sharma, Gehlot, Solanki, & Joshi, 2010; Piliarik et al., 2012; Wijaya et al., 2011) have studied on nondestructive techniques in order to detect intact viruses, without manipulating in their structures. These techniques are often based on the interaction between intact virus and intact cell. There are a number of optical techniques, which can detect intact viral particles (DaCosta, Wilson, & Marcon, 2005; Lazcka, Campo, & Munoz, 2007; Seydack, 2005; Zhou et al., 2004). Among these techniques, the surface plasmon resonance (SPR) is one of the most significant techniques that are used extensively for studying diagnosis of the intact viruses.

According to the stated points, we would like to propose a strategy to detect the anti-dengue virus in human serum sample for all four serotypes of dengue virus simultaneously. The optical method that is used in this research introduces an effective and rapid POC diagnostic test to solve the problems of indirect viral particles diagnosis.

1.3 Statement of problem

In conventional method, apart from having a well-trained staff, the test is many hours of labor, and very time consuming. Having a lot of sequent steps for diagnosing diseases and taking approximately half a day to complete one experiment are another issue in conventional methods. This is because each subsequent assay step needs specific time for separating, bonding, or mixing between antigens, antibodies, and solutions. Therefore, special care should be taken at the specific time and it is a complicated method that needs the use a special microtiter plate, lot of reagents, waiting for a sample-reagents reaction and incubation time obtain results. Accuracy is another factor of major importance in the modality of these assays. In addition, the conventional experiments are accomplished by manual intervention, and expensive interconnection techniques can take a long time and high cost (Crowther, 2000).

Rapid immune chromatography method, as previously introduced as RDT, only takes a few minutes (~15-20 minutes) and is easy to use. In the proposed method, one drop of blood sample is collected and applied into the device. Therefore, rapid immunochromatography method is only suitable for screening. This method is also not able to deliver high sensitivity and specificity results (Sang, L. S. Hoon, Cuzzubbo, et al., 1998; Tricou et al., 2010).

Sunita Kumbhat et al., 2010, have reported that the optical technique can detect the dengue virus; however, they have failed in categorizing all four serotypes of this virus. Moreover, their proposed method does not meet the point-of-care.

1.4 Objectives

The main aim of this study is to establish an assay for the diagnosis of dengue infection virus that can be carried out on a single device with a single sample and also with short turn-around time. The main objectives of this work are to simulate, implement, and optimize a rapid diagnostic test based on surface plasmon resonance (SPR) technique for detection of anti-dengue virus in human serum samples. The main objectives of this research work is stated as follows:

- ✓ COMSOL along with MATLAB will be used to simulate the intended SPR structures analytically and numerically
- ✓ Rapid detection of dengue virus experimentally through SPR technique
- ✓ Determination of sensitivity and specificity of the proposed virus detection method
- ✓ Optimization of sample volume is done through study on different concentrations
- ✓ At the end, the validity of simulation results is examined by comparison with experimental results

1.5 Overview of the study

This study consists of the five chapters. Chapter 1 presents the introduction, research background, statement of problem, objectives, and summary of this study. Chapter 2 introduces photonics and plasmonics, including excitation of surface plasmon, surface plasmon polaritons, surface plasmon resonance and theoretical background (wave equations) which have been used in the study. Chapter 3 discusses the design of SPR structure via numerical method. In order to develop the analytical model for our proposed SPR configuration, almost all dielectric function models are studied and employed in our model. Also the methods and setup of our experiments are described in chapter 3. In Chapter 4, the discussion will be on the experimental assays. It shows the immobilization of antigen is done on the sensor surface, and examines all samples in four serotypes of dengue virus successfully. Scanning electron microscopy (SEM) and atomic force microscopy (AFM) images show that virus immobilization has been done properly. Optimization using sensors and well-regeneration of the chip surface are two significant issues of the quality and accuracy of microbiological laboratory results that is further discussed in this chapter. This chapter also compares and interprets the obtained results from mathematical analysis with experimental ones. This comparison provides a validity of experimental results based on the database provided by University of Malaya Medical Centre (UMMC), which has been examined with conventional laboratorial diagnosis. At the end, it calculates the sensitivity and specificity of the biosensor. The conclusion and future works are stated in Chapter 5.

2 CHAPTER II: THEORY AND BACKGROUND OF SURFACE PLASMONS

2.1 Introduction

Robert W. Wood (1868-1955) was the first scientist who accurately described the effects of surface plasmons (SPs) by examining the spectra of an incandescent lamp with a new metallic grating in 1902 (Wood, 1902). Wood expected a smooth and slow change in the intensity distribution but instead observed sharp and narrow, bright and dark bands. He also noticed that this unexpected behavior occurs only when the incident wave is s-polarized, that is, when the only magnetic field component of the incident wave is parallel to the grating. Wood could not explain the results he obtained in the framework of the existing theory and described them as anomalies. Ever since, this phenomena is referred to as Wood’s anomalies (Fano, 1941; Hessel & Oliner, 1965; Raether, 1988a). Fano (Fano, 1941) and later Hessel and Oliner (Hessel & Oliner, 1965) were among the first to develop a theory that explained Wood’s anomalies by coupling light into EM surface waves, mediated by the metallic grating structure.

According to the free electron model, metal consists of a lattice formed by positive ions and electrons from the valence band, which move through the body and are only weakly bound to the ion cores, similar to gas (Fox, 2001; Mizutani, 2001; Sólyom, 2010). The coherent oscillations of the valence (or conducting) electrons are called bulk (volume) plasmons or SPs, depending on whether the plasmon oscillation takes place inside or at the surface of the metal. Bulk plasmons were first scrutinized in detail in the early 1950s by Pines and Bohm, who studied the effect of electrons passing through metal (Bohm & Pines, 1951, 1953; Pines & Bohm, 1952; Pines, 1953). In 1957, SPs were first predicted by Ritchie (Ritchie, 1957) who explained unexpected low frequency losses (below the bulk plasmon frequency ω, see section 2.4) during a study of the angle-energy distribution of electrons passing through thin metal films. Two years later, SPs were verified experimentally by Powell and Swan (Powell & Swan, 1959) by measuring the energy distribution of electrons passing through an aluminum film.

In this thesis, Maxwell’s equations are introduced in section 2.2, followed by a brief discussion on the constitutive relations in the subsections, in the context of energy conservation, pointing vector, and wave equations. In section 2.3 the surface plasmon resonance phenomenon is introduced followed by a concise discussion on the SPR concept, excitation, configuration, and so on.

In section 2.4, mathematical equations of SP propagation on a flat metal surface are presented analytically and numerically. Starting from Helmholtz’s equation and applying appropriate boundary conditions, the dispersion relation for the plasmon wave number $q(\omega)$, where ω is the angular frequency, is derived and the solutions’ main characteristics are discussed. SP propagation on a metal film bound by a dielectric on each side, also called DMD (dielectric-metal-dielectric), is studied in this section. In this configuration, coupling of SPs for sufficiently thin metal film produces additional plasmon modes known as film plasmons. It will be shown that film plasmons have either a symmetric or anti-symmetric EM field distribution across the film with respect to the middle plane. The dispersion relations of all possible modes are analyzed and the results in relation to nanofocusing are discussed.

In section 2.5 an overview of the different analysis methods applied within this thesis is presented, and to conclude the literature review, surface plasmon application in sensing is presented in section 2.6.

2.2 Theoretical background of electromagnetic

Light can be viewed from two aspects: it is an electromagnetic wave and it has particle-like properties. Electromagnetic wave expressions can be conveyed as a solution to a set of equations called Maxwell's equations, energy conservation, Poynting vector, and wave equations, which are introduced next (Yamamoto, 2008).

2.2.1 Maxwell's equations in differential form

Maxwell's equations are generally described as follows (Yamamoto, 2008):

$$\nabla . D = \rho, \tag{2.1}$$

$$\nabla . B = 0 \, , \tag{2.2}$$

$$\nabla \times \mathrm{E} = -\frac{\partial \mathrm{B}}{\partial \mathrm{t}} \, , \tag{2.3}$$

$$\nabla \times H = J + \frac{\partial D}{\partial t} \, , \tag{2.4}$$

where the electric field *E*(V/m) and magnetic field *H*(A/m) are related to the electric displacement (or dielectric flux density or electric flux density) *D*(C/m^2) and magnetic-flux density (or magnetic induction) *B*(*T*[i])

$$D = \varepsilon \, \varepsilon_0 E \, , \tag{2.5}$$

$$B = \mu \mu_0 H, \tag{2.6}$$

Here, ε and ε_0[ii] are the dielectric constant (with dimensionless) and electric permittivity of free space, respectively; μ and μ_0[iii] are magnetic permeability (with dimensionless) and magnetic permeability of free space, respectively. It will be assumed that Ohm's law for the relation between the current *J* and electric field *E* is:

$$J = \sigma \, E \, , \tag{2.7}$$

2.2.2 Energy Conservation and the Poynting vector

The equation for motion of point charges is (Yamamoto, 2008):

---

[i] Tesla : N/(A·m)

[ii] $\varepsilon_0 \approx 8.854 \times 10^{-12} F/m$

[iii] $\mu_0 \approx 4\pi \times 10^{-7} H/m$

$$m_i\ddot{r}_i = \int dr\,\{e_i\delta\big(r - r_i(t)\big)E + e_i\delta\big(r - r_i(t)\big)\dot{r}_i \times B\}, \qquad 2.8$$

where trajectory is given by $r_i(t)$. If we apply $(\sum_i v_i)$ from the left, and the velocity is defined as $v_i = \dot{r}_i$ then,

$$\sum_i m_i\, v_i \cdot \dot{v}_i = \sum_i \int dr\,\{e_i\delta\big(r - r_i(t)\big)v_i \cdot E + e_i\delta\big(r - r_i(t)\big)v_i \cdot [v_i \times B]\}$$

$$= \textstyle\sum_i \int dr\;\, e_i\delta\big(r - r_i(t)\big)v_i \cdot E\ , \qquad 2.9$$

From the definition of current and 2.4 we have:

$$J = \textstyle\sum_i e_i\dot{r}_i\,(t)\delta\big(r - r_i(t)\big) = \nabla \times H - \frac{\partial D}{\partial t}\,, \qquad 2.10$$

Then,

$$\sum_i \frac{d}{dt}\left(\frac{1}{2}m_i v_i^2\right) = \int dr\left(\nabla \times H - \frac{\partial D}{\partial t}\right).E$$

$$\frac{1}{2}\frac{\partial}{\partial t}(E.D + B.H) = E.\frac{\partial D}{\partial t} + H.\frac{\partial B}{\partial t}$$

$$= E.\frac{\partial D}{\partial t} - H.(\nabla \times E)\,, \qquad 2.11$$

$$\frac{d}{dt}\left(\sum_i \frac{1}{2}m_i v_i^2\right) = \int dr\left[-\frac{1}{2}\frac{\partial}{\partial t}(E.D + B.H)\right.$$

$$\left.\underbrace{-H.(\nabla \times E) + E.(\nabla \times H)}_{=-\nabla\cdot(E\times H)}\right]$$

$$\frac{d}{dt}\left[\underbrace{\sum_i \frac{1}{2}m_i v_i^2}_{kinetic\ energy} + \underbrace{\frac{1}{2}\int dr(E.D + B.H)}_{total\ energy\ of\ electromagnetic\ feld}\right] =$$

$$-\int dS \underbrace{[E \times H]}_{Poynting\ vector}\ .n\,, \qquad 2.12$$

From above equations the Poynting vector $S = [E\times H]$ means the energy flux is leaving the system.

2.2.3 Wave equations

From 2.3 and 2.6,

$$\nabla \times E = -\mu\mu_0 \frac{\partial H}{\partial t} , \tag{2.13}$$

From 2.4, 2.5, and 2.7,

$$\nabla \times H = \sigma E + \varepsilon\, \varepsilon_0 \frac{\partial E}{\partial t} , \tag{2.14}$$

If we apply $\nabla \times$ to 2.13 and $\partial/\partial t$ to 2.14 and use the relation

$$\nabla \times \nabla \times E = \nabla \times \begin{vmatrix} i & j & k \\ \dfrac{\partial}{\partial x} & \dfrac{\partial}{\partial y} & \dfrac{\partial}{\partial z} \\ E_x & E_y & E_z \end{vmatrix} = \begin{vmatrix} i & j & k \\ \dfrac{\partial}{\partial x} & \dfrac{\partial}{\partial y} & \dfrac{\partial}{\partial z} \\ \dfrac{\partial E_z}{\partial y} - \dfrac{\partial E_y}{\partial z} & \dfrac{\partial E_x}{\partial z} - \dfrac{\partial E_z}{\partial x} & \dfrac{\partial E_y}{\partial x} - \dfrac{\partial E_x}{\partial y} \end{vmatrix}$$

$$= i\left[\frac{\partial^2 E_y}{\partial_x \partial_y} - \frac{\partial^2 E_x}{\partial y^2} - \frac{\partial^2 E_z}{\partial z^2} + \frac{\partial^2 E_z}{\partial_x \partial_z}\right] + j[\dots] + k[\dots]$$

$$= i\frac{\partial}{\partial x}\left(\frac{\partial E_x}{\partial x} + \frac{\partial E_y}{\partial y} + \frac{\partial E_z}{\partial z}\right) + j\frac{\partial}{\partial y}\nabla \cdot E + K\frac{\partial}{\partial z}\nabla \cdot E$$

$$-i\nabla^2 E_x - j\nabla^2 E_y - \mathrm{k}\nabla^2 E_z$$

$$= \nabla(\nabla \cdot E) - \nabla^2 E , \tag{2.15}$$

If we assume ρ = 0, $\nabla \cdot E = 0$, then

$$\nabla^2 E = \sigma\mu\mu_0 \frac{\partial E}{\partial t} + \mu\mu_0\varepsilon\varepsilon_0 \frac{\partial^2 E}{\partial t^2} , \tag{2.16}$$

In the same way we can get

$$\nabla^2 H = \sigma\mu\mu_0 \frac{\partial H}{\partial t} + \mu\mu_0\varepsilon\varepsilon_0 \frac{\partial^2 H}{\partial t^2} , \tag{2.17}$$

In case the electric field has a plane wave form:

$$E = E_0 e^{i(k.r-\omega t)}, \qquad 2.18$$

where E_0 is the polarization vector, wave vector k is in the direction of the wave propagation and the magnitude is given in 2.16.

$$k^2 = i\sigma\mu\mu_0\omega + \mu\mu_0\varepsilon\,\varepsilon_0\omega^2, \qquad 2.19$$

In vacuum, $\varepsilon = 1, \mu = 1, \sigma = 0$ and $c/v = \lambda, c/\omega = \lambda/(2\pi), k = 2\pi/\lambda = \omega/c$ then

$$c = 1/\sqrt{\mu_0\varepsilon_0}\,, \qquad 2.20$$

The complex optical index $\tilde{n}$ may be given by

$$k = \frac{2\pi}{\lambda} = \frac{\omega}{v} = \frac{\tilde{n}\omega}{c}\,, \qquad 2.21$$

$$\tilde{n}^2 = k^2c^2\big/\omega^2 = \mu\varepsilon + i\frac{\sigma\mu}{\varepsilon_0\omega}\,, \qquad 2.22$$

$$\tilde{n} = \mathrm{n} + ik\,,\; k = {}^{\tilde{n}\omega}\!/_{c} = (n + ik)\,\omega/c\,, \qquad 2.23$$

where *n* and *k* are the real and imaginary parts of the complex optical index, respectively.

$$E(z,t) = E_0 e^{-k\omega z/c} e^{i(n\omega z/c-\omega t)}, \qquad 2.24$$

$$I(z) \propto E^*E = |E_0|^2 e^{-2k\omega z/c} = I_0 e^{-\alpha z} \qquad \text{(Lambert's law) } 2.25$$

$$\alpha = 2k\omega/c\,, \qquad 2.26$$

$$\tilde{n}^2 = \tilde{\varepsilon} = \varepsilon_1 + i\varepsilon_2 \quad [\mu = 1, \sigma = 0 \text{ in } 2.22], \qquad 2.27$$

$$\varepsilon_1 = n^2 - k^2,\; \varepsilon_2 = 2nk\,, \qquad 2.28$$

Here, α is the absorption coefficient, $\tilde{\varepsilon}$ is the complex dielectric constant, and ε_1 and ε_2 are the real and imaginary parts of the complex dielectric constant, respectively.

If we take the divergence of the plane-wave electric field,

$$divE = \left(i\frac{\partial}{\partial x} + i\frac{\partial}{\partial y} + i\frac{\partial}{\partial z}\right).\left(E_{0x}i + E_{0y}j + E_{0z}k\right)e^{i\left(k_x x + k_y y + k_z z - \omega t\right)}$$

$$= i\left(k_x E_{0x} + k_y E_{0y} + k_z E_{0z}\right) = iK.E_0$$

$$= \frac{\rho}{\varepsilon\,\varepsilon_0} = 0\,, \qquad 2.29$$

It is possible to find that the electric field is a transverse wave, i.e. $k \perp E_0$.

If the magnetic-flux density B is written as

$$B = \frac{K \times E_0}{\omega} e^{i(k.r - \omega t)}, \tag{2.30}$$

then the magnetic-flux density satisfies 2.3 because

$$\begin{aligned} \nabla \times E &= i\left(\frac{\partial E_z}{\partial y} - \frac{\partial E_y}{\partial z}\right) + \cdots \\ &= i\left(ik_y E_z - ik_z E_y\right) + \cdots \\ &= iK \times E \ , \end{aligned} \tag{2.31}$$

$$\begin{aligned} -\frac{\partial B}{\partial t} &= -\frac{K \times E_0}{\omega}(-i\omega) e^{i(K.r - \omega t)} \\ &= iK \times E \ , \end{aligned} \tag{2.32}$$

2.3 Introduction to optics and surface plasmons

Optics is a branch of science that was developed before the knowledge of light could be quantized into photons. Therefore, it deals with light and its manipulation at a very broad range of wavelengths. The classical optics theory does not necessarily depend on the fact that light is quantized into photons. Photonics, as the name suggests, also relates to photons. It deals with aspects of light such as the generation, manipulation, and detection of light for different purposes. It involves the wave and particle nature of light, and is usually referred to as the technical, application-based aspect of light in areas such as telecommunications, spectroscopy and nanocircuits (Ahmet Arca, 2010).

2.3.1 History of Surface Plasmon Resonance

Sharma *et al.* and Homola *et al.* provided a detailed history of surface plasmon resonance (Jiří Homola, Yee, & Gauglitz, 1999; Sharma, Jha, & Gupta, 2007), which is summarized in this section with reference to the original papers. As early as 1907, Zenneck (Zenneck, 1907) and Sommerfeld in (Sommerfeld, 1909) demonstrated and formulated the existence and properties of radio frequency surface Electromagnetic (EM) waves at the interface of a loss-free medium and a lossy dielectric, or a metal. The main stride towards the existence of surface plasmon (SP) waves was made in 1957, when Ritchie derived the energy distribution of a fast electron losing energy to the conduction electrons in a metallic foil and proposed that the energy loss is due to surface plasmon excitation (Ritchie, 1957). Ritchie's theory was further supported by Powell and Swan (1960) who detected the excitation of surface plasmons in aluminum and magnesium via electrons (Powell & Swan, 1960). Their work was followed by Stern and Ferrell, who in the same year derived the condition of resonance for surface plasmon modes and showed that the surface waves involved electromagnetic radiation coupled to surface plasmons (Stern & Ferrell, 1960). In 1968, Otto introduced the method of attenuated total reflection (ATR) for resonant excitation of surface plasmon waves by light (Otto, 1968). His idea involved using a prism near the metal vacuum interface, so that the surface plasmon waves would be excited optically by the evanescent waves present in total reflection. However, the most popular and widely used method to date is the Kretschmann configuration proposed in 1968 (Kretschmann & Raether, 1968), which made the practical and commercial use of surface plasmon resonance (SPR) possible. Instead of a finite air gap between the prism base and metal substrate like in the Otto configuration, a thin metal layer (10nm-100nm) remains in contact with the prism base.

The prospects of surface plasmon resonance (SPR) sensing in the field of thin film characterization and monitoring electrochemical interfaces were further realized in work by Pockrand *et al.* and Gordon *et al.* (Gordon Ii & Ernst, 1980; Pockrand, Swalen, Gordon II, & Philpott, 1978). During the early 1980s, Nylander *et al.* and Liedberg *et al.* demonstrated the use of SPR for gas detection and bio-sensing (Liedberg, Nylander, & Lundström, 1995; Liedberg, Nylander, & Lunström, 1983; Nylander, Liedberg, & Lind, 1983). From that time onwards, the surface plasmon resonance technique has been extensively utilized for the characterization and quantization of physical, chemical and biological interactions. Since 1990, several companies have commercially launched surface plasmon resonance biosensors (Jiří Homola et al., 1999) as the Biacore instrument (Jönsson et al., 1991). This instrument is the most accurate, sensitive, reproducible, reliable direct SPR biosensor technique for measuring real-time biomolecular interactions.

2.3.2 Surface plasmon concept

The surface plasmon is a traveling wave oscillation of electrons that can be excited in the surface of certain metals with the right material properties. Because a plasmon consists of oscillating electric charges, they also have an electromagnetic field associated with them which also carries energy (Skullsinthestars, 2010).

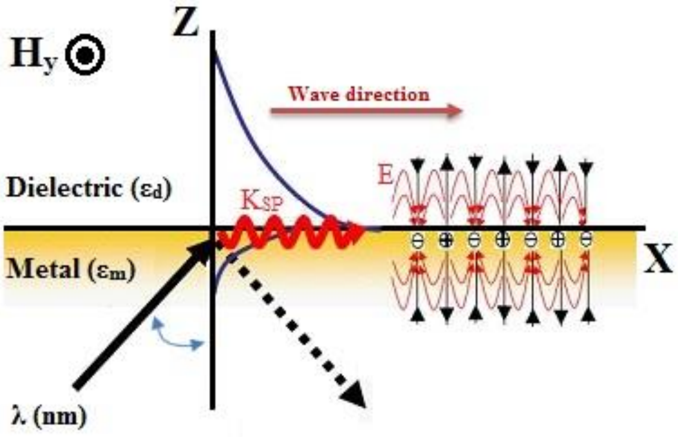

Figure 2.1 A simple schematic of a surface plasmon

To explain Figure 2.1, it first may help to mention the electrical properties of electrical conductors like metals. Electrically conductive materials have a large "pool" of electrons within their last orbit in the atom that are essentially free to move about the material. When an electric field is applied to the conductor, the electrons are forced into new positions, leaving positive ions behind. The electrons tend to flow along the metal’s surface, and the net positive charge left behind is also on the surface.

SPR is effectively a resonant transfer of energy from the optical excitation to the SP wave. The fields associated with SPs decay exponentially away from the metal surface into the dielectric, thus confining the energy onto the proximity of the metal surface. Therefore the optical changes right next to the metal surface in the dielectric medium, or transduction medium, modify the propagation constant of the surface plasmon and change the SPR condition. The change in SPR condition results in changed optimum incidence angle or wavelength for the SPR excitation. Consequently, variations in optical properties of the dielectric medium are observed by examining the plasmon properties. SPR sensor development dates back to the late 1970s (Jiří Homola et al., 1999).

2.3.3 Surface plasmon excitation

There are two principal means of exciting SPs, namely electron bombardment or using photons. Within the application of light two different techniques have been developed, frustrated total internal reflection (FTIR) or attenuated total internal reflection (ATR), and scattering by nano-sized metallic structures. Since SPs cannot be excited directly by light waves impinging onto an ideal flat surface due to the mismatch of wave numbers, some additional momentum must be provided to the light wave.

2.3.3.1 Excitation by Electrons

In transmission electron microscopy (TEM) or electron energy loss spectroscopy (EELS), a beam of electrons with a well-defined and narrow range of kinetic energies penetrates thin materials, such as metal films or specimens like living cells (Raether, 1988b). Some of the electrons are deflected due to inelastic scattering. As a result, their paths change and kinetic energy is transferred to the sample (inter and intra band transition or phonon and plasmon excitation). The amount of energy loss and scattering angle can be measured in order to obtain chemical and physical data. TEM can also be employed in such a way that the kinetic energy of the electron beam matches so that the

SP can be excited (Raether, 1988b). Though the newest generation of transmission electron spectroscopy can achieve resolution of less than 1nm (Rosenauer, 2003), the TEMs are large and very expensive to operate and probes are quite difficult to prepare. That is primarily the reason why TEMs are not used for SP excitation.

Pfeiffer *at el.* (Pfeiffer, Economou, & Ngai, 1974), Martinos and Economou (Martinos & Economou, 1981, 1983) and Ashley and Emerson (Ashley & Emerson, 1974) demonstrated theoretically that SPs can be excited on a metal cylinder by orbiting electrons. In their models, a magnetic field oriented along the cylinder axis was applied in order to keep the electrons around the cylinder. However, the electrons have to encircle the cylinder on a very low orbit to excite the SPs. Another drawback is that the metal cylinder must be very accurately shaped (Martinos & Economou, 1981). For more details see section 2.7.1.

2.3.3.2 Excitation by Photons

In 1968, A. Otto (Otto, 1968) proposed a new technique based on frustrated total internal reflection (FTIR) or attenuated total internal reflection (ATR) to overcome the difficulties experienced with Electron Energy Loss Spectrometry (EELS). With this novel approach, photons are employed to excite SPs. Ever since several configurations based on ATR have been proposed that ensure the match between the wave numbers of the incident light and SPs, including the Otto-Raether and Kretschmann configurations. Similarly, other photon-based approaches are gratings and surface defects or, more recently, pointed probes of near field microscopes.

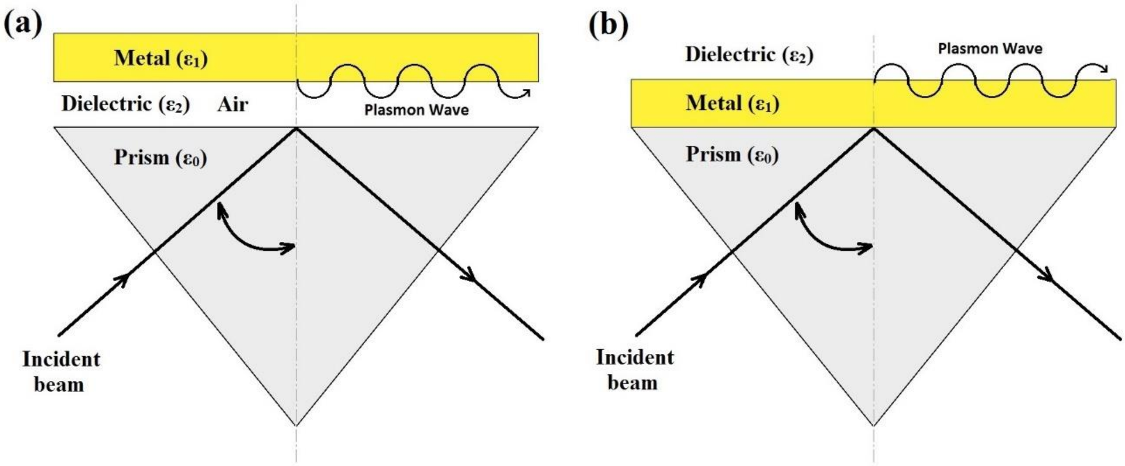

Figure 2.2 (a) Kretschmann; and (b) Otto configuration of an attenuated total reflection setup for coupling surface plasmons. In both cases, the surface plasmon propagates along the metal/dielectric interface

2.3.4 Otto and Kretschmann configurations

The Otto or Otto-Raether configuration, as depicted in Figure 2.2, consists of a prism in close proximity to a metal surface. A laser beam is coupled at the critical angle θ into the prism in such a way that the beam at the base of the prism, which faces the metal surface, becomes totally reflected. Due to total internal reflection, the evanescent field penetrates the metal surface and excites the SPs (Knoll, 1998; Zayats, Smolyaninov, & Maradudin, 2005). If the wave number of the incident wave parallel to the interface prism-metal matches the wave number of the SPs, a dip in reflected wave intensity can be observed. In that event, part of the evanescent field's energy has been transferred into the SP; hence the name attenuated total reflection. In order to obtain good coupling efficiency the prism must be placed very close, usually a few tens of nanometers, and aligned parallel to the metal. However, this demands very clean and planar surfaces of both prism and metal; consequently this configuration is not applicable for curved surfaces such as a metal cylinder or metal sphere. This is one of the reasons why this configuration has not been widely used (Knoll, 1998).

The Kretschmann configuration (Figure 2.9) is also based on ATR. In the simplest form, it consists of a prism and a very thin metal film deposited on the base of the prism. The evanescent wave, originating again from total reflection at the boundary prism-metal, penetrates through the metal film and triggers surface plasmon propagation at the outer metal interface. In addition, there is a second angle of incidence at which SPs at the interface prism-metal film can be excited (Kretschmann & Raether, 1968).

Numerous variations based on the Kretschmann geometry have found applications in biotechnology (Abdulhalim, Zourob, & Lakhtakia, 2008; Hutter & Fendler, 2004; Vo-Dinh, 2008), surface science and microscopy (Novotny & Hecht, 2012; Prasad, 2004; Raether, 1988b; Zayats et al., 2005) owing to the extraordinary sensitivity of surface plasmon-based sensors. Even the slightest change in the permittivity of the attached film for instance, results in strong reflected angle variation (Prasad, 2004) or a frequency shift that can be detected (Abdulhalim et al., 2008).

However, the Kretschmann geometry can only be applied for the excitation of SPs on planar films that are thinner than the penetration depth of the evanescent wave. Therefore, other means have to be employed to excite SPs on optical thick metal layers or on curved surfaces.

2.3.5 Surface plasmon polaritons

Surface plasmon polaritons (SPPs) are infrared or visible frequency electromagnetic waves trapped at, or guided along metal-dielectric interfaces, which have shorter wavelength than the incident light (photons). Collective charge oscillations at the boundary between an insulating dielectric medium (such as air or glass) and a metal (such as gold, silver or copper) are able to sustain the propagation of infrared or visible frequency electromagnetic waves known as surface plasmon polaritons (SPP).

2.3.6 Surface Plasmon Resonance

Surface plasmon resonance (SPR) is an optical technique with applications in a variety of disciplines, especially in sensing devices. Its popularity can be attributed to the cross-disciplinary philosophy of present-day research (Chhatre, Solasa, Sakle, Thaokar, & Mehra, 2012; Fry et al., 2011; Piliarik et al., 2012; Shalabney & Abdulhalim, 2012; Xu et al., 2012). The SPR can be applied to probe changes in refractive index, which often occurs within an immediate vicinity of the sensor surface. Previously, the SPR was employed to investigate an inherent optical property of the thin metal films. Its usage has subsequently been expanded to a multiplicity of applications including absorbance measurements, bio-kinetics, biosensing techniques, bulk liquid measurements, immune sensing, blood protein detection, gas detection, light modulation, process analytics, spectrometers, microscopy, refractive index measurements, polarization fibers, and thin film characterization (Bhatia & Gupta, 2012; Campbell & Kim, 2007; Liedberg et al., 1983; Giancarlo Margheri et al., 2012; Naimushin et al., 2002; Schmidt, Lee, Yang, & Harrison, 2012; Watanabe, 2011).

However, SPR has not been limited to these fields but has been employed in electrical engineering, chemistry, theoretical physics, and experimental optics as well. The multidisciplinary nature of SPR requires knowledge of optical waveguide, thin-film, and optical detection techniques, besides the application under study. SPR is now widely prevalent due to the cross-disciplinary philosophy of current research (Mcdonnell, 2001).

In sensors, the surface plasmon (SP) mode is stimulated at the interface of a thin metal film and small dielectric layer using a light wave. A refractive index change in dielectric medium results in altered propagation constant of the SP mode waveguide. Therefore, this alters the condition of coupling among the propagated light wave with specific incident angle and the SP wave, which becomes evident as a change in one of the optical wave characteristics interacting with the SP mode. Based on their optical characteristics, these sensors can be categorized into polarization, phase, intensity, wavelength, and angular modulation. In this work, angular modulation was used for detection (Figure 2.4) (J iˇrí Homola, 2006b; Jirí Homola, 2008; Oliveira et al., 2013).

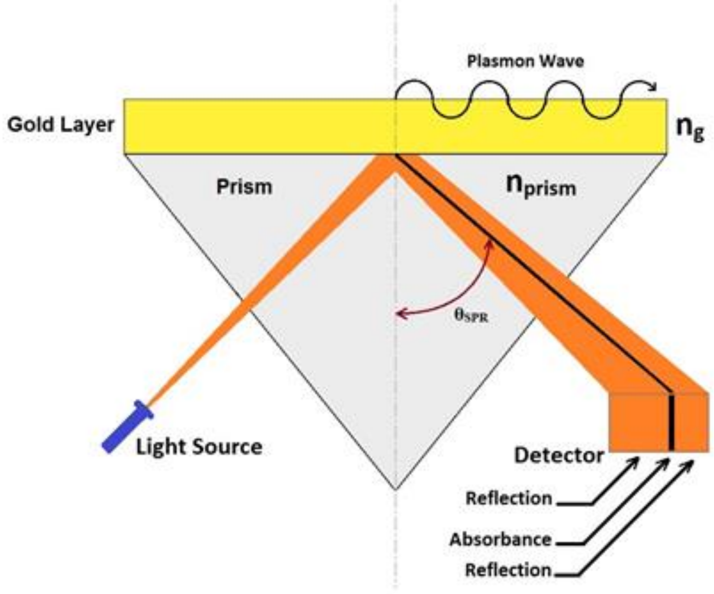

Figure 2.3 The surface plasmon mode (wave) is excited at the interface between a metal film and dielectric medium using a light wave

In SPR sensors with angular modulation, a monochromatic light wave excites a surface plasmon wave. For multiple different angles of incidence of input light the strength of coupling between the incident wave and surface plasmon wave is measured.

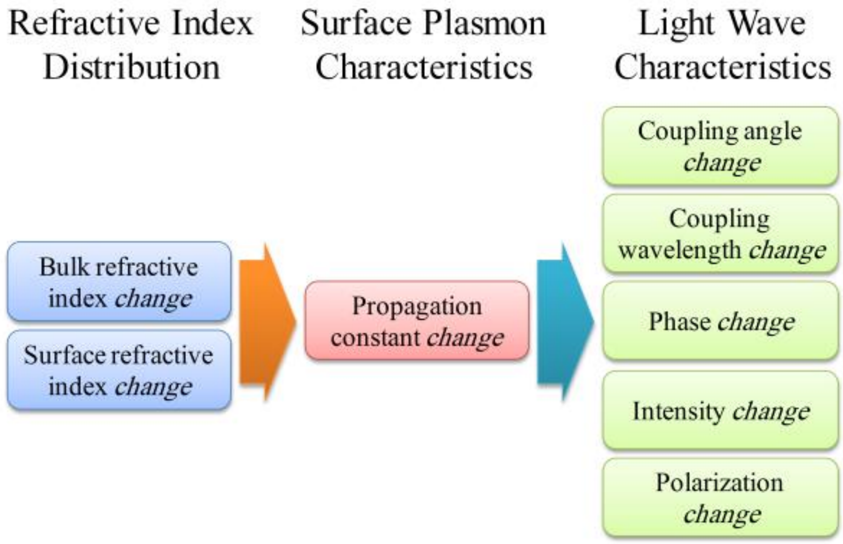

Figure 2.4 Concept of surface plasmon resonance sensors

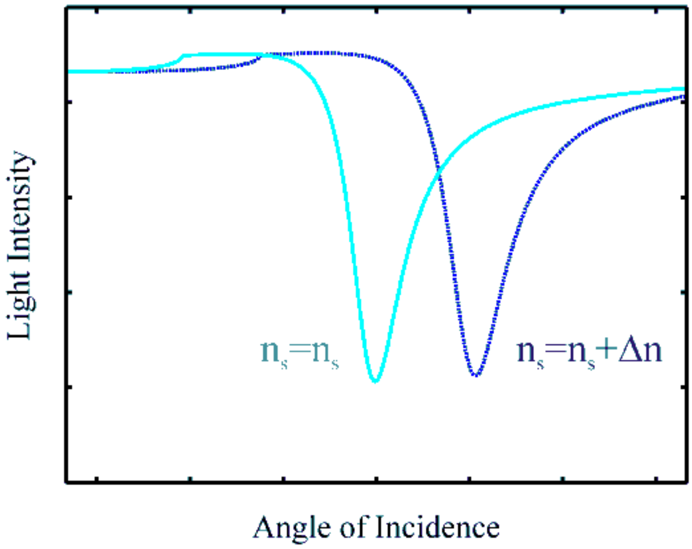

Figure 2.5 Intensity of light wave interacting with a surface plasmon as a function of angle of incidence

In SPR sensors with wavelength modulation, a surface plasmon wave is excited by a collimated, broad-spectrum light wave. Unlike the previous method, the angle at which the light wave is incident onto the metal film is kept constant and the strength of coupling between the incident wave and surface plasmon is measured for the input spectrum. Again, the wavelength that results in the strongest coupling is considered the sensor output (J iˇrí Homola, 2006b).

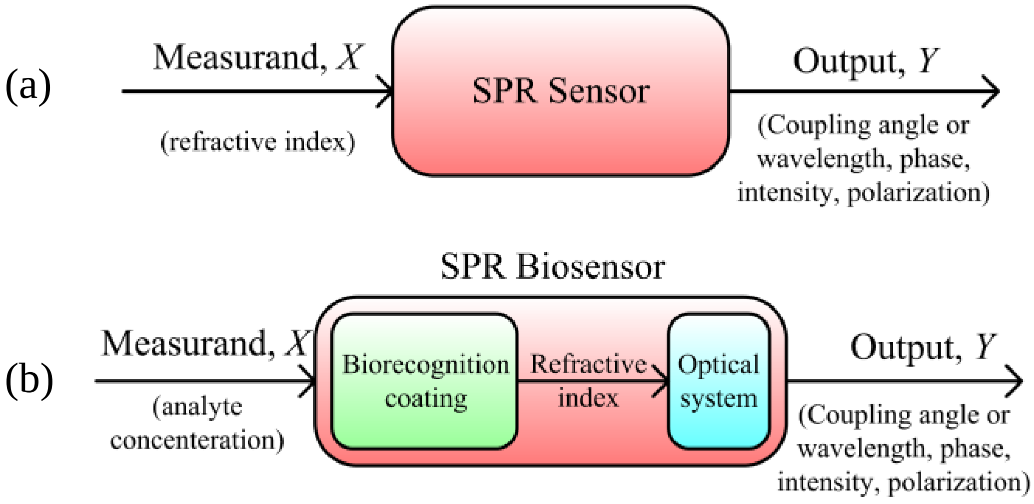

Figure 2.6 (a) Direct and (b) Indirect SPR sensors: measurand and sensor output

For SPR sensors with intensity modulation, the light wave intensity is deemed an indicator of the strength of coupling between the incident light wave and a surface plasmon mode at a single angle of incidence and wavelength (Figure 2.5). The angle of incidence yielding the strongest coupling serves as the sensor output (Figure 2.6) and can help determine the refractive index.

In SPR sensors with phase modulation, the shift in light wave phase interacting with the surface plasmon is measured at a single angle of incidence and wavelength. Phase changes are detected using the interferometry techniques and are used as the sensor output.

In SPR sensors with polarization modulation, changes in the polarization of the light wave interacting with a surface plasmon are measured. The last three techniques are generally used in setups in which the light, for either surface plasmon excitation or measurement, is carried by a waveguide.

In addition to the mentioned categorization, SPR sensors are classified as either direct or indirect. In direct SPR sensors, the measurand (typically refractive index) directly modifies coupling characteristics, while in indirect SPR sensors the measurand modulates an intermediate that alters the coupling characteristics. SPR affinity biosensors are a typical example of indirect SPR sensors (J iˇrí Homola, 2006b).

2.4 Planar Surface Plasmons

A single flat metal surface is probably the most basic metal structure to describe SP propagation. Nevertheless, some important results can be derived with this simple configuration. Within this section, it is assumed that the interface, which separates the metal and dielectric, is placed on the *x*-*z* plane of a Cartesian coordinate system. It is also assumed that the metal occupies the $y < 0$ region and the SPs propagate along the *x*-axis. It can be demonstrated that only TM plasmons can propagate along the surface (Maier, 2007; Raether, 1988b; Zayats et al., 2005) because the relative permeability μ is close to unity for most natural metals at optical frequencies (see Appendix A). There is an alternative explanation derived from the boundary condition

$$(D_d - D_m) \cdot n = \delta \tag{2.33}$$

where D_d and D_m are the dielectric displacement in the dielectric and metal, respectively, and n is the normal vector at the interface. As a consequence of 2.33 only the components of E in the plane of the incident wave can induce longitudinal surface charge density oscillations in the direction of propagation (x-axis) (Knoll, 1998). The only magnetic field component left is H, hence only TM plasmons can propagate along the metal surface. The EM field associated with TM plasmons also decays exponentially away from the interface into both media (Figure 2.7). Therefore, the following solution for H_y can be assumed:

$$H_y = A \cdot e^{j(\omega t - q_X X)} \cdot \exp(\alpha_m y)\; y < 0, \text{metal} \tag{2.34}$$

and

$$H_y = B \cdot e^{j(\omega t - q_X X)} \cdot \exp(-\alpha_d y)\; y > 0, \text{dielectric} \tag{2.35}$$

where A and B are amplitudes to be determined by the boundary conditions; and α_m and α_d are the reciprocal (positive and real) penetration depths into the metal and dielectric, respectively. The TM-plasmon wave number q_x is complex due to the presence of a metal with the permittivity $\varepsilon_m = \varepsilon_m' + i\varepsilon_m''$. Consequently, the amplitude of the SPs decreases with increasing propagation distance, and eventually dissipates. The penetration depth is defined as the distance from the interface metal-dielectric at which the amplitude of H_y is reduced by e^{-1}:

$$\frac{\alpha_d}{m} = \sqrt{{q_x}^2 - {k_0}^2 \frac{\varepsilon_d}{m}} \tag{2.36}$$

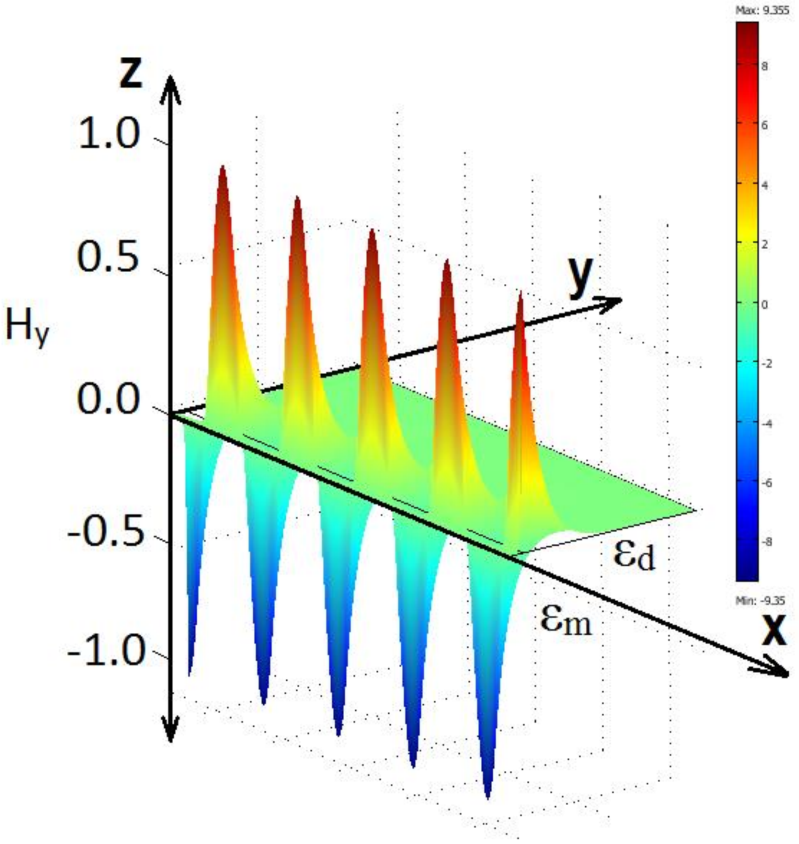

Figure 2.7 3D model of surface plasmon propagating along a flat metal surface in the *x*-direction; A snapshot of the H_y distribution (TM mode) is schematically shown. The relative permittivity ε_d is for the dielectric material and e is for the metal. The evanescent waves in the *y*-direction are indicated by the dash-dotted line.

The penetration depths and permittivities are also related (see Appendix A for derivation) by:

$$-\frac{\alpha_d}{\varepsilon_{m'}} = \frac{\alpha_m}{\varepsilon_d} \tag{2.37}$$

where ε_d and $\varepsilon_m{'}$ are the real permittivities of the dielectric material and metal, respectively. From 2.36 it can also be concluded that the penetration depth of the plasmon into the metal is much smaller than into the dielectric, as indicated in Figure 2.7. The real part of the permittivity of the metal, $\varepsilon_m{'}$, must take on negative values to satisfy 2.37, because the penetration depths are positive real numbers by definition. The real part of the complex wave number can then be written as (Barnes, Dereux, & Ebbesen, 2003; Dragoman & Dragoman, 2008; Knoll, 1998; Maier, 2007; Raether, 1988b):

$$q_x' = k_0\sqrt{\frac{\varepsilon_d \varepsilon_m'}{\varepsilon_d + \varepsilon_m'}} \qquad 2.38$$

In order to obtain a positive wave number, the permittivity condition is $|\varepsilon_m|>\varepsilon_d$. The imaginary part of the plasmon wave number is

$$q_x'' = \frac{k_0}{2}\left(\frac{\varepsilon_d \varepsilon_m'}{\varepsilon_d + \varepsilon_m'}\right)^{3/2} \frac{\varepsilon_m''}{\varepsilon_m'^2} \qquad 2.39$$

The propagation distance of SPs along the surface is limited owing to losses in the metal, and it is represented by the imaginary part of the permittivity ε_m''. The propagation length *L* is defined as (Raether, 1988b; Zayats et al., 2005):

$$L = (2q_x'')^{-1} \qquad 2.40$$

Inserting 2.39 into 2.40 yields:

$$L = \frac{1}{k_0}\left(\frac{\varepsilon_d + \varepsilon_m'}{\varepsilon_d}\right)^{3/2} \frac{(\varepsilon_m')^{1/2}}{\varepsilon_m''} \qquad 2.41$$

The propagation distance *L* on a flat metal surface for gold, silver and aluminum as determined by 2.41 is depicted in Figure 2.8.

Returning to the dispersion relation 2.38, the solutions for the real part of the plasmon wave number q_x of TM plasmons on a silver surface with metal permittivity described by the Drude-Lorentz Model[i] (2.33) surrounded by vacuum is shown in Figure 2.9.

---

[i] $\varepsilon_r(\omega) = 1 - \frac{\omega_p^2}{\omega^2 - i\gamma\omega}$; where ω_p and γ are the bulk plasma frequency and damping frequency respectively.

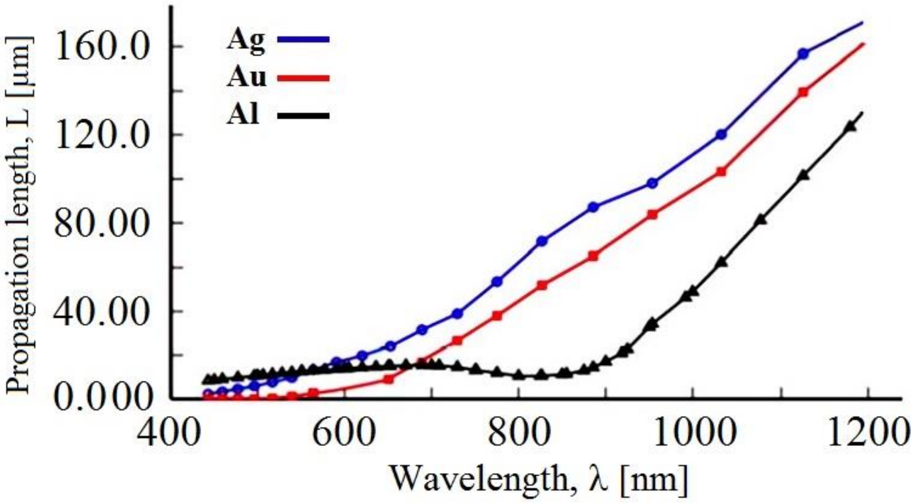

Figure 2.8 Propagation length for SPs on a planar surface for gold, silver and aluminum (Vogel, 2009)

For small wave numbers the dispersion curve of the TM plasmons (Figure 2.9, surface plasmon polaritons) asymptotically approaches the dispersion curve of the bulk wave (light-line) in the adjacent dielectric (Figure 2.9, free space). For large wave numbers it approaches the SP condition $\omega_{sp} = \omega_p/(\varepsilon_d + 1)^{1/2}$, which also corresponds to the condition $\varepsilon_d = -\varepsilon_m(\omega)$. One important result is that the free space curve does not intersect the SPP curve, which represents the dispersion relation of the bulk wave in the adjacent dielectric. Consequently, light waves cannot excite SPs on a flat metal surface or SPs cannot radiate into light waves without appropriate devices, hence the term non-radiative SPs. This is a consequence of Snell's law, which imposes the condition that the component of the wave vector parallel at the interface is continuous. In other words, the wave vector of the surface plasmon and wave vector of the bulk wave do not match at the interface; once the SPs are coupled into a smooth metal surface, they are trapped (Barnes et al., 2003).

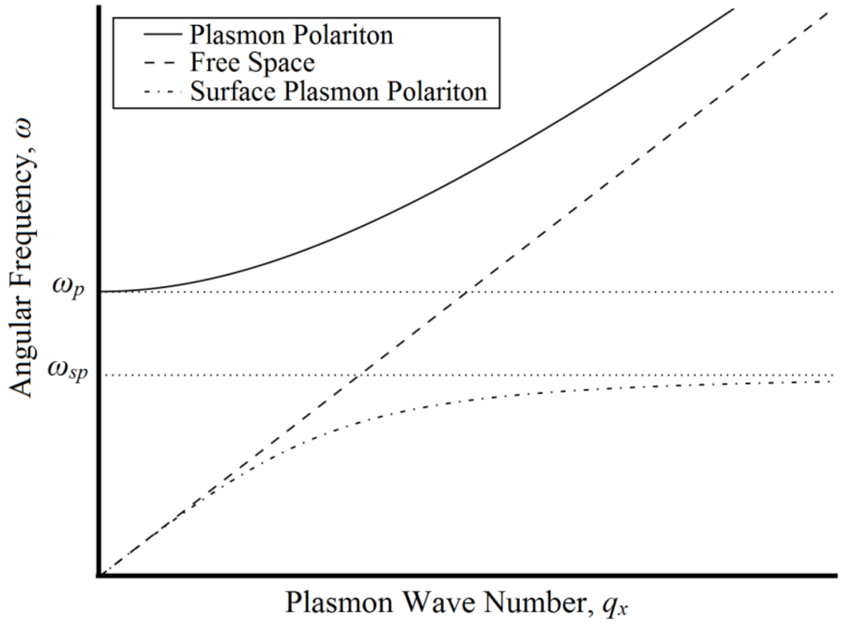

Figure 2.9 Dispersion relation of SPs on a flat Ag surface, with the permittivity of Ag modeled by Drude-Lorentz Model; λ_p is the corresponding plasmon wavelength and ε_d = 1 is the permittivity of the adjacent dielectric material. See text for curve descriptions.

Between the bulk plasma frequency ω_p and surface plasmon frequency ω, no solution corresponding to SPs exists. This can also be shown by substituting Drude-Lorentz Model (DLM) for a weakly damped system ($\varepsilon_r(\omega) = 1 - \frac{{\omega_p}^2}{\omega^2}$; when $\gamma \rightarrow 0$) into 2.38. This frequency gap is also known as the plasmon gap (Maier, 2007). For applied frequencies higher than the bulk frequency ω_{sp} another solution exists, where the plasmon wave radiates in the metal (Figure 2.9, plasmon polariton) (Maier, 2007; Raether, 1988b). However, these modes are not confined to the interface and are of no interest for this project.

2.4.1 Surface plasmons in three-layer configuration

An important extension of a simple metal surface is a three-layer configuration, where each of the layers has an infinite extension in two dimensions. Two basic configurations are well-known: a dielectric gap in a metal, or metal-dielectric-metal (MDM) configuration, and a metal film surrounded by two dielectrics, or dielectric-metal-dielectric (DMD) configuration. However, because of the additional interface, the dispersion relation becomes more complex owing to the fact that the surface plasmons on each interface couple and form new, additional modes when the thickness of the metal film or gap width becomes sufficiently small.

In this section it is assumed that our study adopts the dielectric-metal-dielectric structure that extends infinitely in the x- and y- directions and the plasmon propagation is along the x-axis. In view of the fact that only TM plasmons can propagate, the distinction of different plasmon modes is determined by the distribution of the sole magnetic field component H_y across the metal film (Gramotnev & Vernon, 2007; Gramotnev, 2005).

2.4.2 Theoretical background of SPs in DMD structure

Assume an optical waveguide composed of the three homogeneous layers (Figure 2.10) with a permittivity profile:

$$\begin{aligned} \varepsilon(x) &= \varepsilon_3 \quad x > d, \\ \varepsilon(x) &= \varepsilon_2 \quad -d < x < d\,, \\ \varepsilon(x) &= \varepsilon_1 \quad x < -d, \end{aligned} \tag{2.42}$$

where d is defined the half-thickness of wave guiding layer and ε_i (i = 1, 2, 3) is complex permittivity in general.

With orienting the Cartesian axes as presented in Figure 2.10, the field vectors are only in x and z and the modal fields can be written as:

$$\begin{aligned} E &= \boldsymbol{e}(x) \cdot \exp\big(i(\beta z - \omega t)\big) \\ H &= \boldsymbol{h}(x) \cdot \exp\big(i(\beta z - \omega t)\big) \end{aligned} \tag{2.43}$$

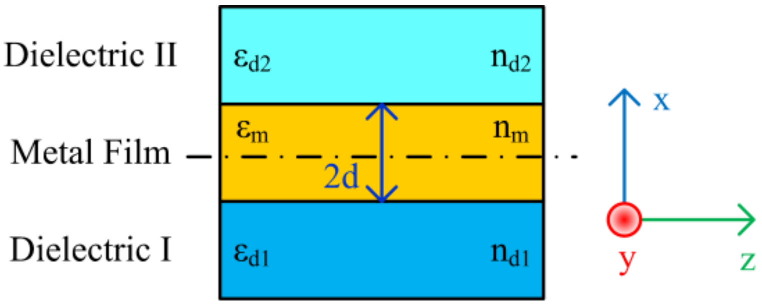

Figure 2.10 Three-layer dielectric-metal-dielectric waveguide structure

Substituting the field profiles into a simplified wave equation yields for the transversal components of the field vectors:

$$\frac{\partial^2 e_y(x)}{\partial x^2} + (\omega^2 \varepsilon \varepsilon_0 \mu_0 - \beta^2) e_y(x) = 0; \text{ TE modes,} \qquad 2.44$$

$$\frac{\partial^2 h_y(x)}{\partial x^2} + (\omega^2 \varepsilon \varepsilon_0 \mu_0 - \beta^2) h_y(x) = 0; \text{ TM modes,} \qquad 2.45$$

In each medium the solution of the above equations can be stated as a linear combination of the functions: $\exp(iK_i x)$ and $\exp(-iK_i x)$, where ${K_i}^2 = \omega^2 \varepsilon_i \varepsilon_0 \mu_0 - \beta^2$(i = 1, 2, 3) (J iˇrí Homola, 2006b).

Outside the wave guiding layer, the fields of modal bound to a waveguide decline exponentially through increasing distance from a waveguide. The boundary conditions of Maxwell’s equations have a requirement that the components of electric and magnetic field intensity vectors parallel to the boundaries of wave guiding layer which are continuous at each boundary ($x = d$ and $x = -d$). The conditions of boundary offer the homogenous series of four linear equations for four unknown amplitudes, which yield a non-zero solution only if the determinant of the matrix of coefficients is equal to zero (J iˇrí Homola, 2006b). This requirement leads to the following eigenvalue equations:

$$\tan(Kd) = \frac{\gamma_1/K + \gamma_3/K}{1 - (\gamma_1/K)(\gamma_3/K)}; \text{ TE modes,} \qquad 2.46$$

$$\tan(Kd) = \frac{{\gamma_1 \varepsilon_2}/{K\varepsilon_1} + {\gamma_3 \varepsilon_2}/{K\varepsilon_3}}{1 - ({\gamma_1 \varepsilon_2}/{K\varepsilon_1})({\gamma_3 \varepsilon_2}/{K\varepsilon_3})};\ \text{TM modes,} \qquad 2.47$$

where $K^2 = \omega^2 \varepsilon \varepsilon_0 \mu_0 - \beta^2$ and $\gamma_{1,3}{}^2 = \beta^2 - \omega^2 \varepsilon_{1,3} \varepsilon_0 \mu_0$.

The eigenvalue equations are transcendental equations for propagation constants of the unknown modal. Afterward that solved the eigenvalue equations, the field profiles can be obtained by substituting the modal propagation constant values β into the boundary conditions and computing the amplitudes.

If the media constituting the waveguide are lossless (ε_1, ε_2, and ε_3 are real positive numbers), the propagation constants are also real. The propagation constants of modes of the waveguide consist of the absorbing media (e.g., metal) are complex (Jiˇrí Homola, 2006). The propagation constant is related to the modal effective index n_{ef} and modal attenuation b as follows:

$$n_{ef} = \frac{c}{\omega} Re\{\beta\}\,, \qquad 2.48$$

$$b = Im\{\beta\} \frac{0.2}{ln 10}\,, \qquad 2.49$$

where $Re\{\}$ and $Im\{\}$ state the real and imaginary parts of a complex number, respectively, and c presents the speed of light in vacuum; the modal attenuation b is in $dB\ cm^{-1}$ if β is given in m^{-1}.

A case study of planar waveguide supporting surface plasmon is a thin metal film placed between two semi-infinite dielectric media (Figure 2.10). If the metal film is much thicker than the penetration depth of the surface plasmon at each metal–dielectric interface, this waveguide supports two TM modes, which correspond to two surface plasmons at the opposite boundaries of the metal film. When the metal thickness decreases, coupling between the two surface plasmons occurs, giving rise to mixed electromagnetic field modes. In this case, the metal film is gold 50nm thick.

The modes of a dielectric–metal–dielectric waveguide can be found by solving the eigenvalue equation for TM modes. For any metal film thickness, there are two coupled surface plasmons referred to as the symmetric and anti-symmetric surface plasmons according to the symmetry of the magnetic intensity distribution (J iˇrí Homola, 2006b).

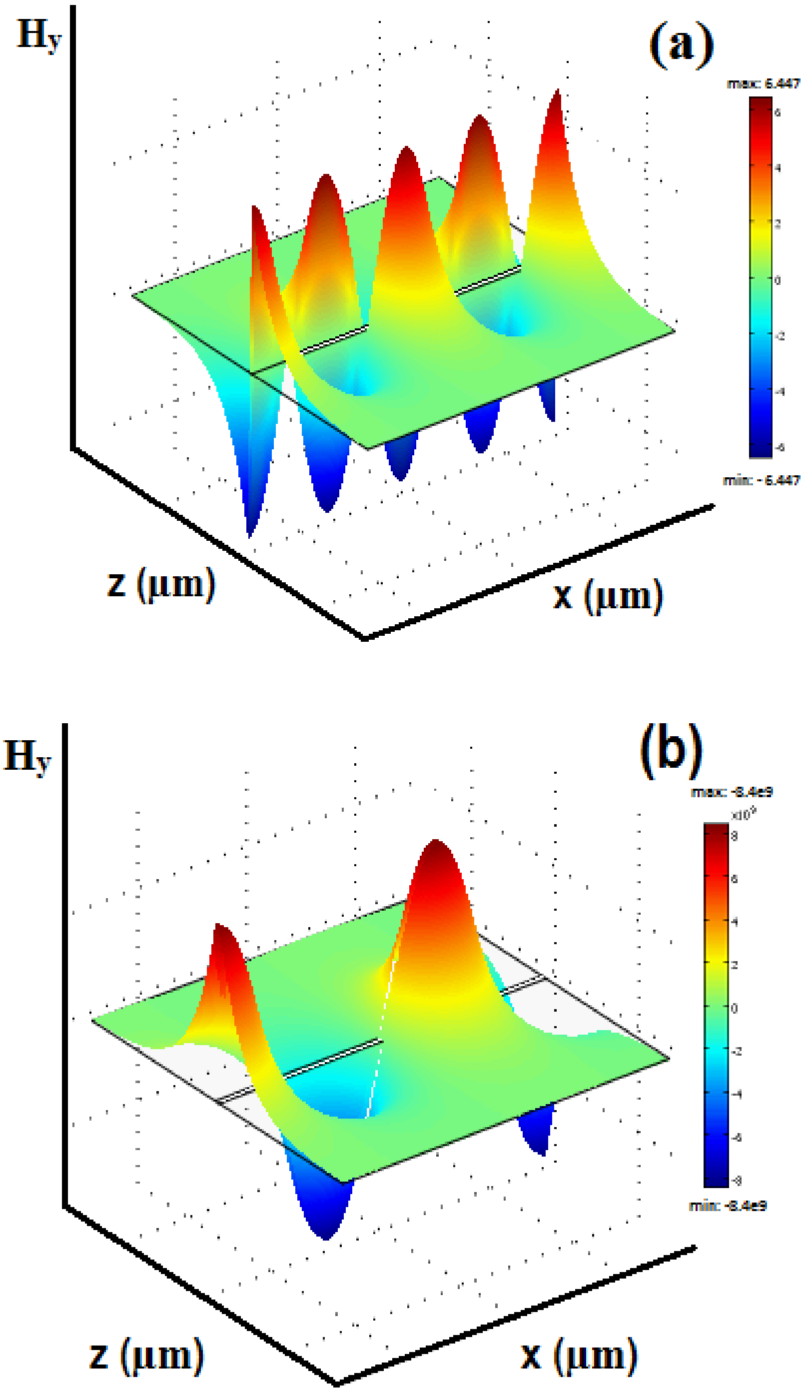

Figure 2.11 3D image of SPs propagating along a metal film (DMD structure) with (a) anti-symmetric and (b) symmetric magnetic field distribution with respect to the middle plane

2.4.3 Symmetric and anti-symmetric modes of SPs in DMD structure

In 1969, Economou (Economou, 1969) conducted the first systematic study of SPs on single as well as multilayer metal films surrounded by symmetric dielectrics. To this end, he derived the dispersion relations for different configurations by taking the Drude-Lorentz model into account (Economou, 1969). Burke and colleagues (Burke, Stegeman, & Tamir, 1986) have extended the analysis of SPs in thin metal films to asymmetric structures where the metal film is bound by two different dielectrics. They also included a detailed discussion on the effect of dissipation on the dispersion relation and classified all possible solutions of the dispersion relation.

The study of SPs in thin films is of practical importance because they are a basic structure for a finite metal stripe, currently one of the most discussed and analyzed plasmonic waveguides (Berini, 1999, 2006, 2008; Brongersma & Kik, 2007; Maier, 2007; Shalaev & Kawata, 2006; Zourob & Lakhtakia, 2010). For instance, one of the methods of determining the wave number is the effective index method (EIM). This approach basically consists of decomposing the 2D waveguide structure into two 1D structures (DMD or MDM) and matching the solution of each 1D structure. However, EIM is not only confined to rectangular structures but is also applicable for other 2D waveguide structures, such as grooves and gaps (Bozhevolnyi, 2006).

In DMD structure, two different film (plasmon) modes can be excited, depending on whether the magnetic field *H* in the film is symmetric or anti-symmetric with respect to the middle plane (see Figure 2.11).

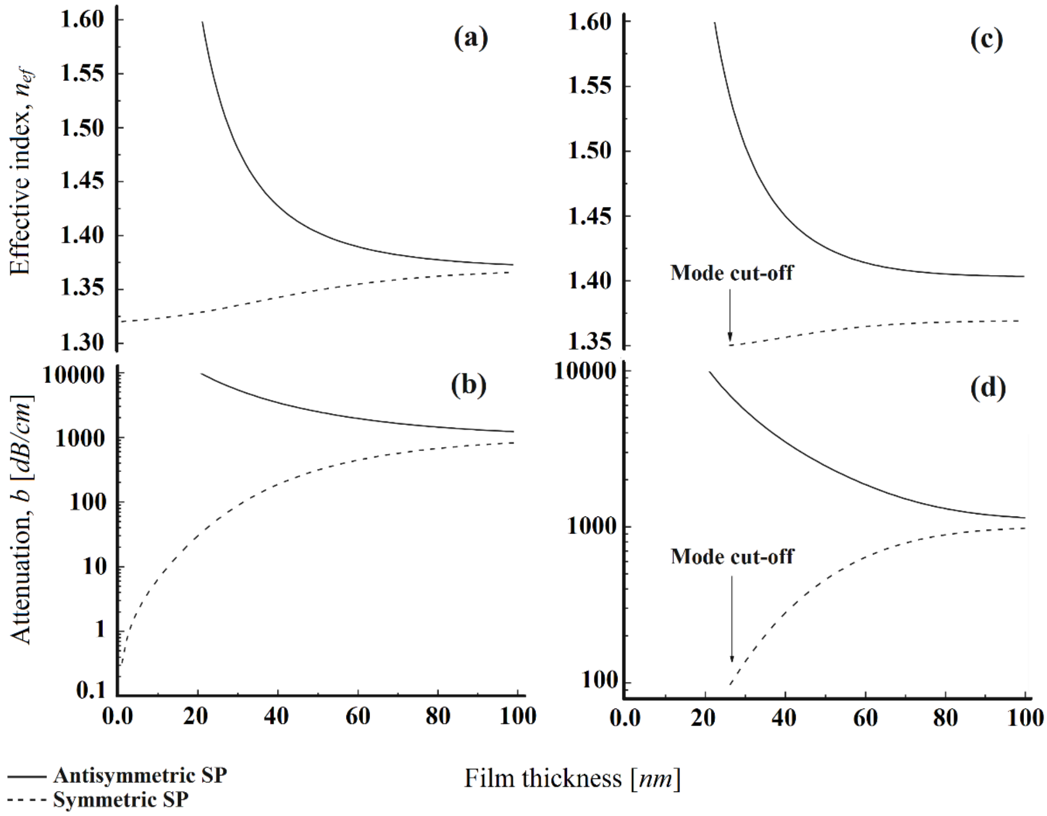

Figure 2.12 Dispersion relation $q_x(h)$, where h is the film thickness of a DMD plasmon waveguide for symmetric and anti-symmetric magnetic field H_y. Effective index and modal attenuation of surface plasmons propagating along thin gold film (ε_m= -25 + 1.44i) slotted in between two dielectrics (n_{d1}=1.32 and n_{d2}= 1.35) as a function of gold film thickness; wavelength is 800nm

For a symmetric DMD structure, the metal film is bounded on each side by the same dielectric. The dispersion relation $q(h)$ is then given by

$$tanh\frac{\alpha_m h}{2} = -\frac{\alpha_d \varepsilon_m}{\alpha_m \varepsilon_d}, \qquad 2.50$$

for the symmetric magnetic field distribution across the film (anti-symmetric charge distribution) regarding the middle plane and

$$\tanh\frac{\alpha_m h}{2} = -\frac{\alpha_m \varepsilon_d}{\alpha_d \varepsilon_m}, \qquad 2.51$$

for the anti-symmetric magnetic field distribution (symmetric charge distribution), where α_d and α_m are the reciprocal penetration depths into the dielectric and metal, respectively, and ε_d and ε_m denote the corresponding permittivity (Gramotnev & Vernon, 2007; Gramotnev, 2005; Vogel, 2009).

Thin, metal film packed amid two semi-infinite dielectric media is otherwise known as a planar waveguide that supports surface plasmons (Figure 2.10). In case the metal film is quite a bit thicker than the surface plasmon penetration depth at all metal–dielectric interfaces, such waveguide sustains two TM modes related to two surface plasmons at the metal film's opposite bounds. With decreasing metal thickness, two surface plasmons will connect resulting in mixed electromagnetic field modes.

It is possible to obtain dielectric–metal–dielectric waveguide modes by working out the eigenvalue (2.47). Figure 2.11 (a) and (b) presents the eigenvalue equation's mathematical results with respect to symmetric waveguide configuration ($n_{d1}= n_{d2}$). For any metal film thickness value two coupled surface plasmons are present known as symmetric and anti-symmetric surface plasmons consistent with the magnetic intensity distribution symmetry (Ghosh, 1998). In the symmetric surface plasmon, effective index and attenuation both evidently amplify with thicker metal film. However, the anti-symmetric surface plasmons' attenuation and effective index diminish as the metal film gets thicker. Meanwhile, for an asymmetric waveguide the symmetric surface plasmons' effective index reduces with declining metal film thickness; at a specific thickness, the symmetric surface plasmon stops being present in the form of a guided mode (Figure 2.12 (c) and (d)) an occurrence known as mode cutoff. Since a symmetric surface plasmon displays less attenuation compared to its anti-symmetric equivalent called a short-range surface plasmon (Quail & Simon, 1984; Slavík & Homola, 2007), it is occasionally identified as a long-range surface plasmon (Berini, 2009) (Quail & Simon, 1984; Slavík & Homola, 2007).

Figure 2.13 shows the field vector profiles of the symmetric and anti-symmetric surface plasmons on thin gold film surrounded by two identical dielectrics. The profiles of magnetic intensity *h* of symmetric and anti-symmetric plasmons are symmetric or anti-symmetric with respect to the center of the metal. The field of the symmetric surface plasmon penetrates deeper into the dielectric media than that of the anti-symmetric surface plasmon.

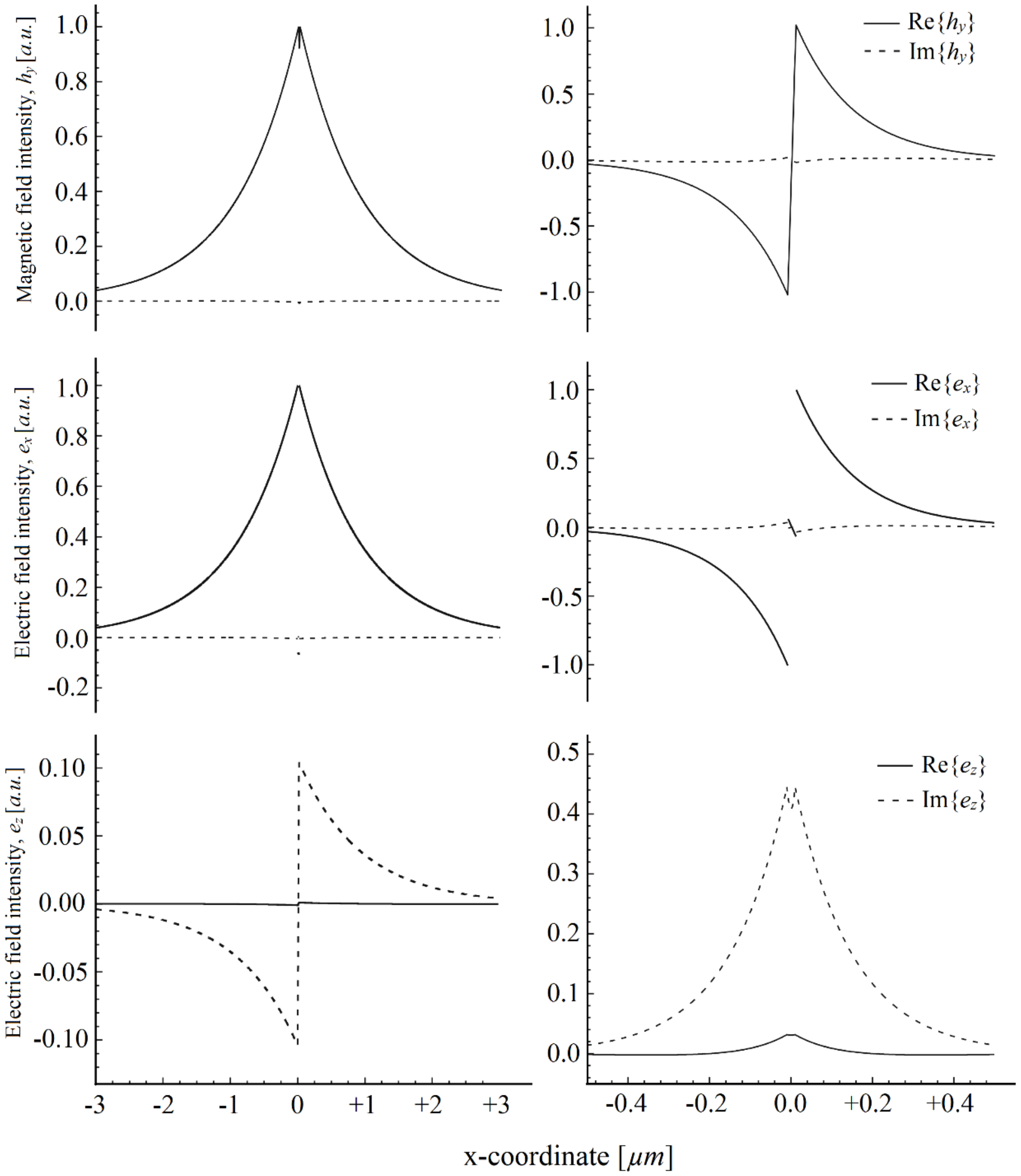

Figure 2.13 Field profile of symmetric (left side plots) and anti-symmetric (right side plots) surface plasmon on thin gold film (ε_m= – 25 + 1.44i) between two identical dielectrics (n_{d1}= n_{d2}= 1.32); gold film thickness is 20nm and wavelength is 800nm.

Figure 2.12 presents the solutions of the dispersion relations for 2.50 and 2.51 calculated for gold film surrounded by vacuum (ε_m = -25 + 1.44i (Palik, 1998), $n_{d1,d2}$=1.32 and free space wavelength of 800nm). For the symmetric mode, the real and imaginary parts of the wave number decrease with decreasing film thickness. This indicates that losses are also reduced, hence according to 2.41, the propagation distance increases with decreasing thickness. The penetration depth into the dielectric also increases and approaches infinite distance for zero film thickness h and the symmetric plasmon transforms into a bulk wave in the dielectric. For the anti-symmetric mode the penetration depth decreases into the dielectric and metal, hence the localization increases with increasing dissipation (Vogel, 2009).

The symmetric film mode in a thin metal film is also referred to as a long-range surface plasmon polariton (LRSPP). Nevertheless, the LRSPP experiences a cutoff, limiting the miniaturization of the metal stripe along with the problem of increasing field localization. In practice there is always a trade-off between reasonable propagation distances and localization (Maier, 2007). The anti-symmetric mode, on the other hand, experiences no cutoff when the film thickness h decreases. As a result, this mode can be employed for nanofocusing for the same reason as the MDM structure (Vogel, 2009).

If the metal film is bounded by two different dielectrics, the classification of symmetric and anti-symmetric modes for DMD-structures, as shown above, cannot be used without modification. For instance, a metal film is placed on a glass substrate (ε) and surrounded by vacuum or another dielectric material ($\varepsilon_c \neq \varepsilon_s$) (Burke et al., 1986; Prade, Vinet, & Mysyrowicz, 1991). The magnetic field H is neither fully symmetric nor fully anti-symmetric with respect to the middle plane. These modes are called quasi-symmetric and quasi-anti-symmetric film modes (Vernon, Gramotnev, & Pile, 2007). The dispersion relation can be derived in the same way by solving Helmholtz's equation as outlined in previous sections. However, due to structure asymmetry, four boundary conditions must be considered, but more inconveniently, the dispersion relations for the quasi-symmetric and quasi-anti-symmetric modes are expressed in one equation (Vernon et al., 2007; Vogel, 2009).

Nevertheless, a method called the zero-plane method, originally developed to analyze EM modes between two piezoelectric materials separated by a gap, simplifies the analysis (Chernozatonskii, Ermoshin, & Gramotnev, 1991; Vernon et al., 2007). This approach consists of subdividing the real asymmetric structure into two symmetric structures, solving the (known) dispersion relations in both symmetric systems and then matching the resulting solutions. The advantages are that only three boundary conditions remain and separate equations for the two types of modes are obtained (Vernon et al., 2007; Vogel, 2009).

The symmetric surface plasmon exhibits effective index and attenuation, which both increase with increasing metal film thickness. The effective index and attenuation of the anti-symmetric surface plasmon decrease with increasing metal film thickness. If the waveguide is asymmetric, the effective index of the symmetric surface plasmon decreases with decreasing metal film thickness and at a certain metal film thickness, the symmetric surface plasmon ceases to exist as a guided mode. The symmetric surface plasmon exhibits lower attenuation than its anti-symmetric counterpart and it is therefore sometimes referred to as a long-range surface plasmon, while the anti-symmetric mode is referred to as a short-range surface plasmon (Jiˇrí Homola, 2006).

As a key result, it will be confirmed in this section, that only TM-plasmons can propagate along with the metal surface. In the optical and near infrared frequency structures, the real part of the complex relative permittivity of the most of metals (gold, silver, copper and aluminum) takes on the negative values which is a basic and mandatory requirement for existing the surface plasmons (Palik, 1998).

2.5 Analysis methods applied in this study

In this section, the analytical and numerical methods employed throughout this PhD study are introduced to thoroughly analyze plasmonic resonances on thin gold film. In order to analytically study SPR structures, light ought to be propagated either within the visible wavelength range (assuming the resonance occurs within this range) with a constant SPR angle or range of incident angle with constant wavelength. Based on analytical analysis as a mathematical method (Abarbanel & Gottlieb, 1997), the SPR angle variation versus wavelength and the reflection intensity versus incident angle are calculated and assessed on the SPR structure. To numerically analyze the SPR structure, it is necessary to rely entirely on rigorous numerical methods, such as finite element methods (FEM) (Sadiku, 2010), finite difference time domain (FDTD) (Hagness & Taflove, 2000; Sadiku, 2010) or methods of moments (MoM) (Gibson, 2007).

2.5.1 Analytical Analysis

From a mathematical point of view, the scattering theory (also known as the field susceptibility or Green's dyadic technique) is based on Green's function theory applied to the wave equation when a source term is introduced. It simply describes the most general analytical solution of the inhomogeneous wave equation as an integral equation where the kernel is a Green's function (Newton, 1982). Several electromagnetic scattering theory formulations have been successfully applied to modeling near-field optical phenomena. Although Green's function may be expanded in Fourier or multi-pole series, most formulations favor a discretization in real space since near-field optical phenomena occur on a sub-wavelength scale (Girard & Dereux, 1996). Until now, most analytical analyses of surface plasmon resonance have been implemented in MATLAB software. All mathematical analysis is solved by this software according to the theoretical description of wave equations and electromagnetic fields given in prior sections of this chapter.

Although the surface plasmon resonance phenomenon can be modeled analytically for bio-interaction analysis, analytically modeling a strip of metal bounded with dielectric medium is not enough. Thus, for slab structure bio-interaction analysis, solving the eigenvalue equations requires numerical calculation and cannot only be evaluated analytically.

2.5.2 Numerical Analysis

The finite element method (FEM), or finite element analysis (FEA), is a numerical computation technique used to obtain approximate solutions of boundary value problems (Brenner & Scott, 2008; Garg, 2008). Simply stated, a boundary value problem (BVP) is mathematical, whereby one or more dependent variables must satisfy a differential equation everywhere within a known domain of independent variables and satisfy specific conditions on the domain's boundary. The extensive use of FEM in solving the BVP of different disciplines has led to the production of lots of computational software such as COMSOL Multiphysics. It is recognized for its flexibility and multidisciplinary modeling capability.

In this work, COMSOL is employed to study of surface plasmon resonance (Ziegel, Press, Flannery, Teukolsky, & Vetterling, 1987). COMSOL includes a powerful radio frequency module that is suitable for analyzing optical phenomena and has been accepted as a trustworthy result generating suit (Englebienne, Hoonacker, & Verhas, 2003; J iˇrí Homola, 2006a, 2006b).

The physical interpretation of FEM is closely related to the method's discovery and extensive use in the field of structural mechanics in the early 1940s (Courant & others, 1943; Meek, 1996). The fundamental concept in the physical interpretation is the breakdown of a complex mechanical system into simpler, disjointed components called finite elements (Huebner, Dewhirst, Smith, & Byrom, 2008). The physical response of an element is characterized in terms of a finite number of degrees of freedom. These degrees of freedom are represented by values of unknown functions as a set of node points. The element response is defined by algebraic equations constructed from physical or energy specifications. The response of the original system is approximated by that of the discrete model constructed by connecting the elements. Therefore, a physical look would indicate that electromagnetic fields could be solved for each element and connected to form a whole physical model by applying the correct boundary conditions and physical approximations/assumptions. The main advantage of FEM, especially over grid-based methods such as FDTD, is with discretization/meshing. Mesh elements in FEM can be triangular and irregular in arrangement (Volakis, Chatterjee, & Kempel, 1998). The mesh provides details about where every element is and to which material in the simulation domain it associates with, and it approximates the domain's geometrical shape. How well the geometrical shapes are resolved in the domain contributes to the stability and accuracy of the solution in addition to the resources used. Mesh characteristics of FEM modeling are recognized as more efficient than conventional FDTD mesh (Garg, 2008). This is because the non-regular triangular FEM mesh can resolve different, arbitrary, small geometries better than the regular rectangular mesh typically employed by FDTD. However, as emphasized throughout this thesis, FEM is applied for numerical analysis of the SPR structure.

2.6 The application of surface plasmons in sensing

Generally, surface plasmon resonance (SPR) has a function in three major areas (Jiří Homola et al., 1999): measurement of physical quantities, chemical sensing and biosensing. SPR sensors are utilized to measure physical quantities such as displacement (G Margheri, Mannoni, & Quercioli, 1997) and angular position (Schaller, Czepluch, & Stojanoff, 1997). Humidity sensors (Qi, Honma, & Zhou, 2006; Weiss, Srivastava, & Groger, 1996) and temperature sensors (Chadwick & Gal, 1993; Turhan-Sayan & others, 2003) using SPR have been developed. In the field of chemical sensing (Jiří Homola et al., 1999), SPR is used to monitoring the distillation process (Ruiz et al., 1993), gas detection (Abdelghani et al., 1997; Liedberg et al., 1983) and detecting Cu and Pb ions (Chinowsky, Saban, & Yee, 1996; Jung, Saban, Yee, & Darling, 1996) by combining SPR with anodic stripping voltammetry. Some of the SPR biosensing applications include protein-protein or protein-DNA interaction assessment (Mernagh, Janscak, Firman, & Kneale, 1998), plasma membrane examination (Kim et al., 1998), as well as DNA detection (Goodrich, Lee, & Corn, 2004), bacteria (Koubova et al., 2001), herbicides (Mouvet et al., 1997), and protein toxins (Ji\vr\í Homola et al., 2002).

A commercial system derived from the SPR technique has been applied to measure a wide range of real-time bio-molecular interactions. It is possible to characterize ligand-analyte binding reactions without labeling requirements. The incident laser light is reflected from the inner face of the prism, which has its outer face coated by a layer of thin noble metal film, i.e. gold in a common SPR setup. The intensity of reflected light is lost in producing a resonance in electrons on the thin metal film at a unique angle (Berini, 2009). Since this unique angle is dependent on the refractive index of the material on the thin metal surface, this phenomenon has therefore been applied to demonstrate molecular interactions in solid-liquid interfaces. One reactant (a ligand) is immobilized on the gold surface and another reactant (an analyte) flows on the gold surface. When antibodies (Abs), acting as the analyte, and antigens (Ags) as the ligands, interact to bind each other, the response is produced and monitored in real-time. The SPR biosensors measure the refractive index changes in the vicinity of the immobilized surface ligands (Tanious, Nguyen, & Wilson, 2008).

Surface Plasmon Resonance offers a new generation of label-free, real-time analysis of bio-molecules, providing information on kinetic processes, concentration and real-time molecule detection (Chen, Chien, Lin, & Lee, 2004; Dostálek & Knoll, 2008; Ji\vrí Homola, 2003; Jiří Homola et al., 1999; Yonzon et al., 2004). Label-free detection means that the analyte does not need to be labeled by fluorescent molecules. A label-free, real-time detection technique offers advantages over an alternative technique, such as fluorescence-based sensors. These methods also provide high sensitivity, but they require either multi-step detection protocols, which limit the real-time measuring ability, or suffer from cross-sensitivity to the non-target analyte (Ji\vrí Homola, 2003), something that reduces accuracy. The first commercial SPR application in biosensing was by Biacore International AB in 1990 (Ji\vrí Homola, 2003). Biacore (“General Electric Company, Biacore,” 2014) is one of the initial SPR instruments and market leaders, especially for larger pharmaceutical companies. Companies such as Nomadics (“I. Nomadics, Sensiq website,” 2014) and Reichert (“Reichert, Inc. , Reichert Surface Plasmon Resonance (SPR) Systems,” 2014) also produce surface plasmon resonance sensors for real-time binding information detection.

3 CHAPTER III: METHOD AND PROCEDURE

3.1 Overview

The configuration and modeling of the proposed SPR biosensor, along with experimental method, are described in this chapter. In the first section, the four common models of optical properties are introduced for analyzing them on SPR structure through analytical and numerical analysis. All models have been implemented using MATLAB programming. There is a comparison between common models and reference data in this section as well. The reason why gold is used in this study and molecular interactions in SPR sensors are explained in the following chapter. In addition, the dielectric-metal-dielectric waveguide is modeled to state the dimension and optical properties of the proposed SPR structure, which affect the surface plasmons. The molecular interactions in modeling the SPR biosensors is briefly explained in this Chapter. The last section is devoted to the method of our experiment. First, the simple SPR biosensor experiment is explained and subsequently the terms and required equipment are described in detail.

3.2 Optical properties of metallic films

In order to design, and analytically and numerically study of multilayer structures containing metal-dielectric films, accurate knowledge of the optical properties of such films is required. The reason is that the optical properties of thin metal-dielectric are strongly dependent on incident wavelength and film thickness. Therefore, the common models for optical properties of thin metallic films are explained. Moreover, The reference data of optical properties of proposed thin films in specific wavelength is stated in following subsection.

3.2.1 Common models for optical properties of thin metallic films

The basic model in the field of optical properties of different materials is the Drude model that almost all the other models are improvements of this model (Hertel, 2011).

Subsequently, few models was developed through experimentally nonparametric models (Amotchkina et al., 2011) that was not comprehensive. The most applicable of models based on Drude are Lorentz-Drude model (Rakic, Djurisic, Elazar, & Majewski, 1998), Brendel-Bormann model (Rakic et al., 1998), and Multi Oscillator Model (Stenzel et al., 1995). However, even these models are not well studied in different application conditions. Vial and Laroche (Vial & Laroche, 2007) described the dispersion properties of metals using Drude model versus Lorentz-Drude model. In another work (Vial, 2007), a similar model discussion has been done by introducing two critical points in the Lorentz-Drude model. Comparison of these models looks interesting but using a trustable experimental data as a reference for this kind of comparing seems to be necessary to prove the reliability of these models. Comparing nonparametric models multi-oscillator model (Amotchkina et al., 2011) and optical properties for different metallic films (Rakic et al., 1998) are examples of these thought. The experimental data used in this study is based on Optical Society of America (OSA) data sheet (Schulz & Tangherlini, 1954; Schulz, 1954).

3.2.1.1 Drude model

In the most simplified cases of time domain methods which the metal-dielectric frequency characterization is sought, the Drude model is invoked to approximate the dispersion properties of metals:

$$\varepsilon_{\mathrm{Drude}}(\omega) = \varepsilon(\infty) - \frac{(\sqrt{f_0}\omega_p)^2}{\omega(\omega - i\Gamma)}, \qquad 3.1$$

where f_0 represents the oscillator strength (weight factor) and the plasma frequency ω_p is associated with intra band transitions (free-electron transitions) and is a function of electron density and mass. Scattering frequency Γ includes all the scattering interactions like e-e, e-phonon, and etc. However, we must consider that only limited range of wavelength can be approximated by Drude model (Hertel, 2011).

3.2.1.2 Drude-Lorentz model

The Drude-Lorentz model is an improvement of Drude model by involving the explicitly separated inters band (bound-electron effects) expression to the initial model of Drude. By adding this Lorentzian term that is described by a semi quantum model, the validity range of Drude model can be extended (Rakic et al., 1998).

$$\varepsilon_{\mathrm{r,D-L}}(\omega) = \varepsilon_{\mathrm{r,Drude}}(\omega) + \sum_{j=1}^{k} \frac{f_j\ \omega_j^{2}}{\left(\omega_j^{\ 2} - \omega^{\ 2}\right) - i\ \omega\ \Gamma_j}, \qquad 3.2$$

Where ω_j and Γ_j are symbols of the oscillator resonant frequencies and bandwidths respectively, k is the number of oscillators with frequency ω_j, and f_j is oscillator strength or weighting factor. Despite the fact that the Drude-Lorentz model (D-L) expands the validity range of analytical metal-dielectric constants approximations, it is not appropriate for describing of some metals edges with sharp absorption. In some references stated that the approximation of the Drude-Lorentz model is not well acceptable for noble metals (Cu, Ag and Au) in the onset of inter band absorption even for five lorentzian terms (Rakic et al., 1998).

3.2.1.3 Brendel-Bormann model

In the broadening functions such as optical parameters in the Drude model, the Gaussian line shape functions give better results than Lorentzian line shape functions. If the same full width at half maximum (FWHM) and same weight are assumed for both of these functions, the Lorentzian function’s wings are usually more extended and higher rather than the other function. As a result, all the Lorentzian based models show immoderate absorption in spite of what is expected (Rakic et al., 1998).

The proposed model of Brendel and Bormann for solids’ dielectric function is based on a Gaussian complex error function method (J. A. C. Weideman, 1994) to reduce the deviance of Drude model from the real values. In this model the Lorantzian term in the Drude-Lorentz model is replaced by the Brendel-Bormann polynomial which is improved by means of complex error function technique. The Brendel-Bormann (B-B) optical dielectric function is:

$$\varepsilon_{B-B}(\omega) = \varepsilon(\infty) - \frac{\left(\sqrt{f_0}\omega_p\right)^2}{\omega(\omega - i\,\Gamma_0)} + \sum_{j=1}^{k} \chi_j(\,\omega) \quad 3.3$$

where *k* is the number of B-B oscillators used to interpret the inter band part of the spectrum (Rakic et al., 1998). So a flexible shape for the absorption profile is obtainable via such an analytic function.

3.2.1.4 Multi oscillator model

Perhaps the most popular model for the metal-dielectric optical properties is the Multiple Oscillator model (M-O) which is based on the material oscillator models. In the infrared and visible spectral ranges, the wavelength dependencies in optical indices for thin metal films are very complicated and one of the models that had a very good response in this case was the Multiple Oscillator model (Djurisic, Fritz, & Leo, 2000; Stenzel et al., 1995).

$$\varepsilon_r(\omega) = \varepsilon(\infty) - \frac{f_0\omega_p^2}{\omega^2+\Gamma_0^2} + \sum_{j=1}^{k} \frac{f_j\omega_{pj}^2\left(-\omega^2+\omega_{pj}^2\right)}{\omega^2\Gamma_j^2+\left(-\omega^2+\omega_{pj}^2\right)^2}\,, \quad 3.4$$

$$\varepsilon_i(\omega) = \frac{f_0\omega_p^2\Gamma}{\omega\left(\omega^2+\Gamma_0^2\right)} + \sum_{j=1}^{k} \frac{\omega f_j\Gamma_j\omega_{pj}^2}{\omega^2\Gamma_j^2+\left(-\omega^2+\omega_{pj}^2\right)^2}\,, \quad 3.5$$

$$\varepsilon_{M-O} = \varepsilon_r + i\varepsilon_i, \quad 3.6$$

Here we separate the real and imaginary part of the model to make it more understandable. In these terms ω_{pj} is the plasmonic resonant frequency of the oscillators and Γ_j is its related bandwidths. Again f_j is weighting factor and *k* is the oscillators counter.

3.2.2 Reference data of optical properties of proposed thin films

To prove the accuracy of each presented methods in the modeling of optical properties of gold, the modeling simulation results should be compared with experimental data. Since experimentally determination of refractive indices and extinction coefficients is very difficult, the experiments on this category are so rare. However, Schulz in 1954, published the absorption coefficients of some metals including gold (Schulz, 1954) which is used in this study. For the refractive indices, another database which was a collaboration of Schulz and Tangherlini is applied in this study (Schulz & Tangherlini, 1954). The measured optical constants in those datasheets have been done at the wavelength range of 450nm to 950nm with the incidence angle of 45 degree at glass/air-metal interfaces. Table 3.1 displays the experimental data used in this study. In this table the refractive index and absorption coefficient is related to the proper wavelength in the range of the modeling. The refractive index and absorption coefficient of titanium are presented in Table 3.2.

Table 3.1 Refractive index (n_r) and absorption coefficient (n_i) of gold (Schulz & Tangherlini, 1954; Schulz, 1954)

λ (nm)	n_r	n_i
450	1.40	1.88
500	0.84	1.84
550	0.34	2.37
600	0.23	2.97
650	0.19	3.50
700	0.17	3.97
750	0.16	4.42
800	0.16	4.84
850	0.17	5.30
900	0.18	5.72
950	0.19	6.10

Table 3.2 Refractive index (n_r) and absorption coefficient (n_i) of titanium (Schulz & Tangherlini, 1954; Schulz, 1954)

λ (nm)	n_r	n_i
1940	3.51	5.19
1610	3.69	4.70
1390	3.67	4.37
1220	3.62	4.15
1090	3.5	4.02
984	3.35	3.97
892	3.29	3.96
821	3.21	4.01
756	3.00	4.01
704	2.86	3.96
659	2.76	3.84
617	2.67	3.72
582	2.60	3.58
549	2.54	3.43
521	2.44	3.30
496	2.36	3.19
471	2.32	3.10
451	2.27	3.04
431	2.21	3.01
413	2.14	2.98
397	2.08	2.95
381	1.99	2.93
368	1.90	2.90
354	1.82	2.87
342	1.72	2.82
332	1.61	2.74
320	1.55	2.66
311	1.50	2.57
301	1.45	2.46
292	1.40	2.36
284	1.35	2.26
276	1.30	2.17
269	1.27	2.07
262	1.27	1.99
255	1.26	1.91
249	1.27	1.83
243	1.28	1.77
237	1.30	1.72
231	1.31	1.68
226	1.32	1.66
221	1.32	1.66
216	1.32	1.67
212	1.31	1.68
207	1.31	1.69
203	1.27	1.69

3.3 Method of analytical and numerical analysis on SPR configuration

In recent years, researchers were struggling to accurately model electro-magnetic processes whether in optical nano-scaled metal-dielectric composites or optical surface plasmonics, analytically and numerically. The thin metal films and specially metal-dielectric structures are increasingly used in various fields of bio-sensing, due to high sensitivities. So there is a high potential to study these metal films. In this study, the proposed SPR biosensor (as known dielectric-metal-dielectric structure) is analyzed analytically and numerically in addition to experiments.

3.3.1 Analytical analysis of SPR configuration

In this part that is done with the MATLAB software, we introduce a multilayer structure with specific optical properties in every layer. The percentage of reflectance and plasmonic resonance angle (SPR angle) in separate calculation is desired for this purpose. In fact the wavelength of the incident beam is the variable used for calculating the SPR angle. Since the optical properties of the target are directly related to the wavelength, we can compare the models in the plots obtained from the calculations. The same conclusion can be taken from the result of reflectance computation, in various incident angles with specific wavelength. In this analysis, the thickness of layers is the only parameter related to the structure that must be denoted.

3.3.1.1 Refection and transmission of polarized light by stratified planar structures

The analytical solution considers a stratified structure that consists of a stack of m parallel layers, sandwiched between known two semi-infinite layers. The first layer is layer *1* and the last layer is layer *N*. The analysis assumes that the layers are all linear, homogeneous and isotropic. For a layer with index *j*, the thickness is noted as d_j, and the refractive index is noted as Z_j. A monochromatic plane wave incident on the layer *1*, yields a resultant reflected field in layer *1* and a resultant transmitted field in layer *N*. In each layer, there is a resultant field travelling forward (denoted as positive) and backwards (denoted as negative) directions. The geometry and the direction conventions are shown in Figure 3.1. In this section the main focus is on the p-polarized waves since p-polarized waves can excite plasmons. (For details and the derivation of these equations and for expressions in s-polarizations, refer to (Azzam & Bashara, 1987)).

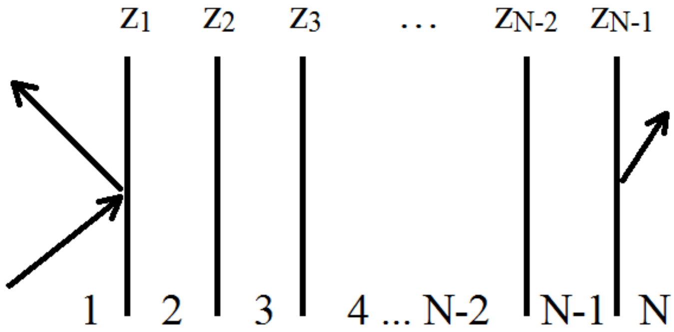

Figure 3.1 N-layer model for SPR measurement.

The tangential fields at the first boundary $z=z_1=0$ are related to those at the final boundary $z=z_{N-1}$ by

$$\begin{bmatrix} U_1 \\ V_1 \end{bmatrix} = M_2 M_3 \dots M_{N-1} \begin{bmatrix} U_{N-1} \\ V_{N-1} \end{bmatrix} = M \begin{bmatrix} U_{N-1} \\ V_{N-1} \end{bmatrix}, \qquad 3.7$$

For p-wave at boundary k,

$$U_k = H_y^T + H_y^R, \qquad 3.8$$

$$V_k = E_x^T + E_x^R, \qquad 3.9$$

and

$$M_k = \begin{bmatrix} \cos\beta_k & -i\sin\beta_k/q_k \\ -iq_k\sin\beta_k & \cos\beta_k \end{bmatrix}, \qquad 3.10$$

Here
$$q_k = (q_k/\tilde{\varepsilon}_k)^{1/2}\cos\theta_k, \qquad 3.11$$

$$\mu_k \cong 1, \qquad 3.12$$

and where, q_k is defined as:

$$q_k \cong (1/\tilde{\varepsilon}_k)^{1/2} \cos\theta_k = \frac{\left(\tilde{\varepsilon}_k - n_1^2 sin^2\theta_1\right)^{1/2}}{\tilde{\varepsilon}_k}, \qquad 3.13$$

and the phase factor is expressed by

$$\beta_k = \frac{2\pi}{\lambda_0} \tilde{n}_k \cos\theta_k \,(z_k - z_{k-1}) = (z_k - z_{k-1}) \frac{2\pi}{\lambda_0} (\tilde{\varepsilon}_k - n_1^2 sin^2\theta_1)^{1/2}, \qquad 3.14$$

in which case the design is considered by defining the arbitrary layer as thickness d_k (= z_k - z_{k-1}), dielectric constant $\tilde{\varepsilon}_k$, and refractive index $\tilde{n}_k$.

The interaction of the light wave and the SPP can change the characteristics of light wave, such as the totally reflected intensity r^p is:

$$r^p = \frac{(M_{11}+M_{12}q_N)q_1 - (M_{21}+M_{22}q_N)}{(M_{11}+M_{12}q_N)q_1 + (M_{21}+M_{22}q_N)}, \qquad 3.15$$

where, $M_{ij} = \left(\prod_{k=2}^{N-1} M_k\right)_{ij},\ i,j = 1{,}2$

M is the characteristic matrix of this structure which is given by

$$M_k = \begin{bmatrix} \cos\beta_k & -i\sin\beta_k \,/\, q_k \\ -iq_k \sin\beta_k & \cos\beta_k \end{bmatrix}, \qquad 3.16$$

Finally, the reflectance R for the TM-polarized light of the complete multilayer structure is described by

$$R_p = |r^p|^2, \qquad 3.17$$

The transmission coefficient for p-wave (TM) is

$$t_H^p = \frac{2q_1}{(M_{11}+M_{12}q_N)q_1 + (M_{21}+M_{22}q_N)}, \qquad 3.18$$

$$t_E^p = \frac{\mu_N n_1}{\mu_1 \tilde{n}_N} t_H^p, \qquad 3.19$$

$$T_p = \frac{\mu_N R_e\left(\tilde{n}_N \cos\theta_N / \tilde{n}_N^2\right)}{\mu_1 n_1 \cos\theta_1 / n_1^2} \left|t_H^p\right|^2, \qquad 3.20$$

For s-wave (TE) the above equations hold except

$$q_k = \sqrt{\frac{\tilde{\varepsilon}_k}{\mu_k}} cos\theta_k, \qquad 3.21$$

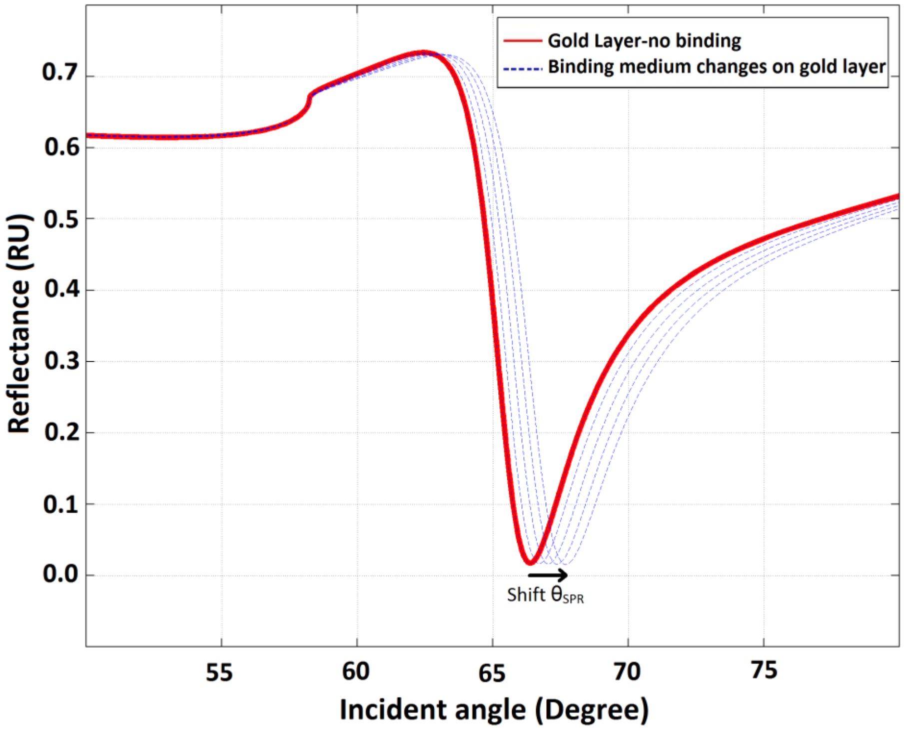

Figure 3.2 SPR curve (red line) with the BK7 galss prism|gold|air, and SPR curves (blue lines) with the BK7 prism|gold|binding medium|air configurations.

For sensing applications, surface functionality via specific binding is necessary. This binding results in refractive index change, which is reflected by 3.17. The binding medium layer is clearly seen as the shift of the SPR angle as shown above.

The MATLAB program solves the mathematical calculations based on analytical analysis which have been introduced previously, and the results will be shown in the next chapter with comprehensive discussions.

3.3.2 Numerical analysis of SPR configuration

FEM is a general variational method, which finds a variational function whose minimum/maximum/stationary point corresponds to the solution of the partial differential equations (PDE) subject to certain boundary conditions. Its application to EM problems can be done through the Maxwell's equations in the frequency domain. Finite element method analysis of a problem consists of few general steps in this study which are as follows:

- Defining the required global parameters
- Modeling the proposed SPR configuration in design environment
- Meshing the model domain so that the simulated material is homogeneous on each element
- Deriving the governing equation for an element
- Assembly of all elements into a system of equations
- The solution of the system of equations based on electric/magnetic field and power flow of structure.

A given problem is divided into many sub-problems that are easier to solve, via a process called meshing. The problem is said to be divided into a finite number of elements. Different shapes may be used for elements depending on the geometry to be resolved and the computational resources available. Throughout our numerical studies in this thesis, triangular and rectangular mesh elements (selection based on different structures) are considered.

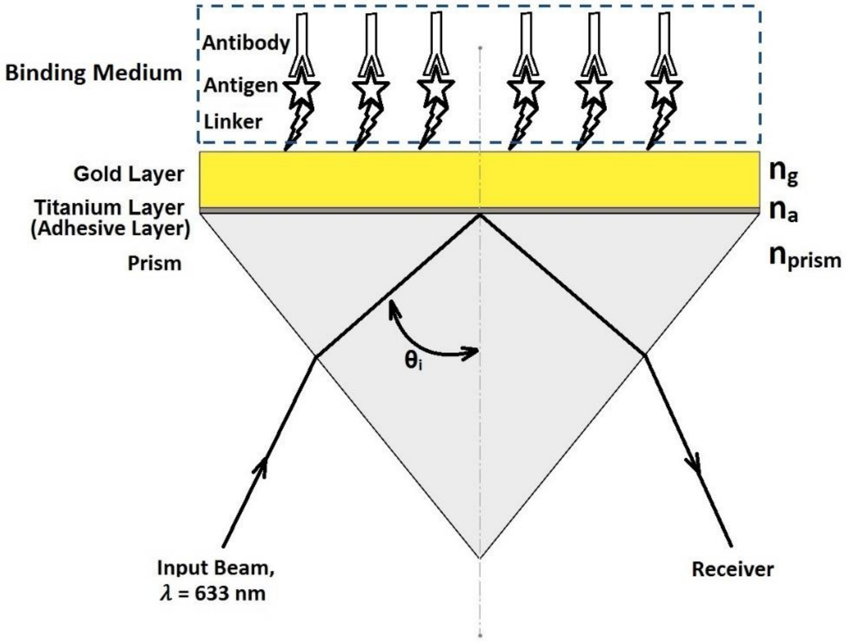

Figure 3.3 The scheme of SPR structure for numerical modeling

The SPR optical unit is composed of a source of a light beam with free space wavelength 633nm that passes through a prism (fused silica with refractive index 1.457) and struck the sensor surface at the angle, so that the beam is fully reflected. Under these conditions, an electromagnetic component of the beam, the evanescent wave, spreads into the binding medium and can interact with mobile electrons in the gold film on the glass surface. At this incident angle and specific wavelength, the surface plasmon wave of excited electrons is produced at the gold layer (thickness ~50nm) and is taken as a reduced reflective light intensity at the detector. In practice, the linker, i.e. carboxymethyl dextran matrix (thickness ~100nm) and other binding medium layers are located on top of the gold layer, respectively.

Figure 3.3 shows the configuration of the proposed carboxymethyl dextran matrix-on-gold surface plasmon resonance biosensor, where the gold surface is covered with a fused silica prism. A light wave (of vacuum wavelength λ_0) passes through the prism and is totally reflected at the prism-metal interface, generating an evanescent wave. This evanescent wave can penetrate the thin gold layer and propagate along the x direction with propagation constant $k_x = n_{prism}\left(\frac{2\pi}{\lambda_0}\right)\sin\theta_1$, where θ_1 is the light incident angle in the first medium (prism). The propagation constant k_x can be adjusted to match that of the surface plasmon polariton (SPP) by controlling the angle of incidence. The numerical angle change can be calculated using complex Fresnel equations based on the finite element analysis (Englebienne et al., 2003; Verma, Gupta, & Jha, 2011).

3.4 Implementation of the proposed SPR structure

In this section, the proposed SPR configuration and all applied materials for each layer are defined.

3.4.1 Use of gold as the metal layer

Gold and silver are the most suited metals for surface plasmon resonance sensing. Silver has better surface plasmon resonance characteristics than gold, because of the larger real part of its dielectric constant (Ordal et al., 1983). However, silver has poor long-term stability. Gold is more environmentally stable, is chemically more inert, has lower reactivity, does not react with commonly used fluids such as water and alcohols, and is compatible with a wide range of chemicals. Thus, gold is used as the metal layer in our studies whether analytical or numerical analysis.

3.4.2 Surface plasmons on dielectric-metal-dielectric waveguides

Structure of the model for study of surface plasmon consists of a thin metal film surrounded with two dielectric layers, dielectric *I* as substrate and dielectric *II* as analyte; (Figure 3.4). Assuming that the metal film is a 30nm thick gold with width of 300 nm in our design; based on Homola’s book. The surrounding dielectric is considered to be infinite. To analyze the structure for symmetric surface plasmon mode, the refractive index of substrate and analyte were made equal (J iˇrí Homola, 2006b). The surface plasmon is supported by mode analysis of its cross section for studying the capability of this configuration. The infinite dimensions of dielectric are not practical for this simulation. Therefore we used a combination of dielectric depth and width, plus the boundary conditions. For mode analysis, we assume that both width and depth of the structure are 1µm. It is also assumed that the outer boundaries of the structure are defined as perfect electric conductors.

The structure was analyzed for free space wavelength of 800nm (based on (J iˇrí Homola, 2006b)), at which the refractive index of dielectrics are $n_{dI,dII} = 1.32$ and the permittivity of gold is $\varepsilon_m = -25 + 1.44i$.

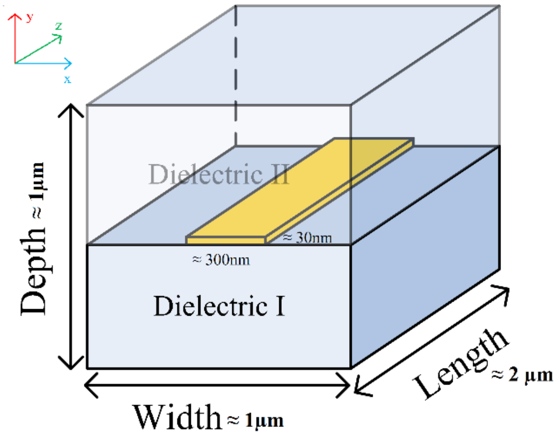

Figure 3.4 Configuration of the modeled structure in this study

Based on the result of the analysis this structure supports only one surface plasmon mode with the effective mode index of $n_f = 1.4604+0.0260i$. The electric and magnetic field distributions of the mode are presented in results and discussions.

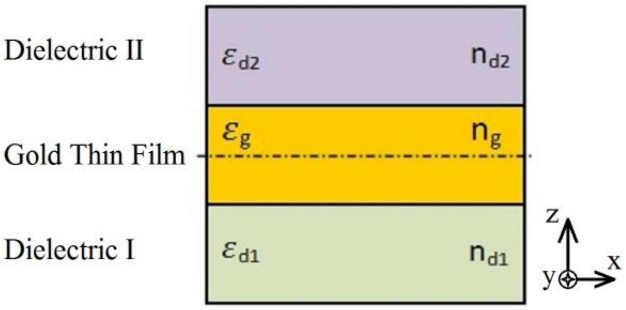

Figure 3.5 The SPR structure, dielectric II-gold-dielectric I waveguide structure

As it is shown in Figure 3.5, there is a planar waveguide supporting surface plasmon in a thin metal film sandwiched between two semi-infinite dielectric media. If the metal film is much thicker than the penetration depth of a surface plasmon at each metal–

dielectric interface, this waveguide supports two TM modes, which correspond to two surface plasmons at the opposite boundaries of the metal film. When the metal thickness decreases, coupling between the two surface plasmons occurs, giving rise to mixed modes of electromagnetic field. The modes of a dielectric–metal–dielectric waveguide can be found by solving the eigenvalue equation for TM modes. For any thickness of the metal film, there are two coupled surface plasmons based on the symmetry of the magnetic intensity distribution which are referred as the symmetric and anti-symmetric surface plasmons (Jiří Homola et al., 1999).

The symmetric surface plasmon exhibits effective index and attenuation, which both increase with an increasing metal film thickness. But, effective index and attenuation of the anti-symmetric surface plasmon decrease with an increasing thickness of the metal film. If the waveguide is asymmetric, the effective index of the symmetric surface plasmon decreases with a decreasing metal film thickness and at a certain metal film thickness, the symmetric surface plasmon ceases to exist as a guided mode. The symmetric surface plasmon exhibits a lower attenuation than its anti-symmetric counterpart and therefore it is sometimes referred as a long-range surface plasmon, while the anti-symmetric mode is referred as a short-range surface plasmon (Jiří Homola et al., 1999).

3.5 Molecular interactions in modeling the SPR biosensors

Binding or unbinding of biomolecules at the active surface of a SPR biosensor is one of the most significant issues. This issue could be evaluated using analytical and numerical analysis before experimental assessment. The determination of binding kinetics provides important new information about interacting molecules. This is commonly considered one of the greatest advantages of the SPR biosensor technique. Although in ideal cases an appropriate kinetic model of molecular interaction is able to completely describe the SPR biosensor response, in reality the influence of hydrodynamic conditions often has to be taken into account. This study devotes the molecular interaction layer in SPR configurations that correspond to the binding processes at SPR biosensor surfaces.

As mentioned earlier, the SPR is a surface-sensitive technique that has been widely used to monitor both chemical and biological interactions in real time, an aspect that gives it a distinctive advantage over endpoint binding assays.

3.6 Method of experiment

In this section, all experimental parts are presented, such as how to measure the relevant parameters of experiments, introducing the utilized equipment and solutions, how to calculate the main output, presenting the whole steps of an assay, and sample concentration. At the end, the samples are prepared based on the proposed concentration for doing the experiments with an optimized sample volume.

3.6.1 A simple experiment

Consider the experimental set-up depicted in Figure 3.6. When polarized light is shone through a prism on a sensor chip with a thin metal film on top, the light will be reflected by the metal film acting as a mirror. On changing the angle of incidence, and monitoring the intensity of the reflected light, the intensity of the reflected light passes through a minimum (Figure 3.6, line A). At this angle of incidence, the light will excite surface plasmons, inducing surface plasmon resonance, causing a dip in the intensity of the reflected light. Photons of p-polarized light can interact with the free electrons of the metal layer, inducing a wave-like oscillation of the free electrons and thereby reducing the reflected light intensity.

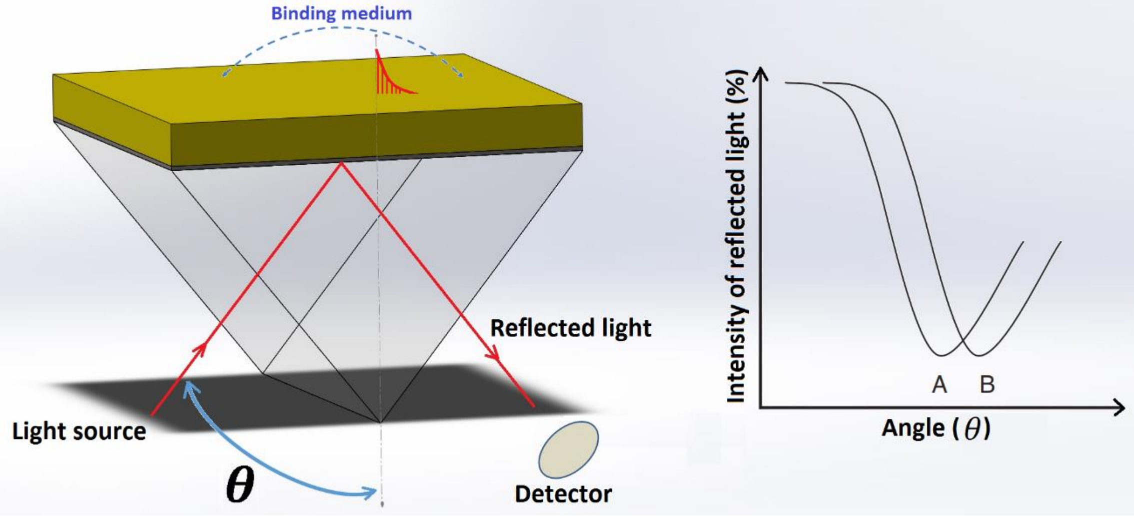

Figure 3.6 Schematic fundamental set-up of SPR excitation. A biosensor with a gold film coating is placed on a prism. The polarized light propagates from the light source on the sensor surface.

The intensity of reflected light is measured in a detector. At a certain incident angle (θ), excitation of SPs occurs, resulting in a decrease of the reflected light intensity (A). A change in optical property (refractive index) on the top surface of the gold film (termed by sensing medium) causes a shift of angle from A to B.

The angle at which the maximum loss of the reflected light intensity occurs is called resonance angle or SPR angle. The SPR angle is dependent on the optical characteristics of the system, e.g. on the refractive indices of the media at both sides of the metal, usually gold. While the refractive index at the prism side is not changing, the refractive index in the immediate vicinity of the metal surface will change when accumulated mass (e.g. bound antibodies to the immobilized antigens on the surface) adsorb on the surface. Accordingly the SPR conditions are changing and the SPR angle shift is suited to take an information on the kinetics of cell adsorption on the sensor surface.

3.6.2 Measurement of the SPR angle shift

As mentioned in chapter 2, the SPR is an accurate technique to monitor the changes of refractive index at the near vicinity of the gold surface. Figure 3.7 shows the dip shift in time, so-called a sensorgram. If this variation represents a biomolecular interaction, then such interaction kinetics can be analyzed in real time.

The angle at the intensity minimum is met will shift when the refractive index alters, where (Figure 3.7, (A)) presents the original plot of reflected light intensity versus the angle of incidence and (Figure 3.7, (B)) presents the plot after refractive index change.

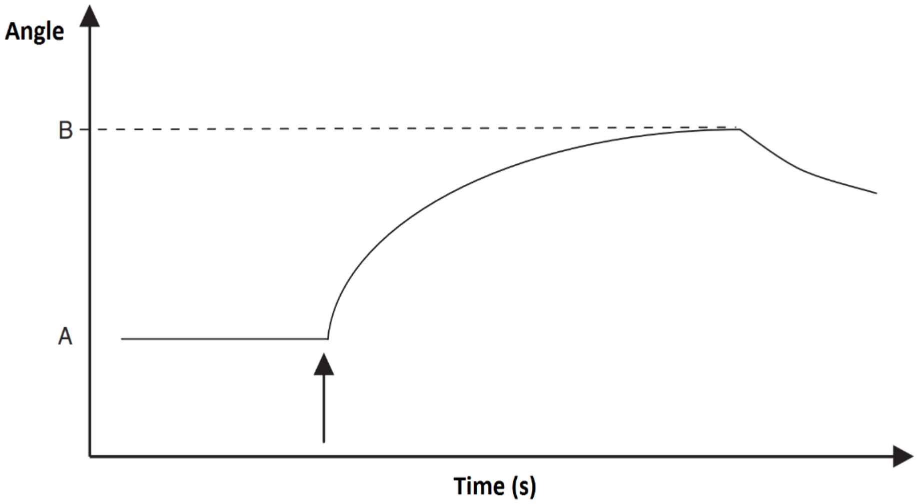

Figure 3.7 The sensorgram of angle (can be termed as resonance unit) versus time. At first, no change occurs in the sensorgram. In state A, a baseline is measured with the dip at SPR angle. After injecting the sample, which adsorbs on the sensor surface, producing a change in refractive index and consequently a SPR angle change to the state B. In real time, the adsorption–desorption procedure can be followed and then the amount of adsorbed specific biomolecular can be determined.

3.6.3 Basics of Biacore set-up and chip construction

Using the SPR method requires a detailed understanding of the physical phenomena through studying biomolecular interactions which has been described in chapter 2. It is adequate to know that the Biacore 3000 uses the SPR method to measure the refractive index near the sensor surface (within ~200 nm to the surface). The Biacore 3000 apparatus comprises three principal units which have been integrated in one device. The system consists of an optical module, liquid handling module and the sensor surface. The features of the sensor have an important influence on the quality of the ligand-analyte interaction measurement. The sensor chip forms a physical barrier between the optical unit and the flow cell.

The Biacore 3000 is an instrument with a prism coupler, also called ‘‘Kretschmann configuration’’, which has been described in chapter 2. The system shares the intrinsic phenomenon such as the direct, label-free and real-time measurement of refractive index changes at the sensor surface.

It has ability to measure the low levels of biological and chemical compounds near the sensor surface. Sensing of the biomolecular bindings occurs when the biomolecules accumulate at the surface of sensor and consequently change the refractive index of sensing medium by replacing the background electrolyte (as solutions). Antibodies have a higher refractive index than water molecules ($\Delta n \approx 10^{-1}$). The sensitivity of Biacore system is each 1000 RU corresponds to an angle change of ~ 0.1º, and 1 RU corresponds to a refractive index change of ~1×10^{-6} of proteinous material (GE Healthcare, 2008; Tanious et al., 2008).

According to CM5 biosensor structure (GE Healthcare, 2008), a glass surface covered in a thin layer (~ 50 nm) of gold, providing the physical conditions for generating the surface plasmon resonance signal. A coating on the gold layer, providing a means for attachment of the ligand. In the case of the CM5 chip, this is a 100 nm thick carboxymethyl-dextran matrix as a linker layer. This matrix provides a relatively inert hydrophilic environment suitable for most biomolecular interactions. This allows efficient immobilization from dilute solutions as well.

The SPR angle change is reported as resonance units (RU) as shown in Figure 3.8-curve A. The Figure 3.8-curve B is calculated from the sensorgram through mathematical calculations by MATLAB.

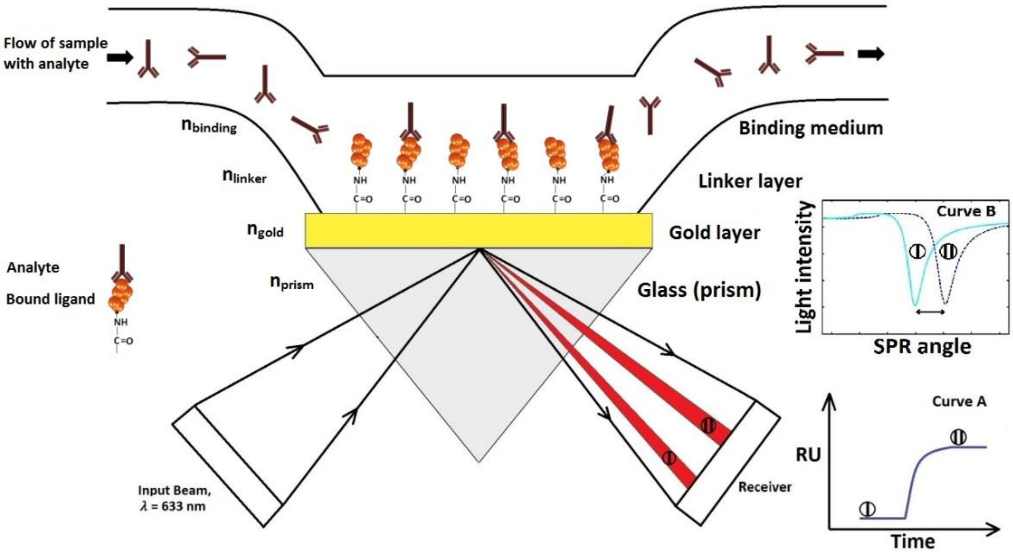

Figure 3.8 The detection approach of Biacore SPR setup. The SPR reaction is correlated to refractive index changes at the surface of biosensor, caused by changing concentration of the binding medium when the antibodies as a target bind to the immobilized antigens as a probe

3.6.4 Buffer Solutions for measuring the analysis cycle

3.6.4.1 Baseline buffer

The running, background or baseline buffer should create optimal conditions for the binding of the ligand to the analyte. For biomolecular interactions the baseline buffer is usually a physiological buffer with sufficient salt and (near-) neutral pH. Phosphate-buffered saline (PBS) is a standard baseline buffer. Alternatively, 10 mM HEPES–KOH (pH 7.4), 0.15 M NaCl is often used. The addition of a surfactant, e.g. Tween 20 (0.03–0.05%) to the buffer is favored in order to minimize non-specific binding. The surfactant not only enhances the ratio between specific and non-specific binding but also helps to prevent air bubble adsorption on the surface. However, surfactants should not be added if hydrophobic surfaces are used for non-covalent attachment of membrane bound components. Moreover, a surfactant should not be used during the immobilization cycle. Sometimes 3 mM EDTA is added to trap remaining bivalent cations (e.g. Mg^{2+} or Ca^{2+}), which may interfere with the carboxylate groups in the hydrogel layer. Blocking components may help in reducing non-specific binding, e.g. 3% BSA or HSA when patient serum is used. All buffer solutions should be prepared with Milli-Q water and preferably filtered through a 0.22 mm filter and degassed before use.

3.6.4.2 Required solutions during an assay

N-hydroxysuccinimide (NHS) and N-ethyl-N-(dimethylaminopropyl) carbodiimide (EDC) solutions (from amine coupling kit) are used to activate the surface of biosensor before injection of the ligand. Deactivation and further washing away of loosely associated ligands are performed with ethanolamine solution with pH 8.5. The 10 mM sodium acetate buffer with a pH 4.5 is used to dilute the analyte to have sufficient concentration for the assay process.

3.6.4.3 Regeneration solution

For repeated use of the same sensor chip, the surface should be regenerated by removal of analyte and any other non-covalently bound material. However, the ligand should be kept intact and should not be inactivated or denatured during the regeneration phase. Commonly used solutions for regeneration include low pH buffers, e.g. 10 mM glycine–HCl (pH 2.0). Optimal sensor regeneration includes a pH shock and regeneration is preferably performed as two consecutive steps of, for instance, 30 s each, rather than one step of 60 s. If the ligand or analyte cannot withstand low pH, sometimes a high alkaline pH is used, e.g. 10 mM NaOH (pH >11). Alternative regeneration solutions have a high salt concentration and the salts used include chaotropic agents that are chemicals, such as urea and guanidine hydrochloride, that disrupt hydrogen bonding in aqueous solutions.

3.6.5 From surface plasmon to SPR signal

Real-time and label-free biomolecular interaction sensing is unthinkable at present without the surface plasmon resonance principle. The SPR technique, liquid handlings and the sensor chip are integrated in the Biacore 3000 as depicted in Figure 3.9.

Figure 3.9 Biacore 3000 system with controller unit

As discussed in Chapter 2, the SPR causes an intensity decrease or dip in the reflected light at the sensor surface. In the following, the relationship between the intensity decrease in reflected light and sensorgram curve are illustrated. In Figure 3.10, a sensorgram of analyte binding versus time is presented, together with a rotated view of an SPR dip. While the SPR angle is the most representative parameter of the biomolecular interaction process in time, one should follow the angle of the SPR minimum (dip). As the dip shifts in the left section from A to B, the SPR dip is followed in the right section of Figure 3.10. The angle shift as a function of time is also shown.

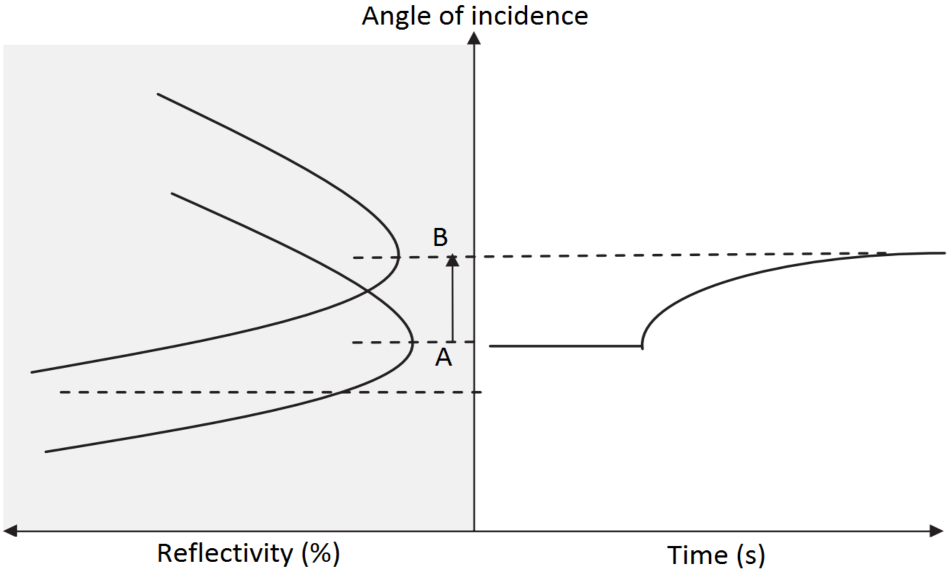

Figure 3.10 Rotated presentation of the SPR dip (left section) that forms directly the pointer of the sensorgram (right section). The angle shift of the SPR dip is determined (left, A to B), followed by plotting the angle of the SPR minimum in the sensorgram vs. time (right). Here the SPR dip minimum of the initial curve (A) shifts with time towards a larger angle (B).

Usually, the SPR curve is measured or fitted and the angle of the SPR dip is determined, followed by plotting the angle of the SPR minimum in the sensorgram (right part of Figure 3.10). A sensorgram can be obtained from a monochromatic light source using the SPR dip shift (y-axis in RU or millidegrees), as shown in Figure 3.10.

From the theory described in Chapter 2, the amount of biomolecules accumulated in the evanescent field results in an (almost) linear shift of the SPR dip. Therefore, only real-time measurement of the SPR dip as indicated in Figure 3.10 is the preferred mode of operation. Reflectivity change is only a derivative parameter of this shift. Therefore, optimally the SPR dip shift should be detected continuously to follow changes at the surface, e.g. a biomolecular interaction event. The angle shift expresses in response units in the Biacore 3000.

3.6.6 Cycle of virus detection using scanning SPR imaging

In our study, the instrument for biomolecular interaction sensing by imaging SPR (Biacore 3000) is used for rapid diagnostic test of dengue fever. Fixed-angle instrument in the Kretschmann configuration (as discussed in chapter 2) are based on the relationship between a small change in the intensity of the reflected light and the mass of bound analyte, i.e. a fixed incident light angle is employed and mass changes are estimated from the intensity of the reflected light. However, the applicable dynamic range and linear relationship of this experimental setup are limited and the optimal incident angles of each spot of a microarray differ considerably when ligand or analyte panels with different molecular weights are monitored, as explained in Chapter 2. Therefore, choosing one fixed angle to monitor many biomolecular interactions in a microarray will result in only qualitative data. Kinetic rate constants, however, require accurate quantitative data including subtraction of ‘‘bulk effects’’ for all the spots of the microarray simultaneously.

Biacore 3000 consists of a processing unit with liquid handling and optical systems and a PC running Biacore 3000 Control Software. Sensor chips and other consumables are available from GE Healthcare. As shown in Figure 3.11, Biacore 3000 processing unit houses the following components:

- two liquid delivery pumps, one for maintaining a constant flow of liquid over the sensor chip surface and the other for handling samples in the autosampler
- the autosampler, for preprogrammed sample handling including mixing and injection to the detector unit as well as sample recovery
- the Integrated μ-Fluidic Cartridge (IFC), containing liquid delivery channels, sample loop and valves
- the detector unit , including optical and electronic components for creating and measuring SPR response
- 4 detector flow cells formed by the IFC pressing against the sensor chip
- microprocessors for controlling pumps, autosampler and IFC valves, and for basic processing of the SPR signal.

The removable sensor chip is inserted into the cassette port on the detector unit, and docks into the instrument to form one side of the detector flow cell. The IFC is connected to the buffer supply through the connector block, which has an injection port for loading samples into the IFC.

The door to the autosampler and buffer compartment is locked during instrument operation, to protect the operator from injury by the moving needle of the autosampler. The instrument cannot be operated with the door open.

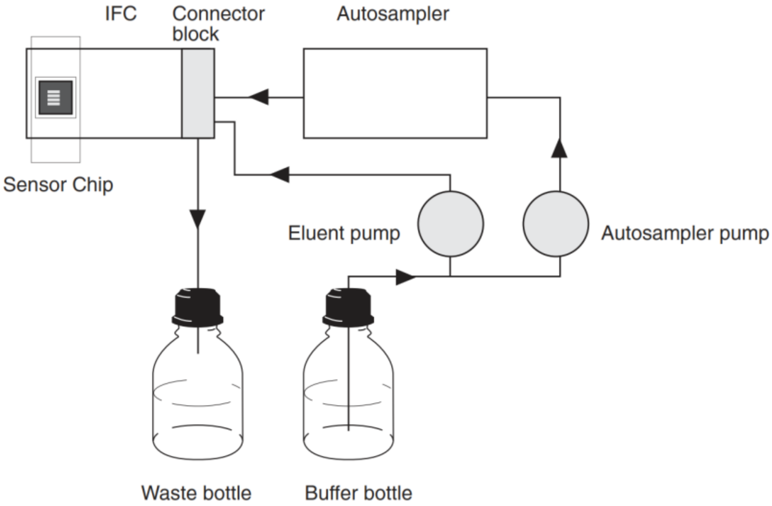

Figure 3.11 The liquid delivery system with two pumps and an autosampler transports liquid to the connector block where samples and buffers are injected to the IFC. The scheme adapted from ref. (GE Healthcare, 2008).

The Biacore 3000 system is used to implement the proposed SPR technique. One of the most widely used chips for various detections in microbiological fields is CM5. Its operating principle is based on SPR technique and is a good choice for the experiments in this study. The approach is capable of assessing the deviation of SPR angle following detection of anti-dengue virus immunoglobulin M antibodies (IgM) in human serum samples.

3.6.7 Measurement of the analysis cycle: scanning SPR microarray imaging of autoimmune diseases

3.6.7.1 Introduction

Almost every SPR-experiment applies the same basic procedure in which the first step, the so-called immobilization (stated in next section), involves covalent binding of a ligand to the surface of the sensor followed by the so-called analysis cycle. In order to detect the presence or a specific interaction of a certain analyte in a sample, prior to analysis, a capturing entity (the ligand) should be immobilized on the sensor surface. Although the ligand can be any type of (bio)molecule, more than 80% of the capturing agents used in SPR analysis are related to proteins (e.g. antibody, antigen, receptor, peptide). In the previous chapter, various chemical protocols are given for the attachment of ligands to the sensor surface. The current section covers the analysis cycle for measuring biomolecular interactions with SPR detection. After a discussion of the analysis cycle, it focuses on the use of SPR in immunoassays, for detecting anti-dengue virus from human serum. SPR imaging in combination with microarrays for diagnostic applications is rapidly evolving. To demonstrate the use of microarray-based biomolecular interactions, the analysis cycle of autoimmune dengue antibody interactions in serum monitored with SPR imaging is discussed.

3.6.7.2 Ligand immobilization

There are different ways for immobilization of substances onto the sensor surface. The choice of immobilization method depends on the properties of the substance. The immobilization approaches may be directed towards amine, carboxyl, thiol or hydroxyl groups on the ligand, or by using specific tags attached to the ligand. An amine coupling chemistry was used since it is the most widely applicable method to covalently attach biomolecules to the sensor chip surface and is suitable for the ligand. Using this method, the dextran matrix on the sensor chip surface is first activated with a mixture of 120 µl EDC and 120 µl NHS to give reactive succinimide esters. The ligand was then passed over the surface and the esters react spontaneously with amine groups to link the ligand covalently to the dextran.

The 6µl ligand (each serotype of dengue antigen) was diluted to 194ul acetate buffer. After the injection of ligand, ethanolamine was passed over the sensor surface to deactivate remaining active esters. The chip was then inserted into SPR apparatus to measure the SPR angle variations for each sample.

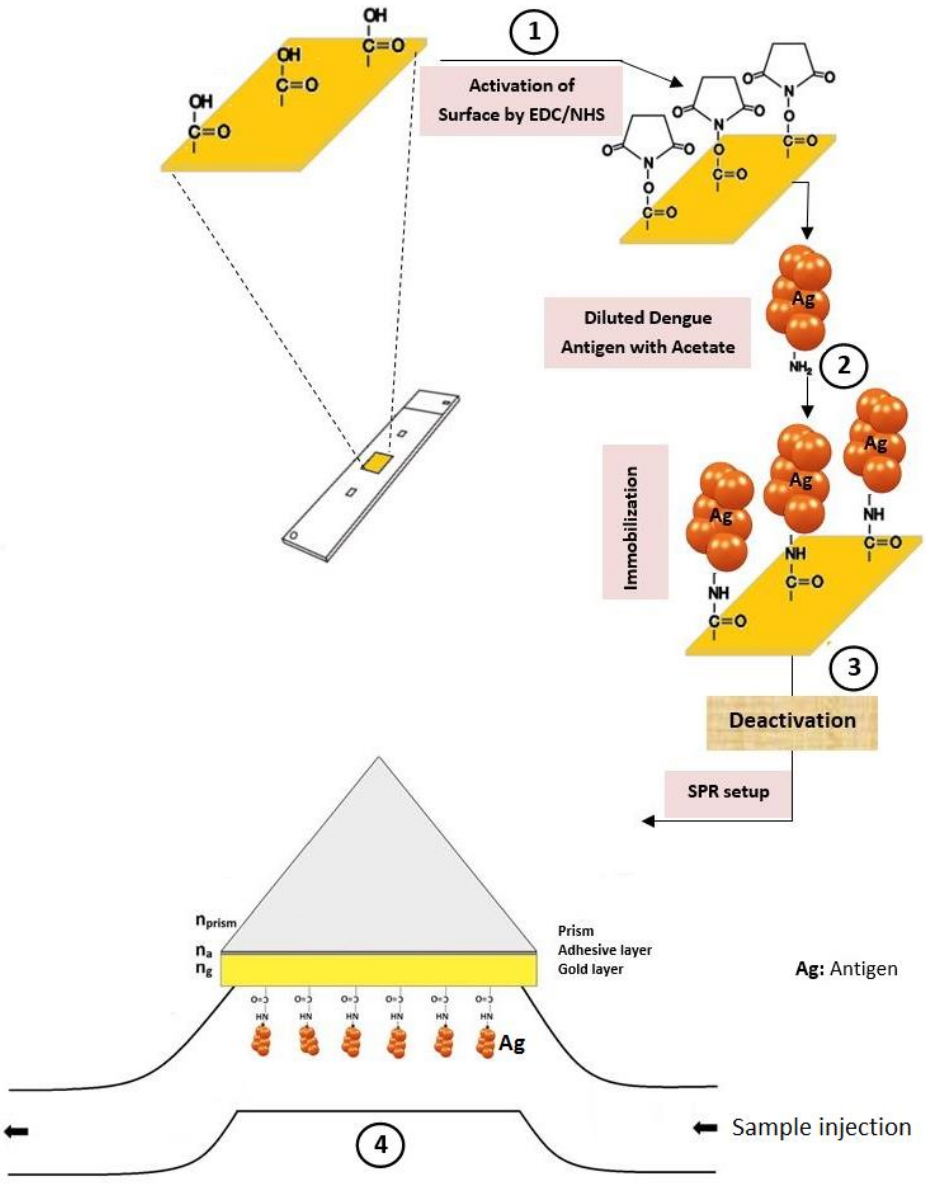

Figure 3.12 Schematic of the dengue virus diagnosis process-ligand immobilization part

The optimal level of immobilized ligand depends on the purpose of the analysis. In our case, the ligand was immobilized on the gold surface to act as a probe on the surface of the chip. The EDC/NHS was used for activation of sensor surface (see Figure 3.12, step 1). After surface activation, there is attraction and covalent coupling of the ligand, and then a buffer was used to wash away loosely associated ligand (Figure 3.12, step 2). The response level at this point provides the first indication of the immobilized amount. Deactivation and further washing away of loosely associated ligand were performed using ethanolamine (Figure 3.12, step 3). In addition, moderate flow rate (10μl/min) was utilized for immobilization.

In Figure 3.13, the immobilization sensorgram of the dengue antigen on sensor surface has been presented as an output of system.

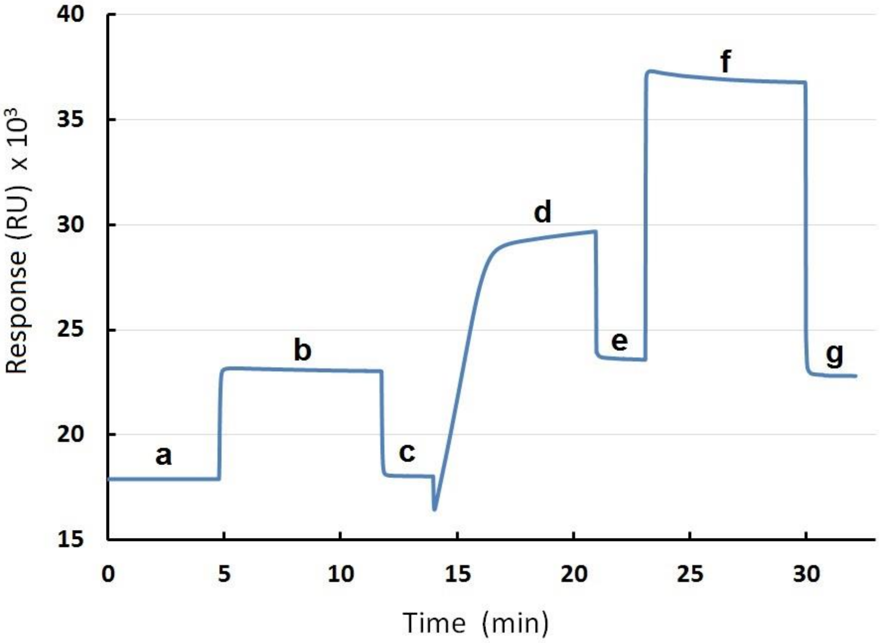

Figure 3.13 Immobilization sensorgram of the dengue antigen on sensor surface: (a) Baseline; (b) using EDC/NHS for surface activation; (c) baseline after activation; (d) attraction and covalent coupling of the ligand; (e) buffer washes away loosely associated ligand; (f) deactivation and further washing away loosely associated ligand; (g) the final response of immobilization.

3.6.7.3 The Analysis cycle for measuring biomolecular interactions

After immobilization of dengue antigen (as ligand), the analysis cycle starts with the introduction of a buffer solution in the measurement cell, in order to generate a (stable) baseline. Subsequently, a sample, containing the ligand's binding partner (the analyte), is introduced into the measurement cell and the analyte binds to the ligand, leading to the selective accumulation of the analyte on the sensor surface. This causes an increase in the refractive index near the sensor surface. This change in refractive index can be measured in real time. The selectively accumulated mass on the sensor chip surface (which is generally expressed in pg/mm^2) correlates linearly with the change in the refractive index near the sensor surface measured by the Biacore system.

3.6.8 The whole process of an assay

Based on the SPR technique, analyte (dengue antibodies which are in sample) is captured by the ligand (Figure 3.14). The ligand (dengue antigens) is permanently immobilized on the surface of sensor as explained previously.

The SPR device generates a sensorgram (RU via time) for each experiment, which measures the response in terms of resonance units (RU) and is proportional to the molecular mass on the surface. For an interactant of a given mass, the response is proportional to the number of molecules at the surface. A sensorgram gives a plot of response against time, showing the progress of the interaction and can be monitored in real-time throughout the analysis. The results from Biacore machine were then converted to show intensity via incident angle graph where 1000 RU is equivalent to 0.1 angle variations.

As shown in Figure 3.14 (step 4), the dengue antibodies bind to immobilized antigens on the gold surface. The binding interaction between the Ags and Abs was monitored by changing the SPR angle in real-time.

Biacore 3000 was used to investigate SPR angle changes to identify the existence of anti-Dengue virus IgM in samples. The Biacore data (Figure 3.14, step 5) was converted to the intensity via incident angle (Figure 3.14, step 6) using MATLAB programming to monitor the SPR angle variations. The sensor surface was regenerated at the end of each experiment to remove the bound analyte from the immobilized ligand on the surface (Figure 3.14, step 7).

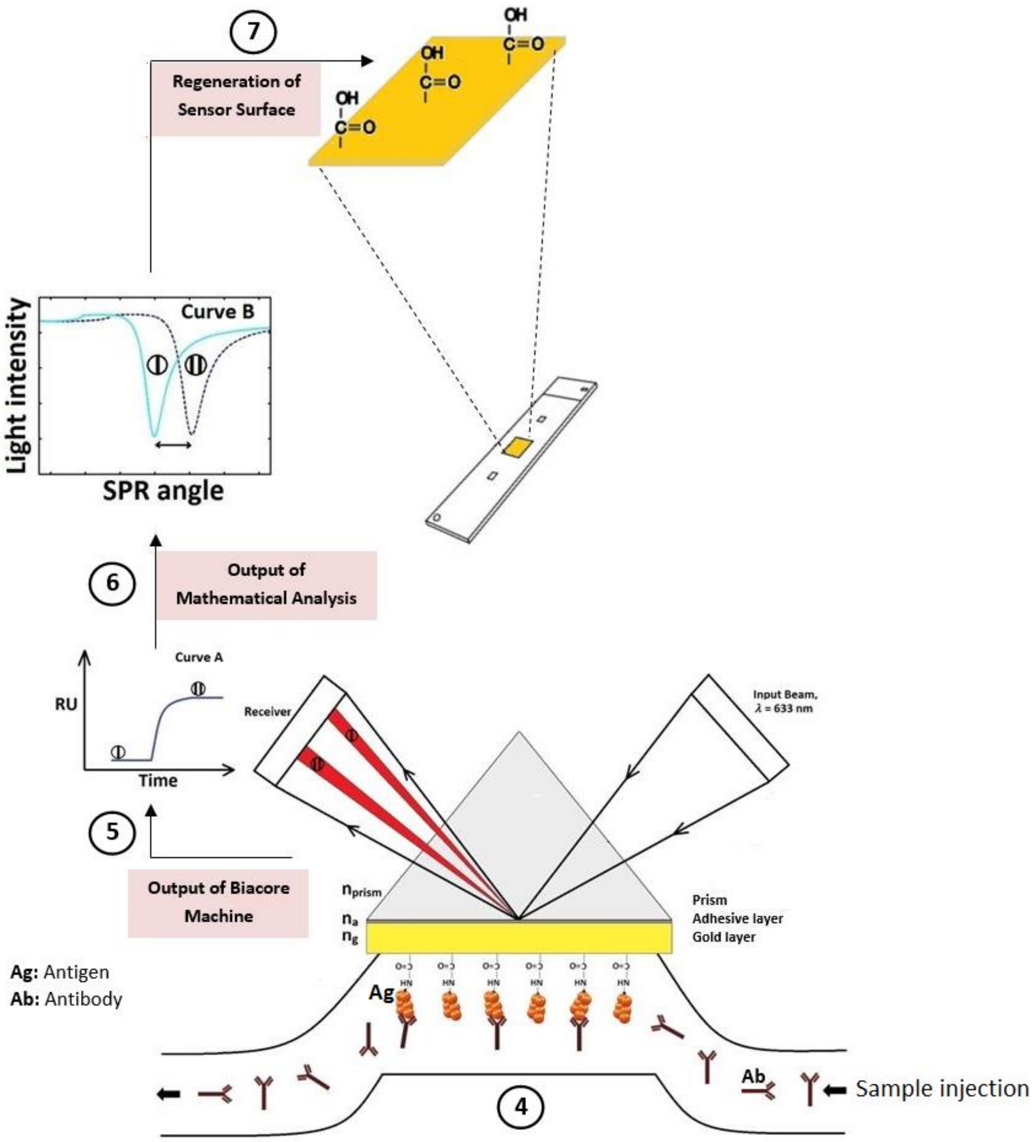

Figure 3.14 Schematic of the dengue virus diagnosis process-virus detection part

Figure 3.15 presents the measurement cycles of a sensor signal using direct-detection. Each measurement begins with conditioning the surface of sensor with an adequate buffer solution (Figure 3.15, part 1). It is of vital relevance to have a reliable baseline before the capturing event starts. At this point, the sensor surface contains the active ligands, ready to capture the target analytes. On injecting the solution containing the analytes (Figure 3.15, part 2), they are bound on the surface through its relevant immobilized ligands. Besides, other particles of the sample might stick to the surface of sensor which are not its relevant analyte of immobilized ligand, these binds will be non-specific, and accordingly broken easily in washing process. In this phase, adsorption kinetics of the analyte biomolecule can be specified in the real-time measurement. After this, the buffer is injected onto the sensor surface and the non-specifically bound particles are washed off (Figure 3.15, part 3; dissociation process). As shown in the figure, the accumulated mass is obtained from the output of SPR sensor. The ΔR presents the measured response that is due to the bound analyte onto the sensor surface. At the end, the regeneration solution (glycine buffer) is injected that breaks the ligand-analyte binding on the surface (Figure 3.15, part 4). It is obvious in order to carry out the multiple assays with a same biosensor, the glycine buffer should be used to leave the intact ligands activity during each analysis cycle. In this case, as shown in Figure 3.15, there are two times regenerations. The bulk shift of refractive index can be found out at t_1. Again, the buffer is injected to have a same condition onto the surface for the next analysis cycle. It should mention, remaining accumulated particles (either the bound analytes to ligands or non-specific bindings) causes to increase the baseline level if the regeneration phase does not do properly.

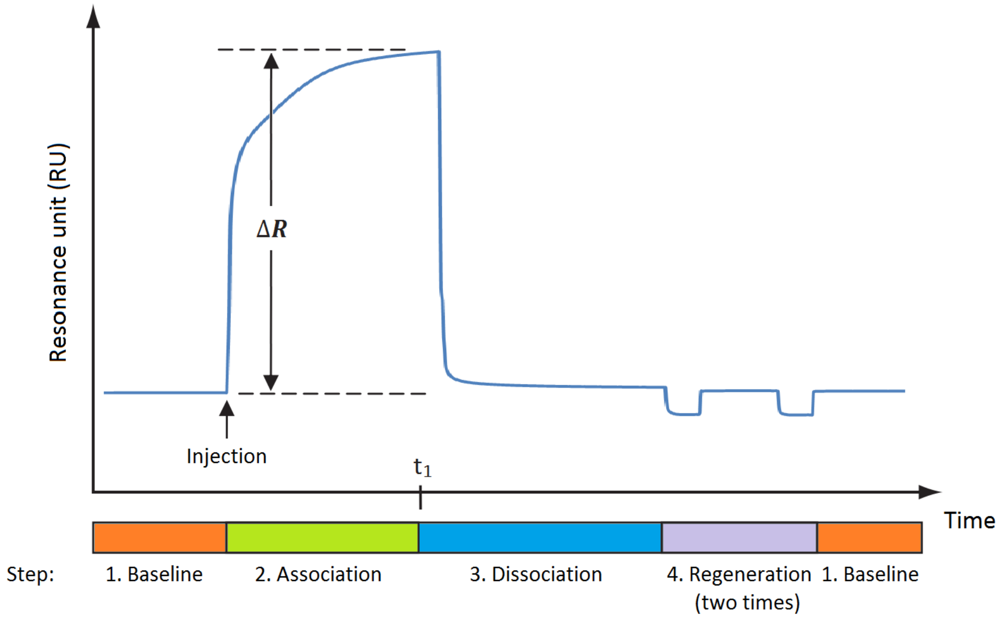

Figure 3.15 A sensorgram which is shown the all phases of an analysis cycle

In Figure 3.16, the data management of each assay is presented schematically from the Biacore machine till obtaining an intensity versus incident angle graph.

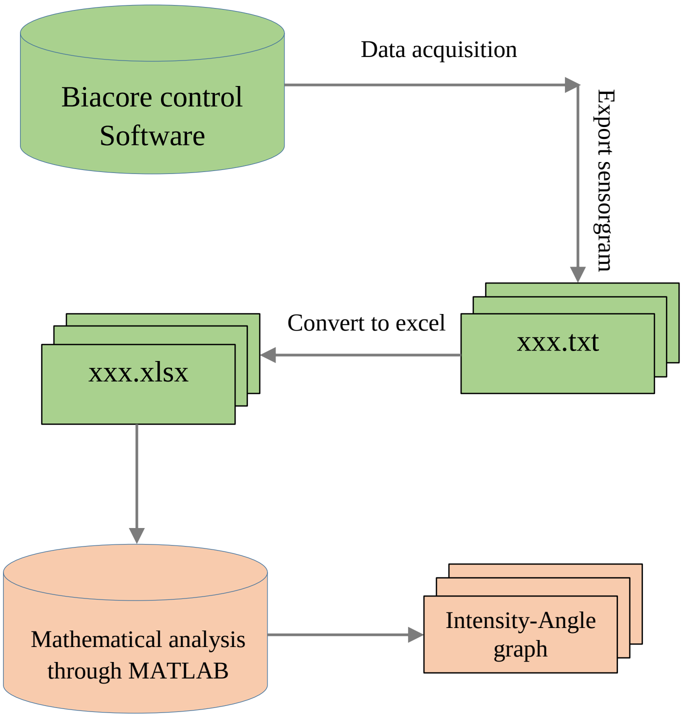

Figure 3.16 Schematic of data management of each assay

3.6.9 Sample Collection

Blood samples which is used in this study were collected from University Malaya Medical Centre, Hospital Ampang and Hospital Tengku Ampuan Rahimah (Klang). The approval of this study protocols was accepted by the institutional review board of the University of Malaya Medical Centre (Ethics no. 782.90) and from both Klang and Ampang Hospital (Ethics no. NMRR-10-683-6420). Written informed consent from patients and asymptomatic donors were obtained prior to blood collection, and the study was conducted in accordance with the “Declaration of Helsinki”.

3.6.10 Investigation of sample concentration - calibration curve

The basic understanding of the SPR signal and the measurement procedure were discussed in the previous section. According to the POC tests, the sample volume and biochip surface regeneration are two significant issues which have effect on the quality and accuracy of microbiological laboratory results. In the following, we are going to discuss on the sample concentration with chip regeneration.

In this experiment, the different concentrations of sample are studied to determine the most appropriate concentration to obtain highest sensing and better surface regeneration. Evaluating the kinetic and equilibrium situations' concentration dependence leads to sample volume optimization under this study's particular conditions. This experiment is repeated under the same conditions, whereby all environmental variables (e.g. temperature and buffers) are fixed to examine the sample concentration. The serum is diluted (by adding solvent 10 mM sodium acetate with pH 4.5) to concentrations of 1:25, 1:50, 1:100, 1:200, 1:400 and 1:800 by adding 10mM sodium acetate solvent with pH 4.5. The experiment is carried using these six different concentrations. According to the flow chart in Figure 3.17, we have already immobilized the serotype 2 of dengue virus (the ligand) on sensor surface and specified patient's serum as an analyte in different concentrations.

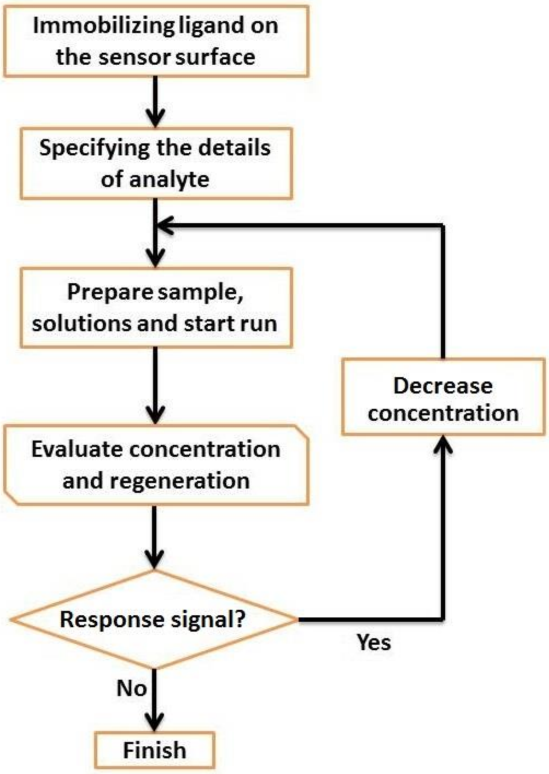

Figure 3.17 Flow chart of the test concentration and regeneration of biosensor.

3.6.11 Clinical samples

The clinical samples were provided by University of Malaya Medical Center (UMMC). The distinction of dengue specific IgM from cross-reactive IgM and the IgM reactions against the infection of serotypes, which are higher than other serotypes of most major dengue virus infection, are the primary causes of using dengue specific IgM antibody as a target for detection.

According to Figure 3.18, the samples include:

- Highly positive (antibody titre 1280-10240 or more),
- Mid positive (antibody titre 160-640), and
- Low positive (antibody titre 10-160),

which were classified via hemagglutination inhibition (HI) antibody and ELISA tests (Organization & others, 2011; Peeling et al., 2010).

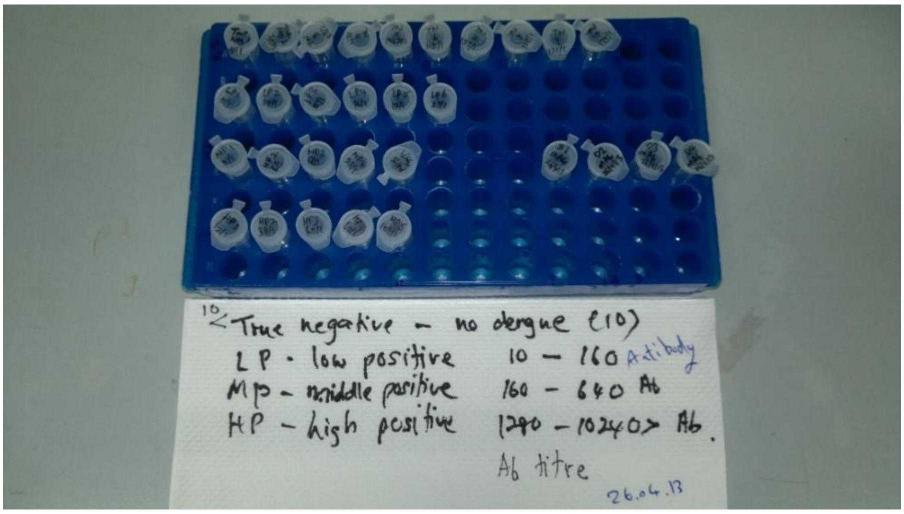

Figure 3.18 The samples from four different serotypes of dengue virus which have been categorized to the three groups

Furthermore, some samples with

- tick-borne encephalitis (TBE) virus,
- and hepatitis C (HC) virus,

were provided in conjunction with the specificity investigation as shown in Figure 3.19. The samples were tested with the SPR method to ensure high sensitivity and specificity.

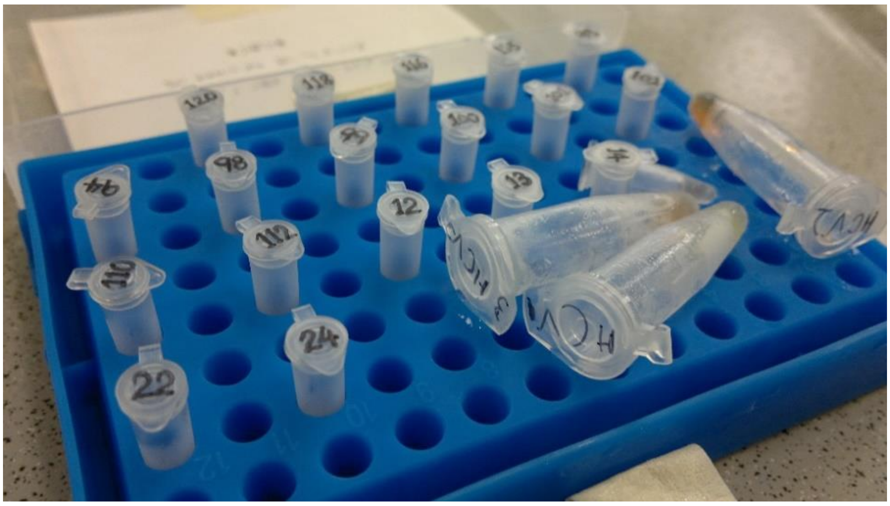

Figure 3.19 Some samples with tick-borne encephalitis (TBE) and hepatitis C (HC) antibodies

4 CHAPTER IV: RESULTS AND DISCUSSIONS

4.1 Introduction

According to our studies in chapter 3, there are a variety of results including the simulation and experimental works. The first section presents the mode analysis of general SPR configuration along with the propagation analysis in symmetric mode. In the following different optical properties models are compared in order to choose the most appropriate model for analyzing the proposed SPR structure analytically and numerically.

The sensor signal of immobilization process is shown for all four types of dengue virus. This sensor signal can validate the immobilization process. Furthermore, the immobilized particles on the chip surface can be observed by microscopic images. The determination of appropriate levels of sample concentration is a prior to examination of all samples in our study. All samples are examined and subsequently the SPR angle variation is obtained for each sample in order to determine the ratio of all dengue serotypes. The sensitivity and specificity are inferred through these experimental results. At the end, according to the samples serotype 2 which contain low, mid, and high positive dengue viruses, the calculated SPR angle variations are investigated and then validated through the obtained experimental SPR angle variations.

4.2 Mode and propagation analysis of general SPR configuration

In this section, the proposed SPR structure is simulated for its capability in supporting surface plasmon wave in mode and propagation analysis of symmetric SPPs.

4.2.1 Mode analysis of symmetric SPPs

Mode analysis of cross section shows the possibility of only one surface plasmon mode being supported with an effective index near to the dielectric material refractive index (Figure 4.1).

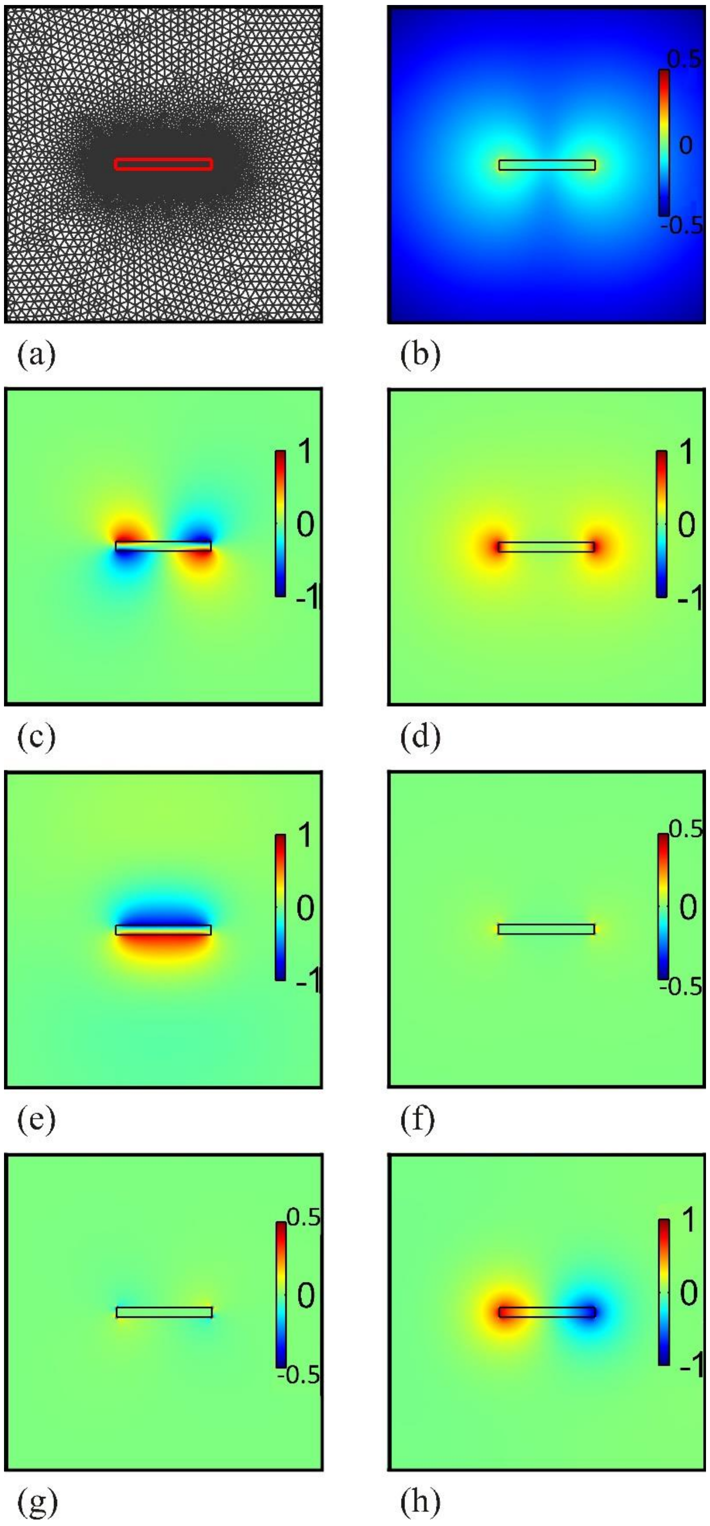

Figure 4.1 Mode analysis of the proposed structure. (a) Mesh structure near and within the metal strip. (b) Total energy density time average. (c-h) fields distributions: H_x, H_y, H_z, E_x, E_y, and E_z respectively

4.2.2 Propagation analysis of symmetric SPPs

Following the successful mode analysis of the structure as shown in Figure 4.1, the three dimensional configuration of the proposed model was designed to present the propagation of surface plasmon wave. The 3D structure consists of the same metal film with length of 2µm as shown in Figure 3.4.

The boundaries were modeled using scattering boundary condition. The *x* and *y* components of magnetic field are used to excite the wave at the input facet. A careful meshing procedure is followed to produce a smooth result. The mesh and results are illustrated in Figure 4.2 which shows the propagation of light along the metal strip in terms of its electric and magnetic fields. As depicted by the figures, the power of light is carried by the same surface plasmon mode that was obtained in mode analysis of the cross section. It is inferred from the results that the main and the only mode for transporting the power of light along the propagation axis, is the surface plasmon mode obtained in the mode analysis.

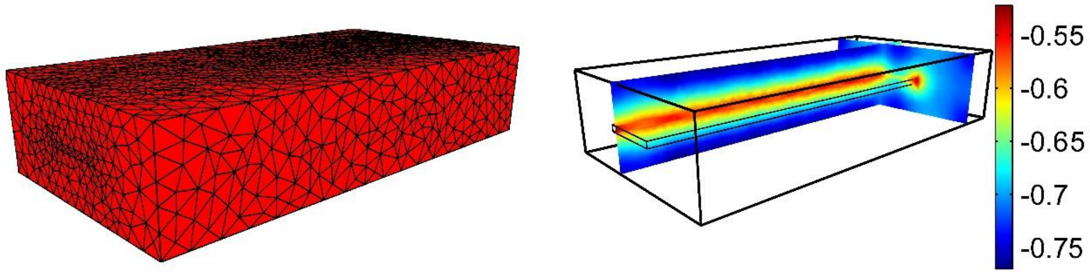
(a) Mesh structure

(b) Energy density time average

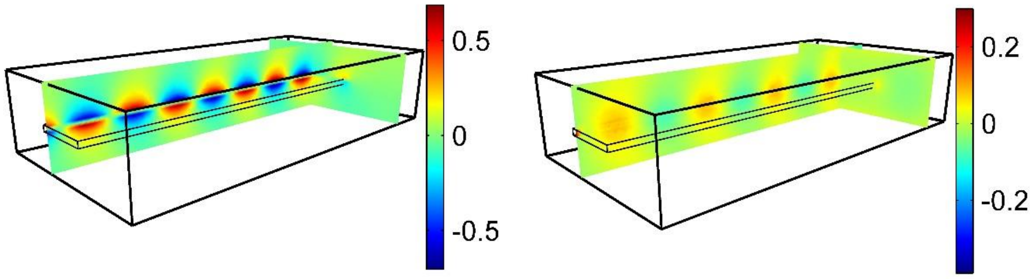
(c) Re{ Magnetic field, H_x }

(d) Re{ Magnetic field, H_y }

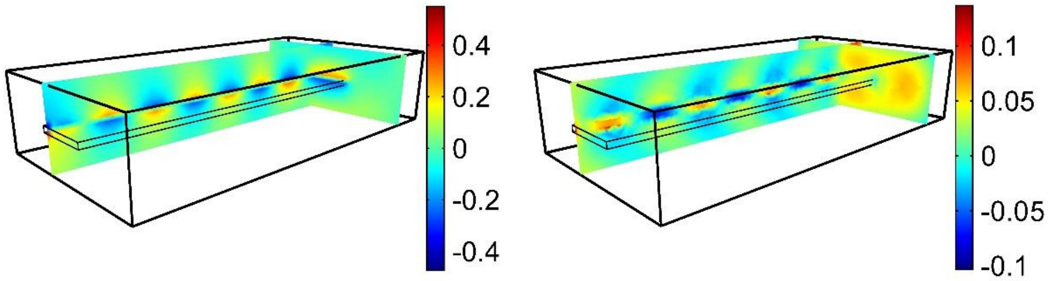
(e) Re{ Magnetic field, H_z }

(f) Re{ Electric field, E_x }

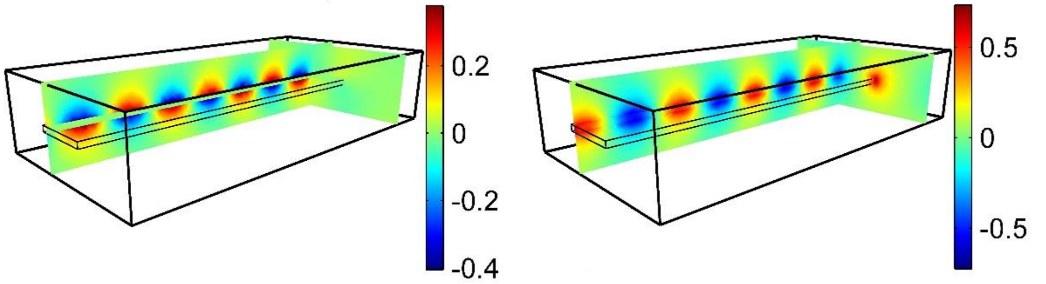
(g) Re{ Electric field, E_y }

(h) Re{ Electric field, E_z }

Figure 4.2 Three dimensional simulation of the proposed model. (a) Mesh structure. (b) Energy density time average distribution of the light. (c-h) Field distributions.

4.3 Numerical analysis for surface binding affinity

The SPR biosensor and its behavior are simulated by a numerical approach using finite element method. The magnetic field in the *z* direction of plasmons on the gold film is simulated in Figure 4.3. An increase in the *z* component of magnetic field (generated resonance on the gold surface) is observed when the refractive index of patient sample is increased.

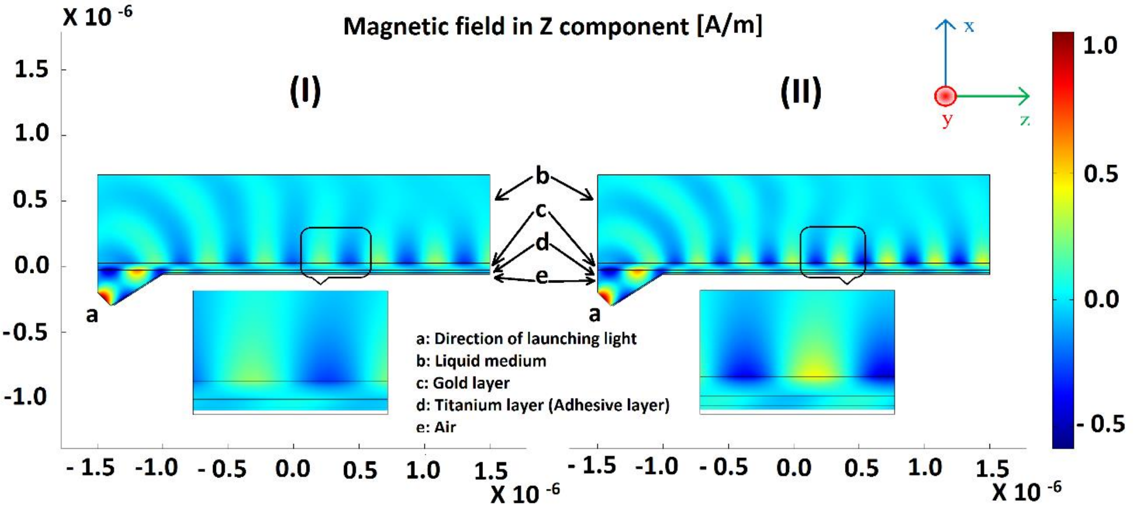

Figure 4.3 The presence of magnetic field in *z* component by numerical modeling of biosensor structure, (I) is with sample's refractive index of 1.33 and (II) is with sample's refractive index of 1.34

This increase is shown in Figure 4.4 at a plot clearly. This small change that is due to the delicate sensitivity of SPR biosensor, shows the quantity of bound antibodies with the immobilized dengue antigens. The increasing of quantity raises the refractive index of binding medium which are plotted the magnetic field at the minimum as initial buffer (1.33) and maximum as a high positive dengue serum (1.34). According to the quantity of bound Ag-Ab onto the sensor surface, the magnetic field varies between the two curves.

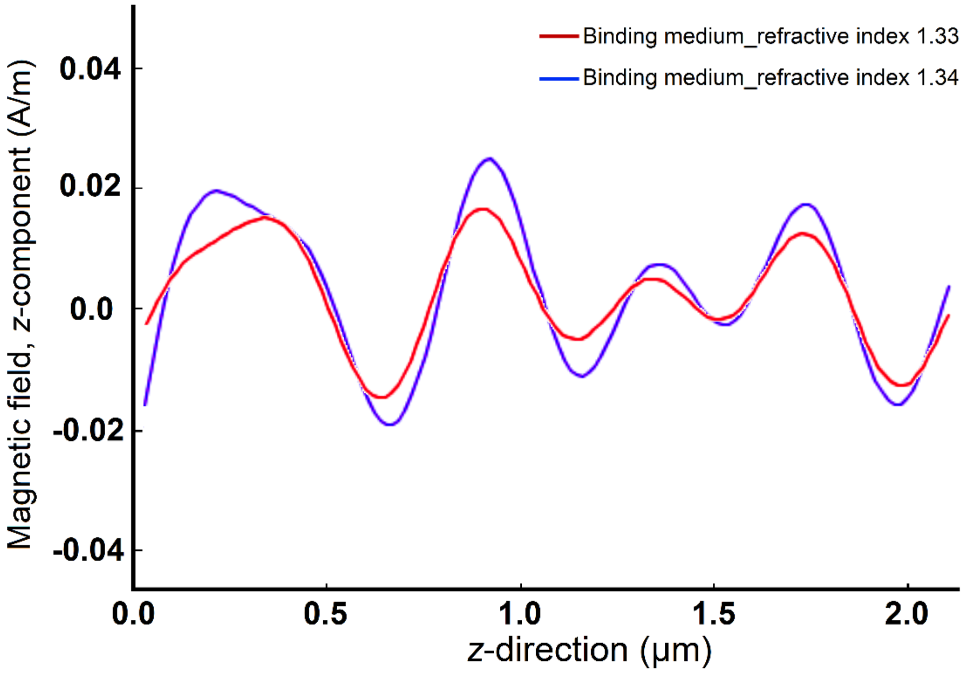

Figure 4.4 Numerical analysis of biosensor structure with refractive index 1.33 to 1.34

4.4 Investigation of optical properties models on SPR structure

The common optical properties models are compared in the real and imaginary parts of the permittivity with an experimental data and then the best model (based on the desired range of wavelength) is applied to study the proposed SPR structure analytically and numerically.

Here, MATLAB programming is used for mathematical analysis of SPR method to investigate the reflectance against incident angle and SPR angle against wavelength. The numerical part is an application for the chosen model which is simulated by COMSOL Multiphysics.

4.4.1 Comparison between common optical properties models for metallic thin films

Following the decision to use gold as the metal thin film discussed, the permittivity of the gold is computed at different wavelengths. For every model the real and imaginary parts of permittivity are calculated in the separate process and compared each part from the different models. Through an overlay plot depicted in Figure 4.5, the real part of permittivity versus wavelength of experimental data, and Multi Oscillator, Drude-

Lorentz, Brendel-Bormann, Drude models are demonstrated. The error analysis with respect to experimental data was also done (Figure 4.6).The similar overlay plot was provided for the imaginary part of every model as shown in the Figure 4.7. In Figure 4.5 and Figure 4.7, the red dotted line represents the experimental values. The yellow, blue, green and purple lines are representative of the Drude, Lorentz-Drude, Brendel-Bormann and Multiple Oscillator Models respectively. It is obvious that the Drude model has the least agreement with the red dotted line and it is confirmed by the error value of Drude model in the Figure 4.6. In this figure the percentage of the deviation of models' real value and experimental data is calculated. Despite the Drude model, the other models have less deviation from the experimental data in the real part of permittivity. However, even the response of the Drude model for wavelengths more than 700nm is acceptable. In general, most of these models can be used to obtain the real part of the permittivity.

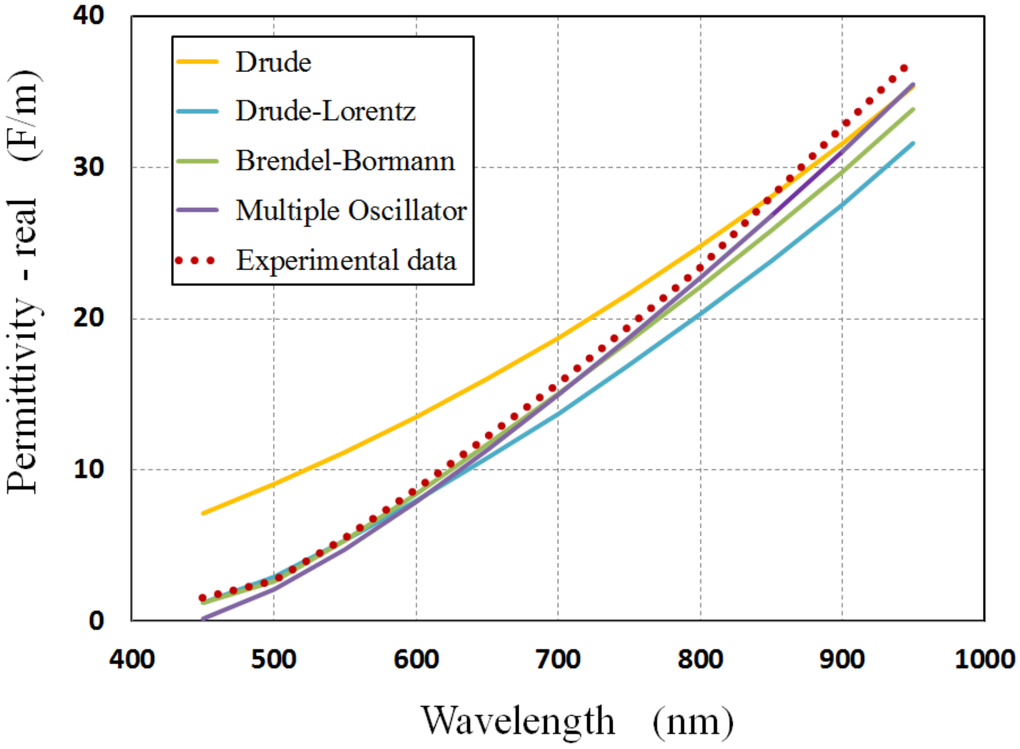

Figure 4.5 Real part of permittivity (F/m) against wavelength (nm) of experimental data, and Multi Oscillator, Drude-Lorentz, Brendel-Bormann, Drude models

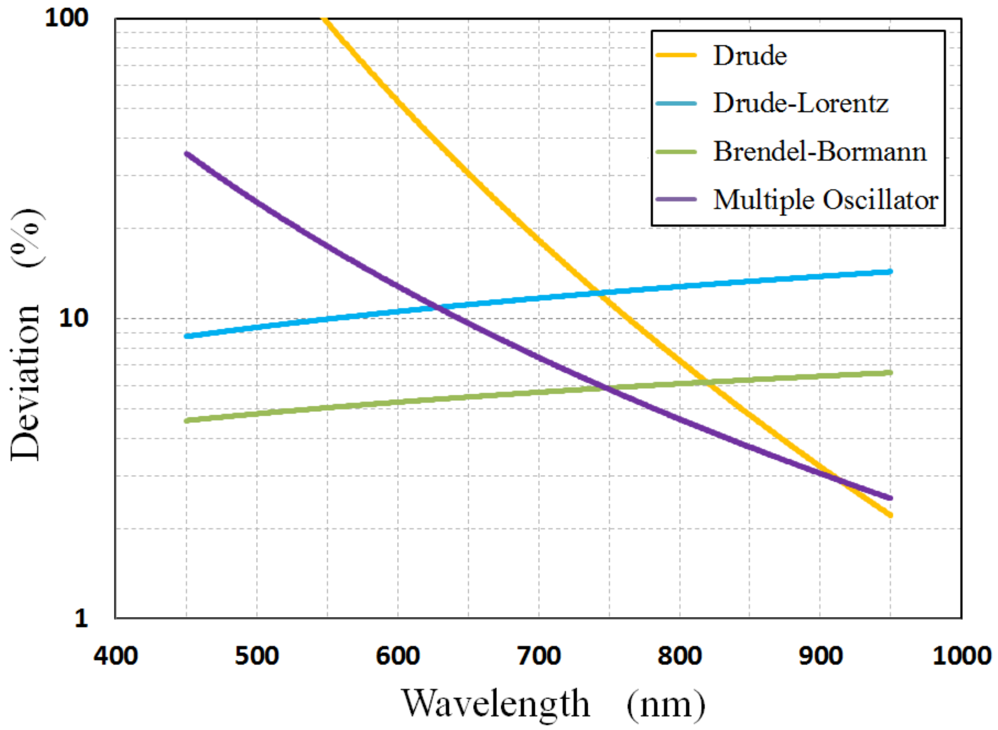

Figure 4.6 Error value at real permittivity (%) against wavelength (nm)

The same comparison has been done for the imaginary part of the permittivity. The results of this computation are shown in Figure 4.7 and the percentage of the deviation of the models' imaginary values are shown in Figure 4.8. This time the aberration of Drude model is more obvious and it can be observed from Figure 4.8 as well. It is clear that we cannot use this model to predict the imaginary part of permittivity. Also the D-L model has a notable aberration and its difference can be traced on the blue line in the Figure 4.8. However, the B-B and M-O models (green and purple lines) still have an interesting harmony with the experimental data in both real and imaginary parts of the permittivity and it can be determined via error plots (Figure 4.6 and Figure 4.8).

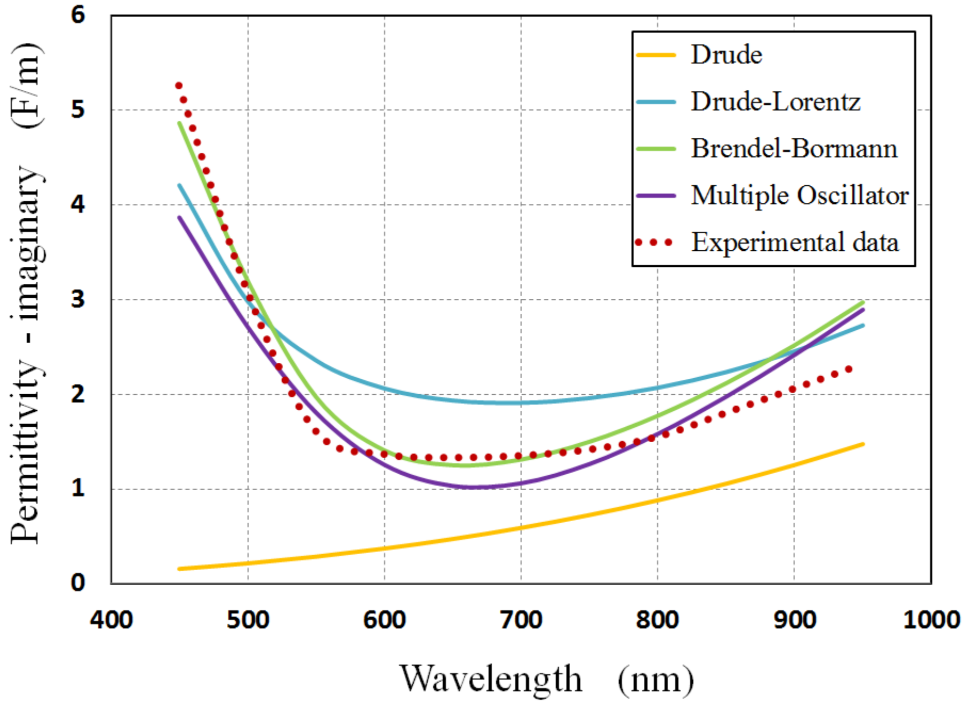

Figure 4.7 Imaginary part of permittivity (F/m) against wavelength (nm) of Experimental Data, and Multi Oscillator, Drude-Lorentz, Brendel-Bormann, Drude models

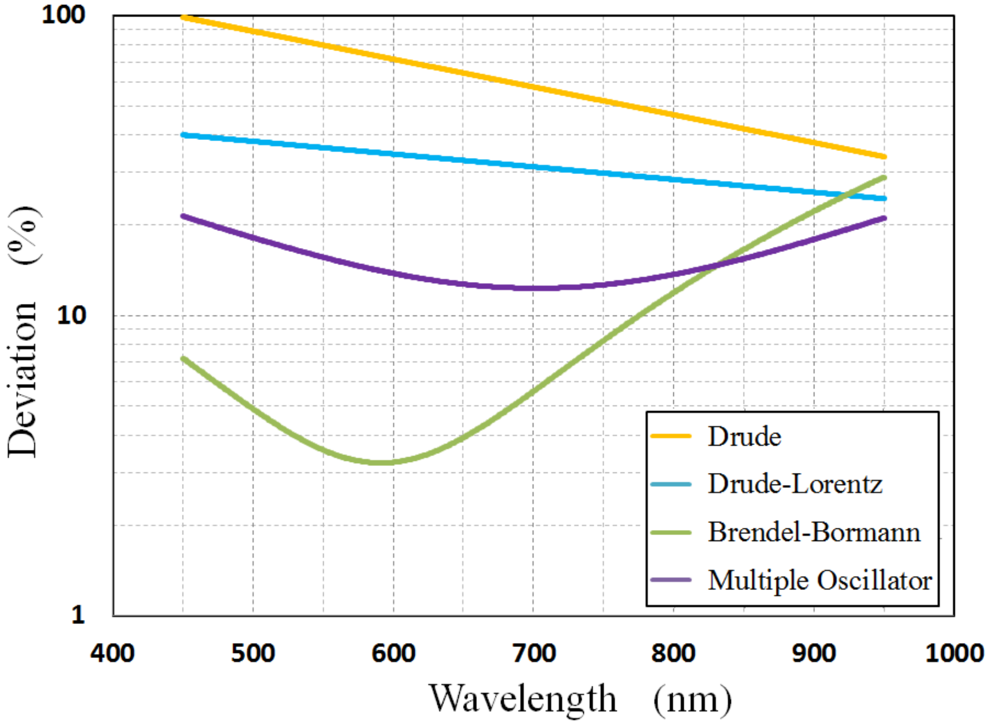

Figure 4.8 Error value at imaginary permittivity against wavelength

Although, the B-B and M-O models have closest results to the experimental data; however, it is needed for further investigation to determine most proper model between them. Hence, the proposed SPR structure is utilized to obtain more precise results for these two models. The results of each model are applied in this structure to make an analytical and numerical analysis. In the next two sections we discuss the general results of using these models in the proposed SPR structure to reach an overall decision about accuracy of these models.

4.4.2 Analytical analysis of the models on SPR structure

In the previous section we showed that the Drude and D-L model have less accuracy in comparison with the other two models. However, more analysis is needed to make sure which model technically works better.

The SPR angle is an incident angle that the entire beam is absorbed by the layers to make a maximum resonance and as a result there will be no reflection from the structure. The optical properties of different layers in the SPR structure can affect this special angle. On the other hand, any perturbation on the surface of this structure can shift the SPR angle which is the basics of the sensing. It is very important to estimate the most accurate SPR angle that is shown in the Figure 4.9 using different models. The dips in this plot indicate the lowest reflectance in the SPR angle. Each curve belongs to an optical model that was applied to calculate the permittivity of metallic layers in the wavelength of 600nm. As it can be concluded from Figure 4.9, B-B model is perfectly matched with experimental curve, so it is the best choice to be used in the proposed SPR model.

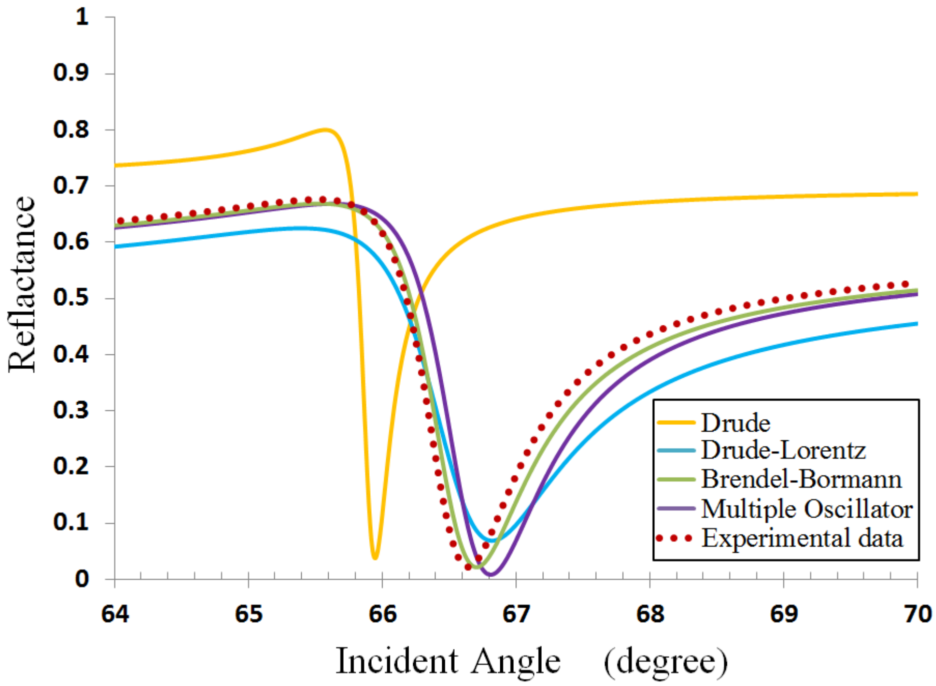

Figure 4.9 Reflectance against incident angle of 30 to 70 degree, at 600nm

After finding the SPR angle for a specific wavelength, we extended the study to include different wavelengths. In Figure 4.10 the SPR angle is calculated with respect to the permittivity of gold and titanium film which directly depends on the wavelength. As such, for each wavelength value, the optical properties of the thin films will also change and this in turn will change the SPR angle. Again the red (dotted) curve is representative of experimental data and SPR angle calculated based on the Brendel-Bormann model has the best agreement with it. This can be concluded by the deviation calculation of results of different models in Figure 4.11. The reason for the small differences in this case is that even a very small variation in the angle, can affect the calibration of the SPR setup. In fact the deviation cannot be high and as it is clarified in the Figure 4.11, the deviation from the experimental case is mostly less than 1%; however, it can be seen that the deviation of B-B is less than 0.1% along the whole examined spectrum which is very important in achieving the reliable results.

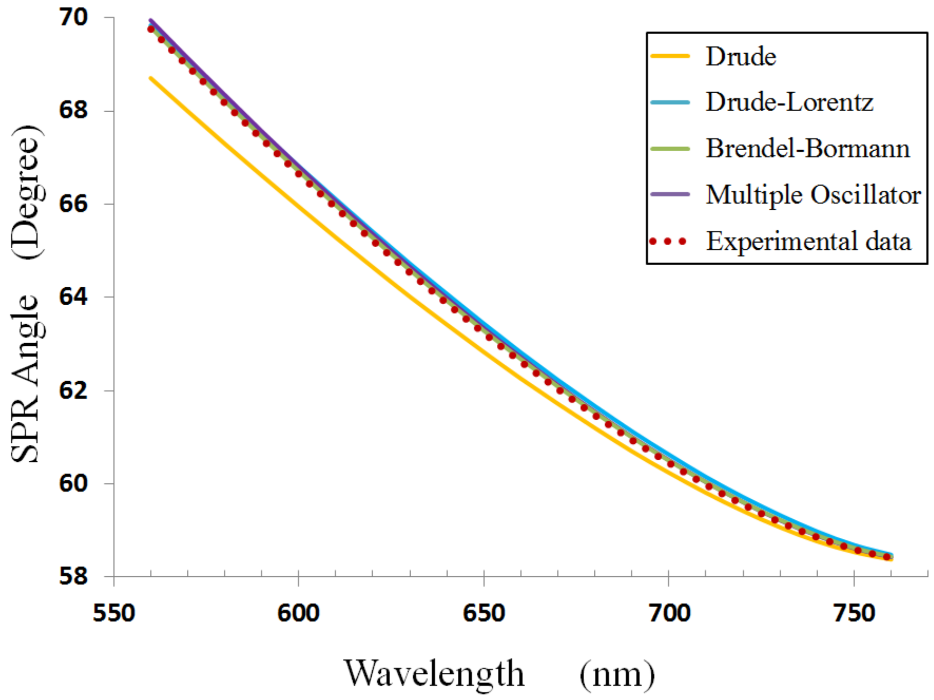

Figure 4.10 SPR angle (degree) against wavelength of 560nm to 760nm

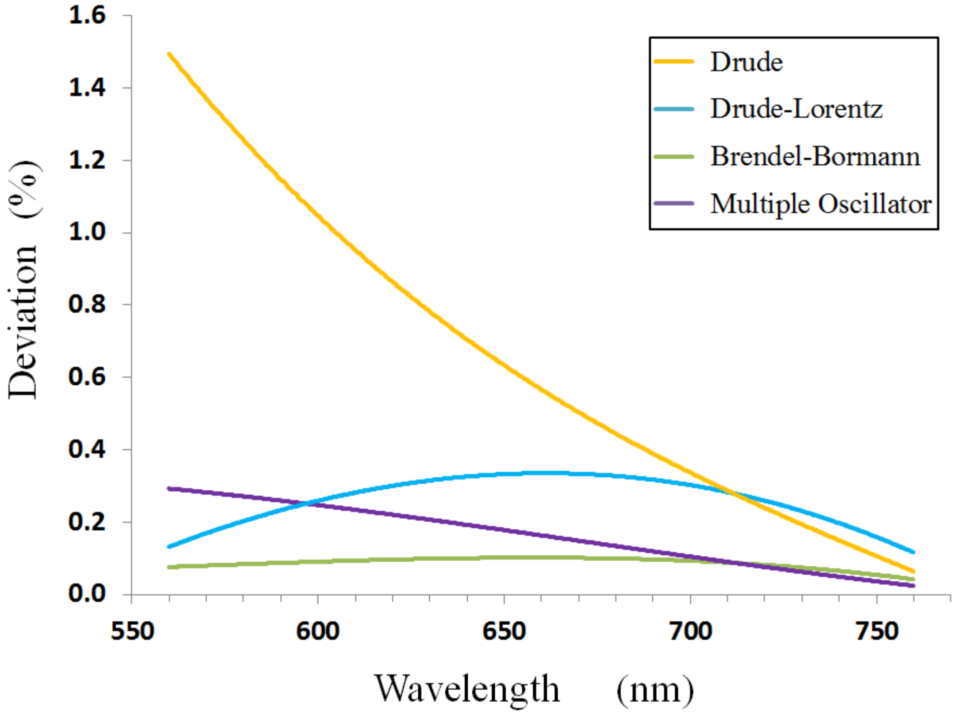

Figure 4.11 Error value at SPR angle for wavelength of 560nm to 760nm

4.4.3 Numerical analysis of the models on SPR structure

As indicated by analytical results, the B-B model is the best outfit for our proposed SPR model. Therefore, this model is utilized to numerically analyze the proposed SPR structure. An application to show the response of the proposed model in a simple surface plasmon structure is finding the power-flow in the cross-section of different layers. The power-flow (also known as load-flow) is an important tool involving numerical analysis that can be applied to a system. It is a factor related to propagation of the medium and for surface analysis it can give us a good perspective for surface sensitivity.

Figure 4.12 shows the power flow of the SPR structure which is plotted versus time average. In this figure the horizontal axis is shown the length of layer in the cross-section of SPR structure. As it is obvious in this picture, the gradual increase in the power-flow results in a sudden drop when passing from dielectric to metal (titanium on the left and gold on the right side) while a small spike can be recognizing in the titanium and gold boundary. It means that the surface is more sensitive when there is a dielectric-metal boundary than metal-metal boundary. Also as much as the increase of the power flow at near of the metal surface is sharper, the sensation is more related to that surface and if it was broad, it can be interpreted as having a good spatial sensitivity. In the case as it is clear the increase of the continuum is sharp and especially near the gold wall the sensitivity is too high. Through Figure 4.12, we can observe that the simulated power-flow using B-B model to calculate the optical properties of the layers (green curve at the background) is well coincided with the simulated power-flow using experimental optical properties (red dotted line).

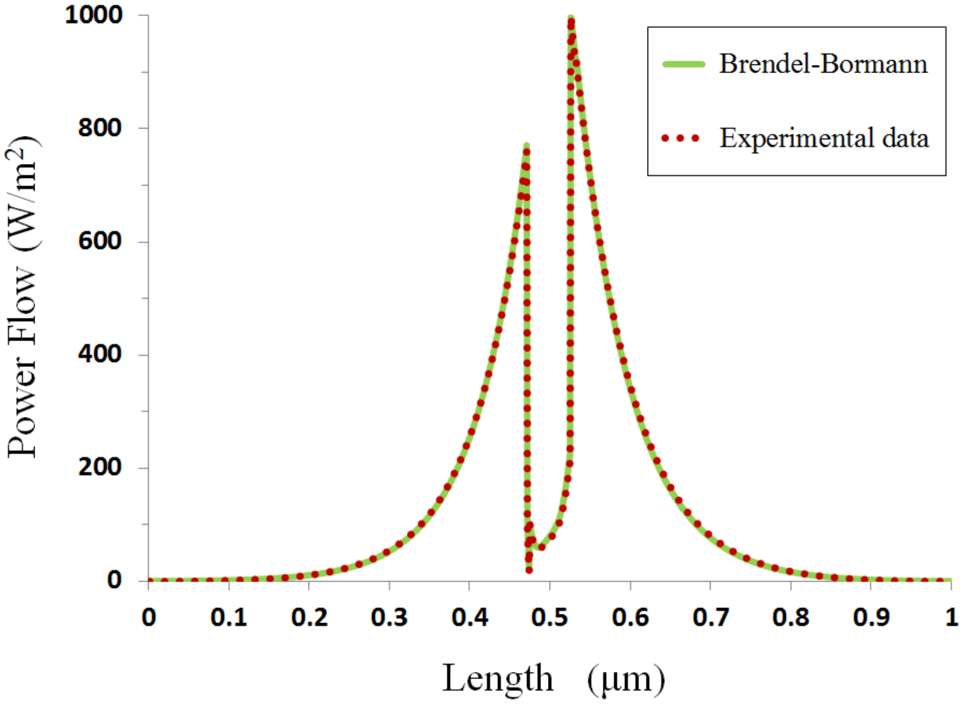

Figure 4.12 Comparison between using experimental data and Brendel-Bormann model at energy density time average distribution of the light

4.5 Sensor signal of immobilization process

Figure 4.13Figure 4.13 shows the immobilization process of four serotypes of dengue virus which has seven steps (step (a) to (g)). At the first, the sensor signal was located on the baseline (Figure 4.13_step (a)). The EDC/NHS was utilized to activate the sensor surface (Figure 4.13_step (b)), and then returns to the baseline again (Figure 4.13_step (c)). In the following there was attraction and covalent coupling of the ligand (Figure 4.13_step (d)). Next, a buffer washed away loosely associated ligands (Figure 4.13_step (e)). The response level at this point provided the first indication of the number of immobilized ligands. Deactivation and further washing away of loosely associated ligands were performed with ethanolamine (Figure 4.13_step (f)). The final response of immobilization was recorded at the end (Figure 4.13_step (g)). In addition, a moderate flow rate of 10μl/min was used for immobilization.

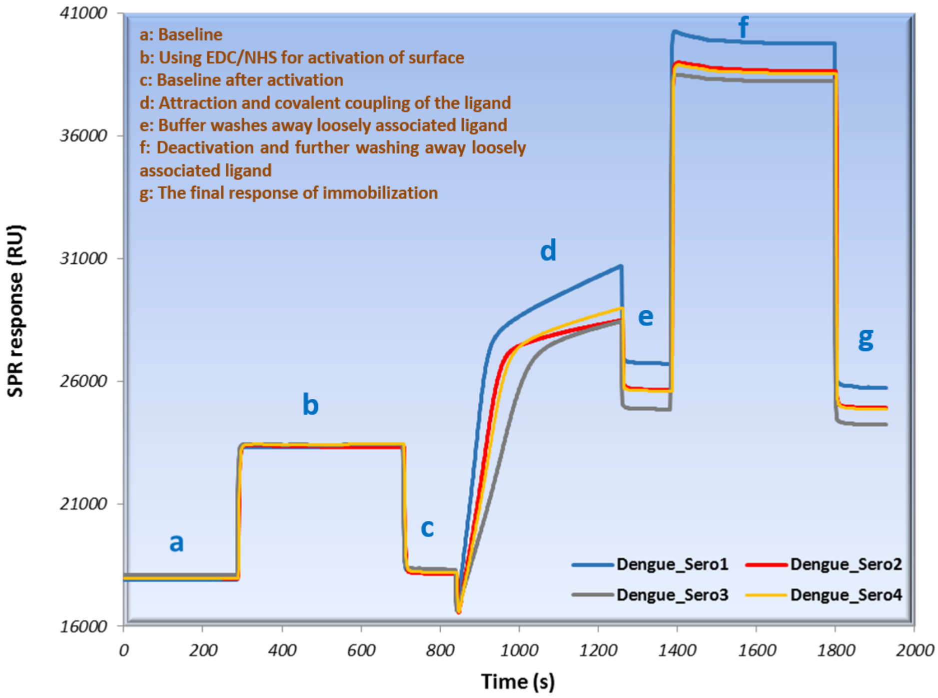

Figure 4.13 Immobilization sensorgram of four serotypes of dengue antigen on sensor surface

4.6 Microscopic information of chip sensor

The SEM and AFM images support the virus immobilization has been done properly in the following.

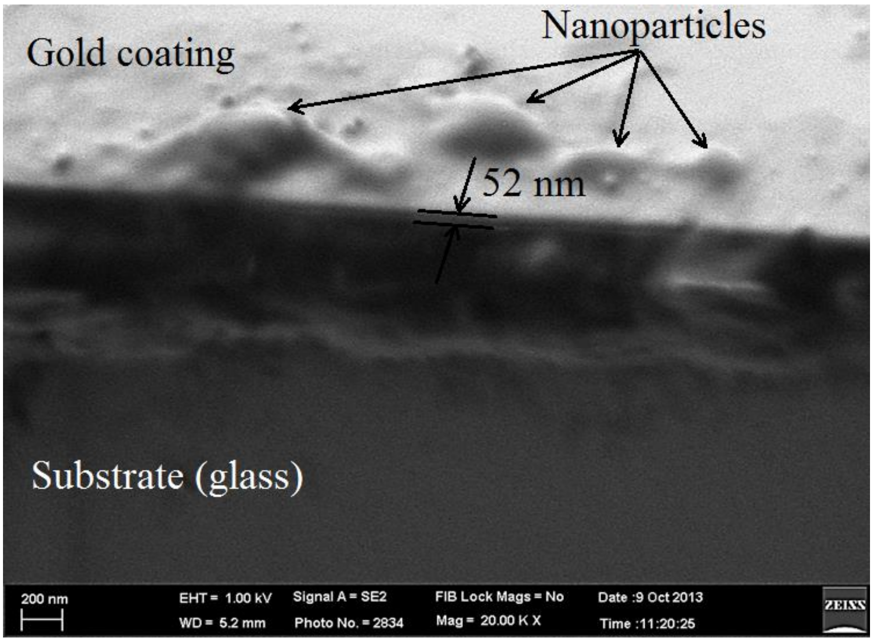

Figure 4.14 Imaging of the immobilization process on the gold surface using SEM

The surface on which the antigens (Ag) were immobilized was characterized using scanning electron microscopy (FE/SEM Quanta FEG250) and atomic force microscopy (VEECO DIMENSION 3000 AFM). AFM imaging was performed in contact mode using 0.01-0.025 Ohm-cm antimony (n)-doped silicon probes. Figure 4.14 exemplifies a typical cross-sectional view of gold coating on glass accompanied by nanoparticles such as amine groups and immobilized antigens. According to the SEM, the gold coating was around 52nm thick.

Figure 4.15 displays the top view of the gold surface with immobilized antigens on it. For further investigation 2D and 3D images of AFM were employed to prove the existence of immobilized antigens (Figure 4.16 and Figure 4.17). The 3D AFM image shows the surface of the gold-coated glass with two distinctive types of hills: first, homogenous, dense and low gold hills resulting from amine groups and second, sporadic higher hills created by immobilized antigens. The amine groups acted as a binding protein to the sensing antigen, which anchored very well to the sensor surface.

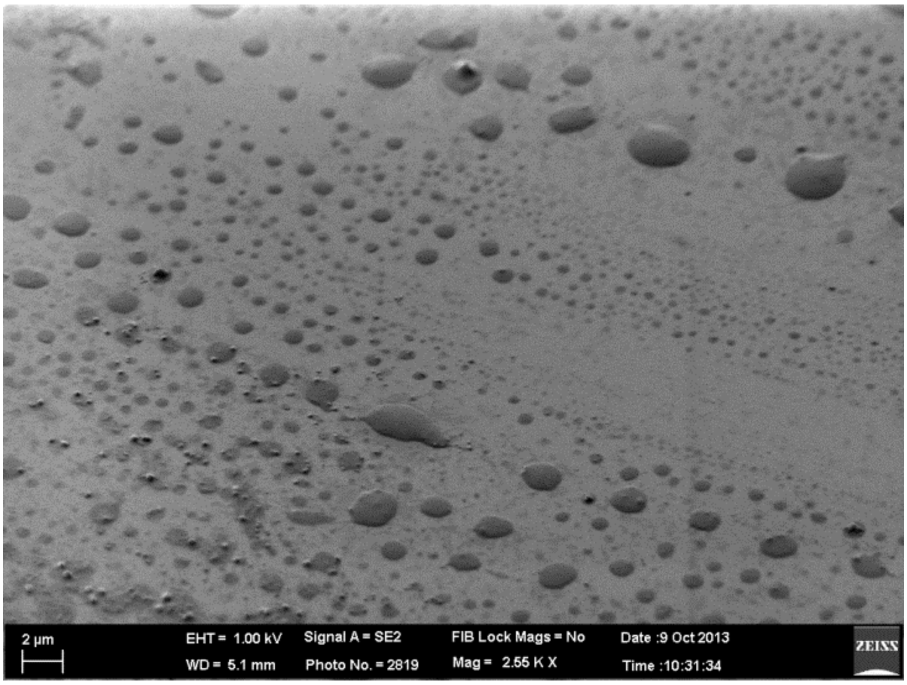

Figure 4.15 Imaging of the immobilization process on the gold surface using SEM machine- SEM top view of immobilized antigen surface

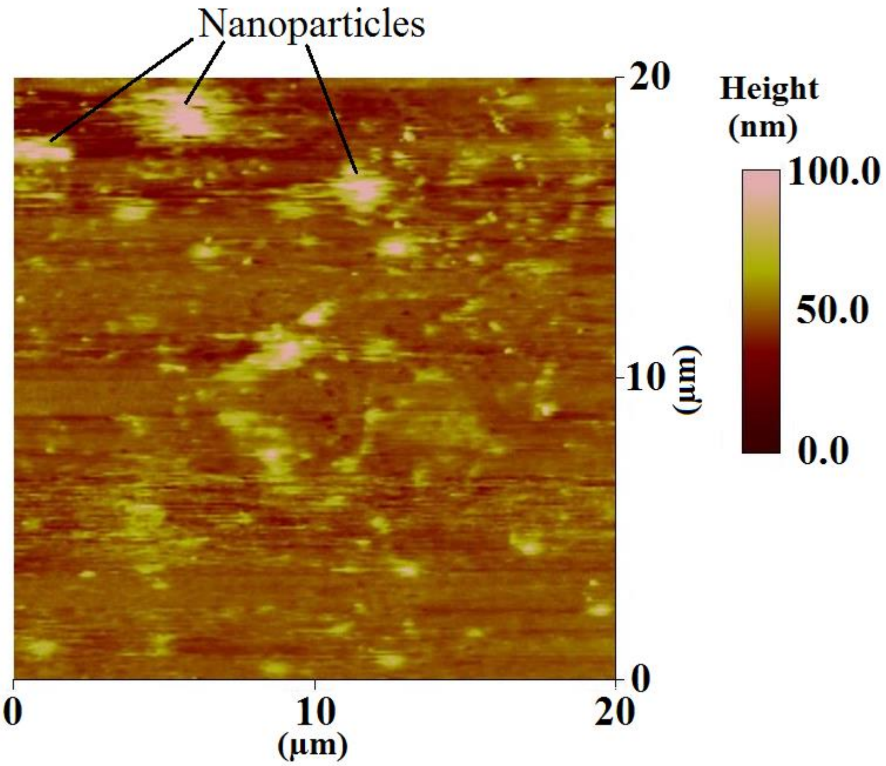

Figure 4.16 Two dimensional AFM image dengue antigen-dextran conjugate onto surface

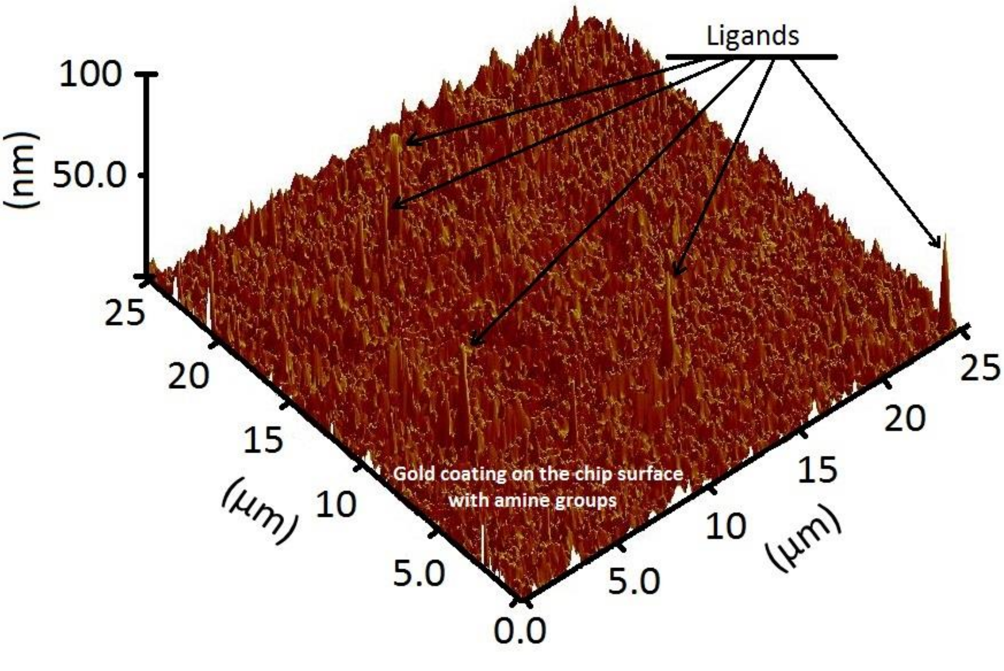

Figure 4.17 Three dimensional AFM image dengue antigen-dextran conjugate onto surface

4.7 Determination of sample concentration

In this section, quantitative analysis is done to find out an optimized concentration of the analyte which is in the fluid sample. For this study, the different concentrations of the analyte are prepared and then applied in the separate analysis cycles for studying the SPR sensor signal. The measured responses (sensorgrams) are presented in the separate plots of Figure 4.18 with similar scale at different concentrations. The association phase of sensorgram is reduced by decreasing analyte concentration. As the concentration of analyte in the sample increases, the rising edge of produced response signal becomes sharper. Hence, the optimum concentration is needed to be determined in order to avoid rapid saturation of sensor signal and to have an appropriate regeneration as well.

All concentration tests are carried out in same conditions and used constant buffers. The patient’s serum, which is diluted in sodium acetate with different concentrations for each experiment, is injected on the sensor surface. Basically the free antibodies which are on the sample bound to dengue antigens (already immobilized on the sensor surface) produce a change in quantity of binding Ag-Ab interaction.

As mentioned, the response sensorgram shows the quantity of binding interaction on the gold surface of the biosensor. With starting the injection of patient’s serum, we are expecting that the response has an upward trend in the baseline level and represents the amount of dengue antibodies bound during injection with its antigens.

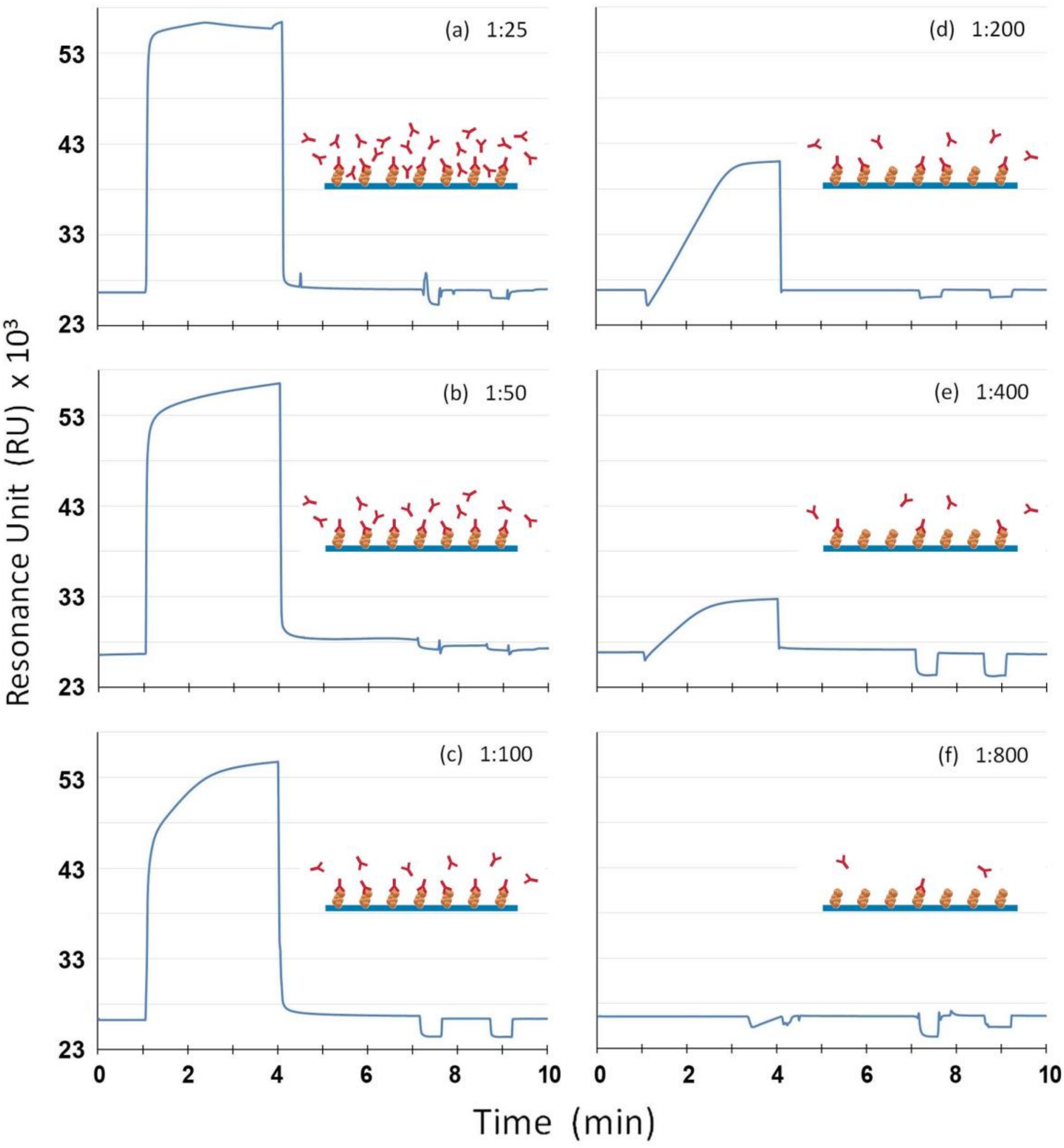

Figure 4.18 Sensorgrams illustrate the evolution of resonance units (RU) versus time during association and dissociation measurements along with biosensor regeneration performed in the Biacore instrument. The inset schematics represent dengue antibodies (Y shapes) versus dengue antigens (immobilized circles on surface)

Upon sensor surface construction, the experiments were conducted by exposing the surface to each concentrated serum containing IgM antibody. The dengue IgM antibody began to bind once the serum was introduced to the sensor surface; a process that continued while an equilibrium position took place between the serum antibody concentration and immobilized dengue antigen concentration. At this point, the process of binding was studied by replacing the liquid phase with a buffer and recording the dissociation of attached antibodies until an equilibrium ratio between dengue IgM antibodies and immobilized antigens was achieved. These basic phases of association and dissociation can be performed at different serum concentrations to examine the effect concentration has on the time-dependent diagnostic process for the dengue virus (Figure 4.18).

Two dips at the end of each sensorgram were anticipated (Figure 4.18) and based on the Biacore setup. They indicate that the chip surface regenerated twice at the end of the process and all Ag-Ab binding was washed out by the glycine buffer. Thereafter, the sensor was ready for the subsequent experiments. The sensor surface was expected to be sufficiently clear for the next binding with minimal influence from prior detection.

Evaluating the kinetic and equilibrium situations' concentration dependence leads to sample volume optimization under this study's particular conditions. This experiment was repeated under the same conditions, whereby all environmental variables (e.g. temperature and buffers) were fixed to examine the effect of sample concentration. The serum was diluted to concentrations of 1:25, 1:50, 1:100, 1:200, 1:400 and 1:800 by adding 10mM sodium acetate solvent with pH 4.5.

In the study of serum concentration generally described in Figure 4.18, a high quantity of dengue antibodies at a 1:25 concentration caused sudden, rapid saturation in the binding phase between antibodies and antigens at the chip surface (Figure 4.18 (a)). Upon saturation, the sensor's accuracy decreased - meaning that virus recognition in the detection procedure was not reliable.

However, the large quantity of antibodies rendered the washing phase difficult owing to the lengthy duration of washing. The importance of the washing phase is more prominent if the chip is used for the following assay. In Figure 4.18, the subplots (a) and (b) show that chip regeneration did not occur adequately. The incomplete regeneration indicates there remained a little Ag-Ab bound onto the chip surface in spite of regeneration having been done twice. The subsequent incoming antibodies (suspended in the next sample) would get bound to the free, immobilized antigens on the surface and combined with previously bound antibody residue. Hence, both concentrations are considered Ag-Ab binding in the next generated signal. The error caused by this chip malfunction affects the entire diagnosis process. With a declining number of antibodies by diluting the serum, their binding to the relevant immobilized antigens caused an exponential bend in the sensorgram. The maximum saturation was still achievable by diluting the serum to 1:100 (Figure 4.18 (c)). At concentrations of 1:200 (Figure 4.18 (d)), 1:400 (Figure 4.18 (e)), and 1:800 (Figure 4.18 (f)), the results signify that the antibodies inside the serums did not attach to the immobilized antigens within the binding timeframe. Consequently, binding in the serum diluted to 1:800 was nearly ineffective (Figure 4.18 (f)). This happened because the low quantity of antibodies in the last sample did not interact enough with the antigens on the surface.

These descriptions indicate the importance of accurate sample concentration. As noted above, the concentration of 1:100 may serve as reference to provide high resolution results. This concentration value also facilitates great surface regeneration and can rely on sample amount for dengue virus detection.

In Figure 4.19, the changing SPR angle and biosensor regeneration were assessed according to the different concentrations. In this comparison, the concentrations of 1:25, 1:50 and 1:100 exhibit the highest percentages of SPR angle alteration, whereas sensor regeneration improved gradually. Although the sensor surface regeneration enhancement is acceptable at more diluted concentrations (1:200, 1:400, and 1:800), the modifications in SPR angle decrease and nearly vanish at 1:800, as explained in the final part. In view of SPR angle variation and regeneration of biosensor parameters, the concentration of 1:100 is practically the best option for dengue virus detection with high sensitivity and optimal chip regeneration.

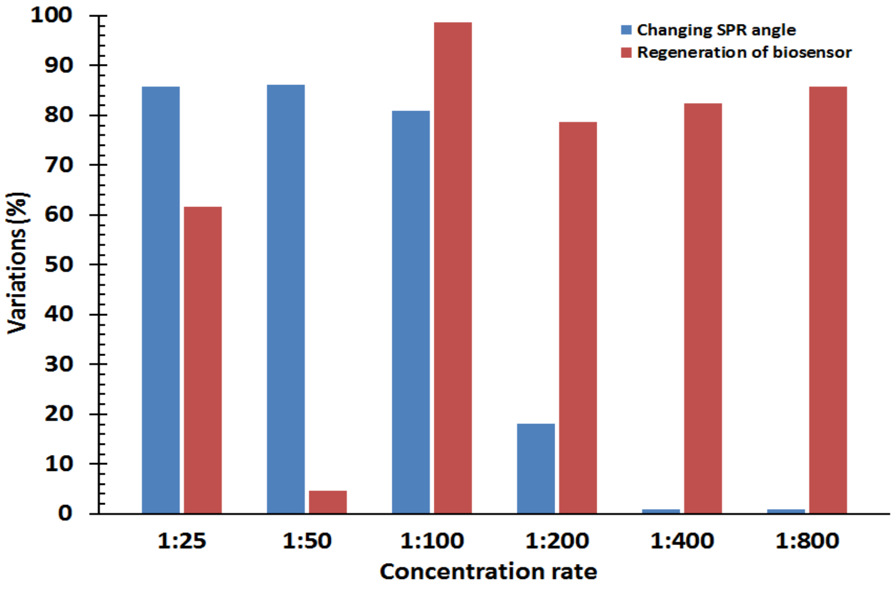

Figure 4.19 (Blue) The stacked column graph represents the quantity of Ag-Ab bound on the sensor surface, which is directly related to the amount of sensor sensitivity; Red represents chip surface cleaning related to the quality of sensor regeneration

4.8 Examination of samples

The binding response sensorgram which resulted from dengue high positive serum (as an example) along with control experiment as a reference, shows the quantity of binding interaction on the gold surface of the biosensor (Figure 4.20). Starting with the injection of patient sample, the response increases exponentially, representing the amount of dengue antibodies bound during injection with its antigens (Figure 4.20 (a)). There will be no binding if the patient sample does not carry the dengue antibodies or is carrying non-dengue antibodies. In this condition, the patient sample is a true negative.

In Figure 4.20 (b), there are two dips located at the end of the sensorgram caused by SPR setup adjustment. The dips indicate that the chip surface is regenerated twice and washed out all Ag-Ab binding (by the glycine buffer). It is expected that the gold surface of the sensor to be cleaned with the least influence of previous binding that can be proved by the control experiment. It should be noted that the whole assay was performed in only ten minutes.

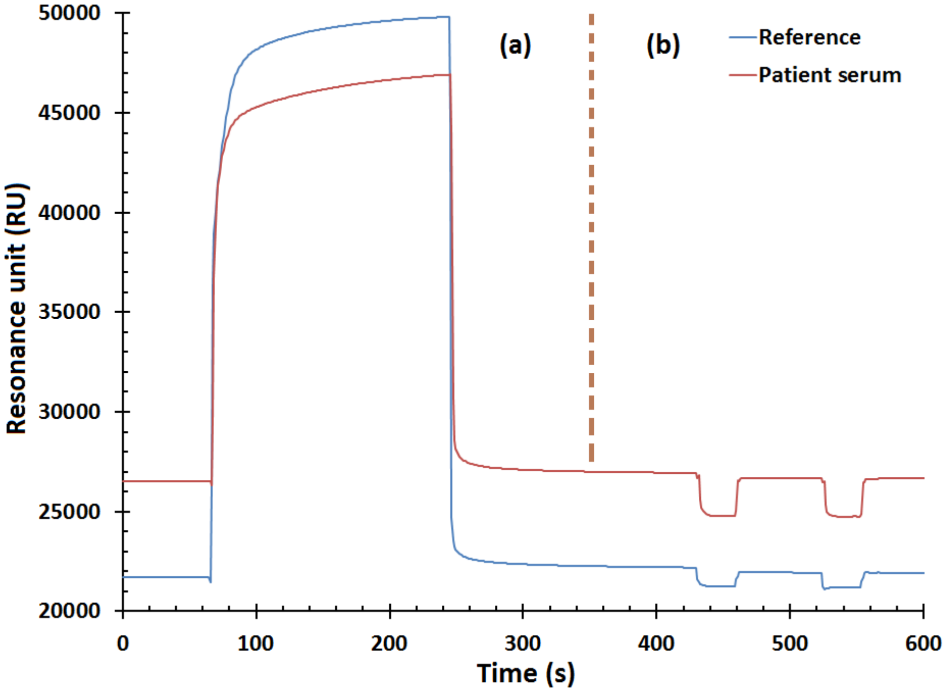

Figure 4.20 The binding response curve termed by sensorgram, (a) the binding process and (b) the regeneration of biosensor surface

Figure 4.21 manifests the SPR angle variations in terms of patient serum. As can be seen, the maximum SPR angle variations occur in high positive (HP), mid positive (MP), and low positive (LP) anti-dengue viruses respectively. Each HPs, MPs, and LPs are the average of ten samples of their types and each bar can also be a reference for diagnosis of each dengue virus types. This method can determine the ratio of four serotypes of dengue virus and by utilizing this ratio, specialists can easily and correctly decide whether to place the patients in observation (hospitalize) or sent home. The SPR angle variations in each serotype of dengue virus tend to have a linear slope. These linearity variations can generate boundaries that are distinguished by HP, MP, and LP.

A comparative study was performed to validate the results that obtained by proposed SPR technique with conventional ELISA method (as presented in Table 4.1). As it can be seen NS1, positive/negative (P/N) ratio and IgM results of each patient serum are displayed based on ELISA method. The first test to be run is NS1 whose positive result indicates the presence of dengue virus in blood, however, to gain further validity, IgM test, too, needs to be conducted. It is vital to do IgM test for final confirmation in samples with negative NS1.

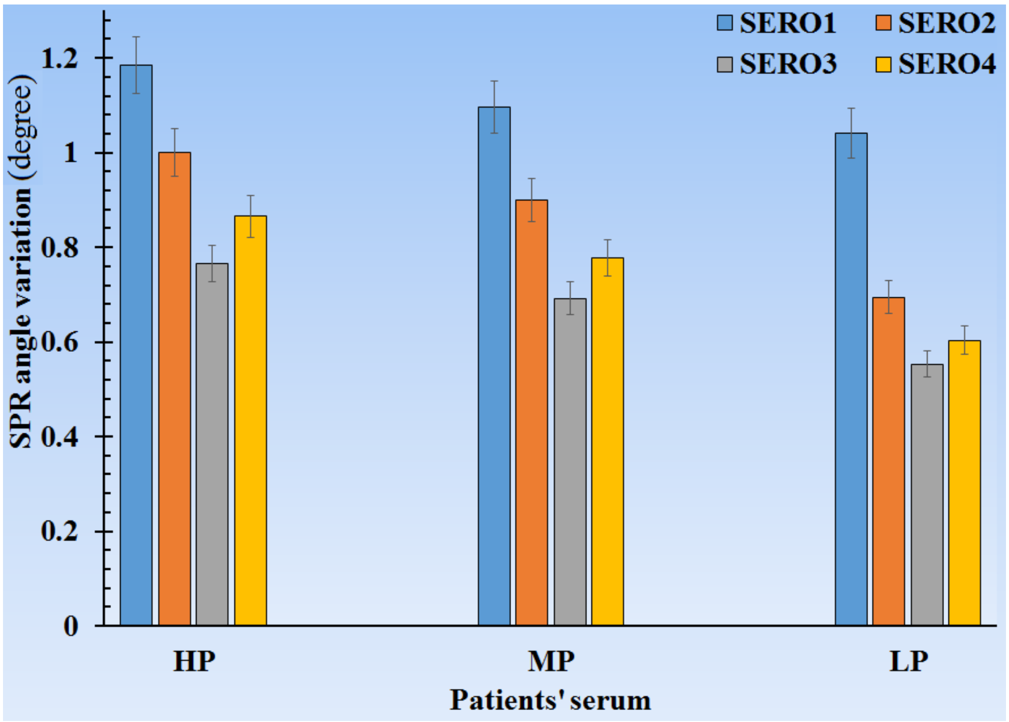

Figure 4.21 SPR angle variation via patient's serum- Dengue virus diagnosis graph

Table 4.1 Comparative data base of ELISA and proposed SPR biosensor in low, mid and high positive patient samples of dengue virus

Type of sample (HI)	**Patient serum**	**ELISA results**			**Biosensor results ($\triangle\theta_{SPR}$)**			
		P/N ratio	**NS1**	**IgM**	**S.T. 1**	**S.T. 2**	**S.T. 3**	**S.T. 4**
Low positive (Antibody titre 10-160)	AH01	2.48	-	+	1.0110	0.7454	0.5808	0.5923
	AH02	2.67	-	+	1.0570	0.7186	0.5845	0.6344
	AH03	2.59	+	+	1.0688	0.7211	0.5785	0.6369
	AH04	2.47	+	+	1.0013	0.6498	0.5499	0.5957
	AH05	2.81	+	+	1.0102	0.6694	0.5162	0.5572
	AH06	2.47	+	+	1.0060	0.6560	0.5080	0.5467
	AH07	2.79	+	+	0.9665	0.6910	0.5548	0.6105
	AH08	2.14	+	+	1.0019	0.7015	0.5002	0.5844
	AH09	2.93	-	+	1.1015	0.7528	0.5775	0.6512
	AH10	2.58	-	+	1.0104	0.7501	0.5771	0.6081
Mid positive (Antibody titre 160-640)	AH11	3.01	+	+	0.9983	0.8863	0.6866	0.7051
	AH12	3.93	+	+	1.0574	0.9095	0.5849	0.8077
	AH13	3.45	-	+	1.1691	0.7965	0.5987	0.7498
	AH14	3.75	+	+	0.9862	0.9380	0.6720	0.7899
	AH15	3.34	-	+	1.1001	0.8754	0.6972	0.7386
	AH16	4.59	-	+	1.1124	0.9566	0.7399	0.8211
	AH17	4.5	+	+	1.1092	0.9487	0.7410	0.8222
	AH18	4.96	+	+	1.1978	0.9637	0.7405	0.8230
	AH19	4.34	-	+	1.0543	0.7688	0.7337	0.6968
	AH20	4.63	+	+	1.1733	0.9598	0.7234	0.8176
High positive (Antibody titre 1280-10240)	AH21	5.25	+	+	1.1255	1.0114	0.7154	0.9045
	AH22	5.69	+	+	1.1469	0.9778	0.7740	0.8304
	AH23	5.12	+	+	1.1344	0.9463	0.7595	0.7983
	AH24	5.6	+	+	1.1226	0.9462	0.7519	0.8084
	AH25	6.53	-	+	1.1215	0.9084	0.7585	0.7845
	AH26	7.13	-	+	1.1987	1.0695	0.7021	0.8793
	AH27	7.32	+	+	1.2731	1.1128	0.8676	0.9519
	AH28	6.06	+	+	1.1996	0.9954	0.7567	0.8922
	AH29	7.02	-	+	1.2453	1.0532	0.8063	0.9476
	AH30	7.38	-	+	1.2782	0.9869	0.7631	0.8541

Table 4.1 contains the positive IgM results proving the presence of dengue virus in all samples through IgM antibody quantity (P/N ratio). The results from the proposed method show the binding ratio between IgM antibody in samples with all four serotypes of the immobilized dengue virus on the chip surface. The changes in the bound antibody quantity to surface in four serotypes were measured by monitoring the surface plasmon resonance angle of each sample.

To know the sensitivity of detection by the sensor, the change of the angle matching the minimum reflection coefficient called SPR angle ($\Delta\theta_{SPR.}$) was calculated for each experiment (Table 4.1). Then the sensitivity of the sensor relates to the test's ability to identify positive results compared with the results of conventional method, which is 83-93% in this research.

The samples with TBE and HC viruses (negative dengue NS1 and subsequently negative dengue IgM results) are presented in Table 4.2. The final outcome of the proposed method indicates that there is an insignificant change in the SPR angle of all four serotypes. Such a small change signals that there is no binding between TBE or HC antibody that exists in samples and the serotypes of dengue virus. According to the Table 4.2, there is no any false positive result, which has overlap with positive range of each serotype. However, the specificity of the biosensor which is 100%, was calculated by examining the sera from this table.

Table 4.2 The negative controls and the number of the serum samples were examined for the specificity evaluation in this study.

Type of sample	**Patient serum**	**ELISA results**		**Biosensor results (|$\Delta\theta_{SPR}$|)**			
		NS1	**IgM**	**S.T. 1**	**S.T. 2**	**S.T. 3**	**S.T. 4**
Tick-Borne Encephalitis	SAM01	-	-	0.31852	0.3760	0.19469	0.32879
	SAM02	-	-	0.15085	0.2557	0.21550	0.19386
	SAM 03	-	-	0.37746	0.2860	0.00040	0.19946
	SAM 04	-	-	0.16855	0.2940	0.04890	0.16955
	SAM 05	-	-	0.14738	0.1254	0.02943	0.13294
	SAM 06	-	-	0.02807	0.1651	0.25771	0.08001
	SAM 07	-	-	0.25098	0.0770	0.18170	0.10140
	SAM 08	-	-	0.03523	0.0973	0.02780	0.07478
	SAM 09	-	-	0.04094	0.0646	0.07810	0.04010
	SAM 10	-	-	0.05042	0.0050	0.01400	0.01260
	SAM 11	-	-	0.24308	0.0911	0.25786	0.04538
	SAM 12	-	-	0.11004	0.0011	0.25924	0.09303
	SAM 13	-	-	0.25980	0.1937	0.21978	0.09314
	SAM 14	-	-	0.35171	0.2944	0.31243	0.20877
	SAM 15	-	-	0.2852	0.1905	0.23039	0.10882
	SAM 16	-	-	0.21199	0.1115	0.14507	0.01650
	SAM 17	-	-	0.22769	0.1312	0.17126	0.03061
	SAM 18	-	-	0.28431	0.1407	0.15434	0.00509
	SAM 19	-	-	0.25883	0.1396	0.17210	0.04012
Hepatitis C	SAM 20	-	-	0.21092	0.1737	0.23510	0.11329
	SAM 21	-	-	0.23587	0.1497	0.24237	0.09972
	SAM 22	-	-	0.30437	0.1798	0.19558	0.06360

4.9 Validating simulation based on experimental results

In this section, the experimental results compare with theoretical results from mathematical analysis. According to the previous section, the change in SPR angle was measured for rapid detection of anti-dengue virus in human serum samples experimentally. Based on the relationship of SPR angle and refractive index, the refractive index changes of binding medium for different serums can be acquired. In order to show the accuracy of theoretical analysis, the obtained refractive index of samples are applied to the proposed SPR configuration which has been presented in the methodology section. Since there are a large number of samples, only one sample from each category of dengue serotypes 2 (low, mid, and high positive) is selected and examined for verification of the analytical analysis. With respect to the samples table (Table 4.1), the SPR angle variation of sample AH 7, AH 12 and AH 29, which are as representative of low, mid, and high positive dengue serotype 2 respectively, is presented along with their refractive index changes in Figure 4.22.

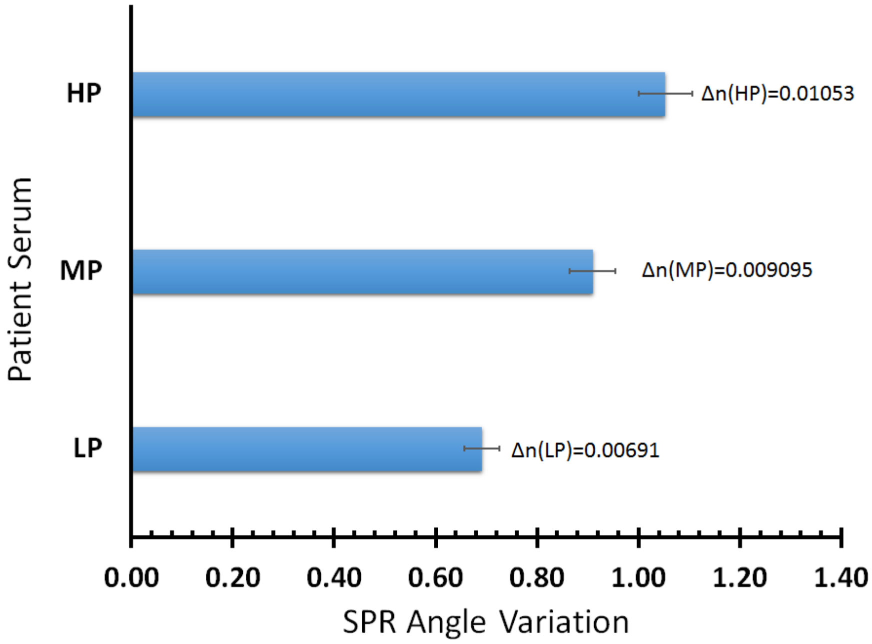

Figure 4.22 Patients' serum via SPR angle variation, and their refractive index changes

Based on samples table, the SPR angle variations were obtained 0.6910°, 0.9095°, and 1.0532° for low, mid, and high positive patients' serums with changing refractive index 0.00691, 0.009095, and 0.01053 respectively.

Based on analytical investigation, the plot of totally reflected intensity versus angle of incidence termed SPR curve was shown in left side of Figure 4.23. To generate a SPR curve, we used a generalized 4-layer model (N = 4). The first layer is prism with refractive index $n_1= n_{prism}$. The k^{th} layer (k: 2 to N-1) has a thickness of d_k and the local dielectric function $\varepsilon_k(\lambda_0)$ or the refractive index $n_k(\lambda_0)$. In λ_0 = 633 nm, there are the prism (n_1= 1.457) | gold (d_2= 50 nm, n_2= 0.2 + i3.32) | linker (d_3= 100 nm, n_3= 1.515) | binding medium, where n_4 was found from experimental results.

Figure 4.23 shows the SPR angle variations based on the mathematical model of SPR structure. As discussed in Chapter 3, the obtained experimental changes in refractive index for each samples were applied in the analytical model. These changes have been schematically illustrated with corresponding sensorgrams in right side of Figure 4.23. The SPR angle variations in low (A), mid (B), and high (C) positive dengue patient serums were calculated 0.654°, 0.85°, and 1.014° respectively.

Table 4.3 shows the mathematical error for dengue detection in low, mid, and high positive patients' serums. According to this table, by experimental investigation on analyte-ligand binding quantity and then analytical analysis of the biosensor based practical conditions, we found the error ratio of each category (~5.35%, 6.54%, and 3.72%) compared to experimental results.

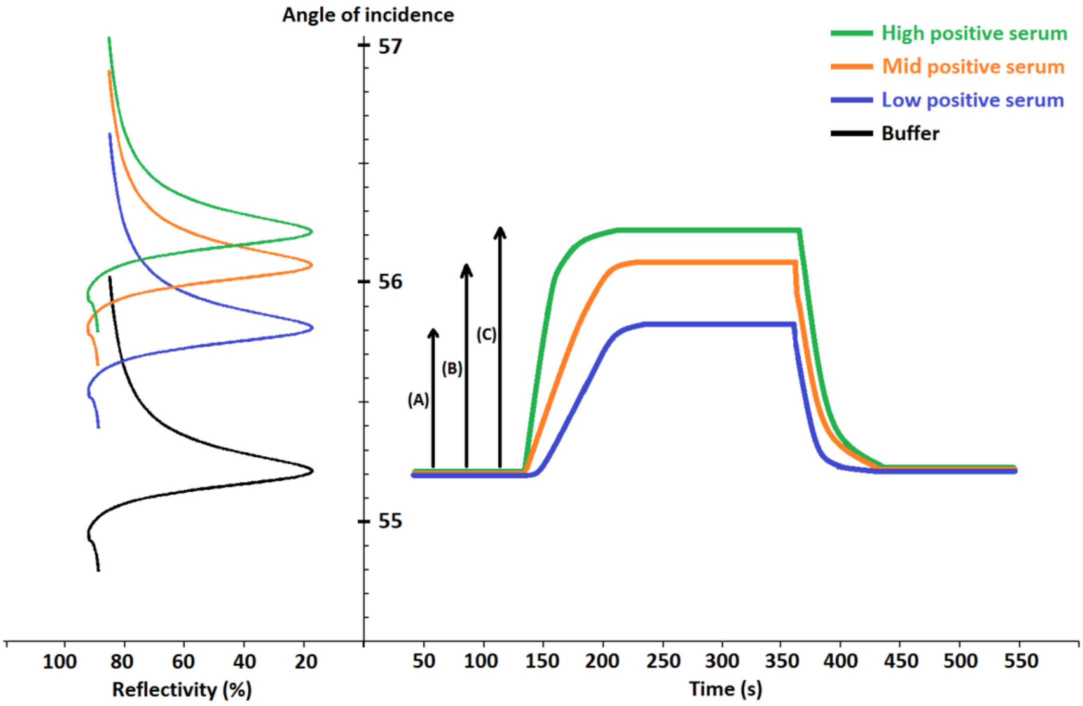

Figure 4.23 The shift of SPR angle which is indicated by reflectivity versus angle of incidence obtained from clinical analysis

Table 4.3 The SPR variations of three categorized serums analytically and experimentally, and their mathematical error

Serum no.	SPR angle variation		Error (%)
	Mathematical	Experimental	
LP_AH 7	0.654	0.6910	5.35
MP_AH 12	0.850	0.9095	6.54
HP_AH 29	1.014	1.0532	3.72

5 CHAPTER V: CONCLUSION AND FUTURE WORK

The aim of the work in this thesis was to develop a technique for dengue rapid diagnostic test. The development of this technique was successfully achieved by employing the SPR method as an optical biosensor.

In this thesis, we applied Drude, Drude-Lorentz, Brendel-Bormann, and Multiple Oscillator models to determine the most compatible and reliable model for SPR sensing studies analytically and numerically. The main focus was on the SPR angle in different wavelengths and also its reflectance in a specific wavelength. The mathematical results revealed that Brendel-Bormann model generated the most accurate real and imaginary permittivity values for the materials used in the proposed SPR structure, within the wavelengths of interest. Moreover the Brendel-Bormann model results was more stable and close to the experimental data as compared to the other models. The final numerical analysis has been performed by simulating the power-flow of the SPR structure. The numerical results supported mathematical work and proved that Brendel-Bormann model can be trustable as its continuum is perfectly matched with the experimental data calculated power-flow.

The value of the optimizing sample concentrations were determined by careful examination of the different concentrations of sample, this is one of the main contributions of this study. In order to obtain the well-regeneration of biochip, the sample volume was optimized to the minimum amount of 1 µl of serum while maintaining high sensitivity.

We then showed that the proposed SPR based biosensor is satisfactory for direct determination of dengue Ag-Ab binding interaction on the sensor surface. Experimental and computational investigations have been carried out in order to determine the dengue Ag-Ab interactions occurring on the surface of the SPR biosensor. This study indicated that the shifting of SPR angle in experimental and analytical results conform to each other. The magnetic fields of the sensor surface were numerically simulated to show the effect of different binding mediums. The SPR technique, despite of the conventional methods, provides a rapid detection of dengue Ag-Ab interaction (i.e. around 10 minutes).

To investigate the four serotypes of dengue virus, the antigens of each serotype were immobilized on the chip surface. A number of patient serums (categorized to the low, mid, and high positive anti-dengue viruses) were passed onto the immobilized ligand. The results showed that using the proposed method, the anti-dengue virus IgM in human serum can be detected with high sensitivity and specificity responses.

According to the findings of this study, a specific portable device could be designed and fabricated for rapid diagnostic tests of dengue fever in medical centers.

The presented work can be used to investigate several areas in the future. In the sensing applications, this early detection technique can also be expanded to include an identification of specific antibodies of other diseases such as Japanese encephalitis (JE) and yellow fever.

APPENDIX A: Derivation dispersion relation; SP's on planar surface

With H_z given by

$$\vec{H}_z = A \cdot \exp\{j(\omega t - q_x x)\} \cdot \exp(\alpha_m y) \cdot \vec{u}_y \quad (y < 0, metal) \qquad \text{A.1}$$

$$\vec{H}_z = B \cdot \exp\{j(\omega t - q_x x)\} \cdot \exp(-\alpha_d y) \cdot \vec{u}_y \quad (y > 0, dielectric) \qquad \text{A.2}$$

and the Helmholtz wave equation

$$\nabla^2 H_z = -\omega \mu_0 \varepsilon_0 \varepsilon_r H_z 0 \qquad \text{A.3}$$

the reciprocal penetration depths α_m and α_d are obtained by substituting and Equation A.2 into Equation A.3:

$$\alpha_m = \sqrt{{q_x}^2 - {k_0}^2 \varepsilon_m} \qquad \text{A.4}$$

$$\alpha_d = \sqrt{{q_x}^2 - {k_0}^2 \varepsilon_d} \qquad \text{A.5}$$

With Maxwell's Equation A.**4**

$$\nabla \times \vec{H} = \begin{vmatrix} \vec{u}_x & \vec{u}_y & \vec{u}_z \\ \partial_x & \partial_y & \partial_z \\ 0 & 0 & H_z \end{vmatrix} = i\omega \varepsilon_0 \varepsilon_r \vec{E} \qquad \text{A.6}$$

and the boundary condition for the tangential components of E at $y = 0$ yields

$$\frac{1}{\varepsilon_0 \varepsilon_m} \partial_y H_z = \frac{1}{\varepsilon_0 \varepsilon_d} \partial_y H_z \qquad \text{A.7}$$

where $\partial x = \partial/\partial x$, likewise for y and z. Substituting Equation A.1 and Equation A.2 into Equation A.7 yields 2.37. The same method can be used to verify that TE-plasmons cannot exist on a flat metal surface. To this end, E_z is given in the same form as H_z for TM-plasmons:

$$\vec{E}_z = A \cdot \exp\{j(\omega t - q_x x)\} \cdot \exp(\alpha_m y) \cdot \vec{u}_y \quad (y < 0, metal) \qquad \text{A.8}$$

$$\vec{E}_z = B \cdot \exp\{j(\omega t - q_x x)\} \cdot \exp(-\alpha_d y) \cdot \vec{u}_y \quad (y > 0, dielectric) \qquad \text{A.9}$$

with α_m and α_d given by Equation A.4 and Equation A.5. With Maxwell's 2.3 and the boundary condition that the tangential component of ***H*** is continuous across the interface, one obtains

$$\nabla \times \vec{E} = \begin{vmatrix} \vec{u}_x & \vec{u}_y & \vec{u}_z \\ \partial_x & \partial_y & \partial_z \\ 0 & 0 & H_z \end{vmatrix} = -i\omega\mu_0\mu_r\vec{H} \qquad \text{A.10}$$

$$\frac{1}{\mu_m}\partial_y E_z = \frac{1}{\mu_d}\partial_y E_z \qquad \text{A.11}$$

$$-\frac{\alpha_m}{\mu_m} = \frac{\alpha_d}{\mu_d} \qquad \text{A.12}$$

In order to satisfy Equation A.12 either μ_m or μ_d has to be negative. However, the relative permeability μ_r is constant and almost unity (or more precisely $\mu_r > 0$) for all metals at optical frequencies; hence no TE-plasmons can be excited.

APPENDIX B: Investigation of chip surface

There is a wide range of analytical techniques which can be used for characterization of materials based on the type of information required from surface structure down to nanometer scale. For surface investigation with high resolution, the two typically used techniques are atomic force and scanning electron microscopies.

Since the ligands (dengue antigens) were immobilized onto the gold thin film, the sensor chip (Figure B. 1); whether the properties of the layers and microscopic images of highest layer; will be investigated using AFM and SEM machines. In the following the required instruments will be introduced and accordingly discussed on their results in results and discussions section.

Figure B. 1 The separated portion of sensor chip for studying its structure

I. Atomic force microscopy image

The atomic force microscopy (AFM) consists a scan of a sharp tip at the end of a flexible cantilever onto a sample surface with a small constant force. The tip-sample interactions are monitored to reflect a laser off the rear of the cantilever in the split photodiode detector. By determining the difference of photo-detector output voltages, the cantilever deflection changes and subsequently oscillation amplitude are specified.

The site of antigen (Ag) immobilization was characterized using atomic force microscopy (VEECO DIMENSION 3000 AFM; Figure B. 2). AFM imaging was performed in contact mode using 0.01-0.025 Ohm-cm antimony with the integrated silicon tip and its cantilever. The 2D and 3D AFM images help to prove the existence of immobilized antigens.

Figure B. 2 The atomic force microscopy instrument- Department of Physics, UM

II. Scanning electron microscope image

The operation of the scanning electron microscopy (SEM) consists an applied voltage between the conductive pattern and filament, which results at electron emission from the filament to the pattern (as a sample). It happens at a range of vacuum environment from 10^{-4} to 10^{-10} Torr. The electrons are conducted to the sample by an electromagnetic lenses series in the column of electrons. The scanning electron microscopy (FE/SEM-FEG) focused ion beam technique (model Quanta FEG250; Figure B. 3), is used for our investigation.

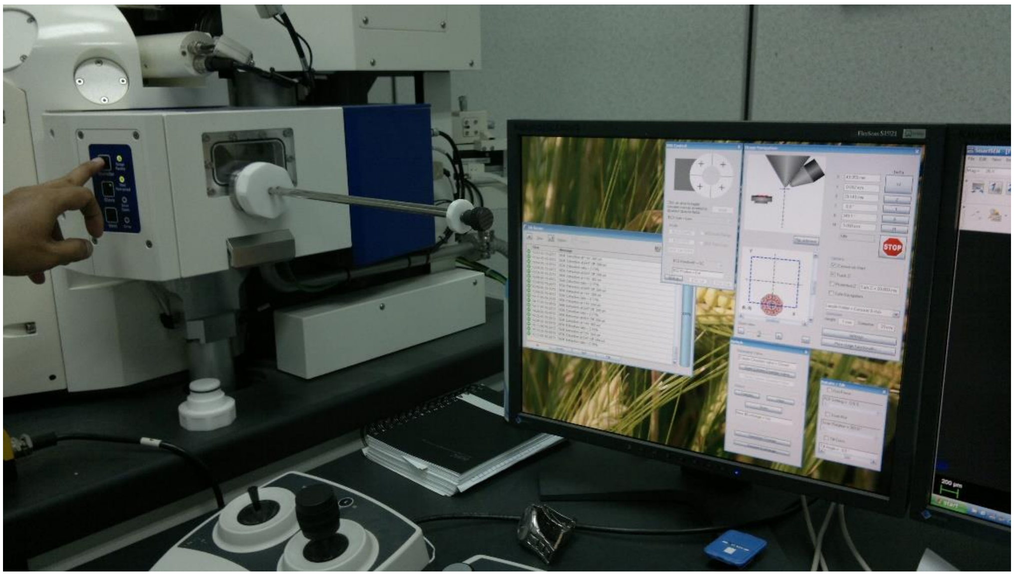

Figure B. 3 The scanning electron microscope instrument- Faculty of Engineering, UM

APPENDIX C: List of Publications, patent and innovation

Journal papers

- **Peyman Jahanshahi**, Erfan Zalnezhad, Shamala Devi Sekaran & Faisal Rafiq Mahamd Adikan; "**Rapid Immunoglobulin M-Based Dengue Diagnostic Test Using Surface Plasmon Resonance Biosensor**", Nature Scientific Reports, 2014.
- **Peyman Jahanshahi**, Mostafa Ghomeishi, and Faisal Rafiq Mahamd Adikan; "**Study on Dielectric Function Models for Surface Plasmon Resonance Structure**", Scientific World Journal, 2014.
- **Peyman Jahanshahi**, Shamala Devi Sekaran, and Faisal Rafiq Mahamd Adikan; "**Optical and Analytical Investigations on Dengue Virus Rapid Diagnostic Test for IgM Antibodies Detection**", Medical & Biological Engineering & Computing, Minor Revision.
- **Peyman Jahanshahi**, Mostafa Ghomeishi, Shamala Devi Sekaran & Faisal Rafiq Mahamd Adikan; **"Kinetic Analysis of IgM Monoclonal Antibodies for Determination of Dengue Sample Concentration Using SPR Technique",** Biomedical Optics Express, Under Revision.

Proceeding/Conference papers

- **Peyman Jahanshahi**, Elian Dermosesian, and Faisal Rafiq Mahamd Adikan; "**Numerical and analytical investigation of a SPR structure as Biosensor**", Frontiers in Optics (FiO) Conference, 19-23th October 2014, USA.
- **Peyman Jahanshahi**, Barmak Honarvar Shakibaei, Shee Yu Gang and Faisal Rafiq Mahamd Adikan; "**Numerical Analysis of SPR-Based Optical Fiber Biosensor**", 5th International Conference on Photonics 2014 (ICP2014), 2014, Malaysia.

- **Peyman Jahanshahi** and Faisal Rafiq Mahamd Adikan; "**Sensitivity Enhancement of Graphene-Based Surface Plasmon Resonance Biosensor Using Germanium Nanowires Grating**", Journal of Medical and Bioengineering (JOMB), 2014, Australia.
- **Peyman Jahanshahi**, Amin Parvizi, Faisal Rafiq Mahamd Adikan; **"Three-dimensional modeling of surface plasmon resonance based biosensor"**, Proc. SPIE 8801, Novel Biophotonic Techniques and Applications II, 2013, Germany.
- **Peyman Jahanshahi**, Hamid Toloue A.T, Anthony Ceteno, and Faisal Rafiq Mahamd Adikan; "**Numerical Analysis of Surface Plasmon Resonance Biosensor Based on Graphene Layer**", The 8th AOTULE Deans Meeting, Administrative Staff Meeting and Postgraduate Conference, 2013, Thailand.
- **Peyman Jahanshahi**, Mostafa Ghomeishi, and Faisal Rafiq Mahamd Adikan; "**Adhesive Layer Effect on Gold-Silica Thin Film Interfaces for Surface Plasmon Resonance Modeling**", 3rd International Conference on Photonics, 2012, Malaysia.

Patent and Innovation

- **NEW TECHNIQUE TO DIAGNOSE THE DENGUE VIRUS,** Patent no.: PI2014702566, 2014.
  - ✓ Name of Principal Investigator/ Inventor: **Faisal Rafiq Mahamd Adikan**
    Position: **Professor**
    Faculty/Department: **Electrical Engineering**
  - ✓ Name of Co-Investigator/Co-Inventor: **Peyman Jahanshahi**
    Position: **PhD. Candidate/Research Assistant**
    Faculty/Department: **Engineering/Electrical Engineering**
  - ✓ Name of Co-Investigator/Co-Inventor: **Erfan Zal Nezhad**
    Position: **Doctor**
    Faculty/Department: **Engineering/Mechanical Engineering**
  - ✓ Name of Co-Investigator/Co-Inventor: **Shamala Devi Sekaran**
    Position: **Professor**
    Faculty/Department: **Medicine/Microbiology**

- **5TH EXPOSITION ON ISLAMIC INNOVATION (i-Inova2014),** Nilai Indoor Stadium, Negeri Sembilan, Malaysia, be held on 31st October - 2nd November 2014.
    - ✓ Name of Principal Investigator/ Inventor: **Faisal Rafiq Mahamd Adikan**
      Position: **Professor**
      Faculty/Department: **Electrical Engineering**
    - ✓ Name of Co-Investigator/Co-Inventor: **Peyman Jahanshahi**
      Position: **PhD. Candidate/Research Assistant**
      Faculty/Department: **Engineering/Electrical Engineering**
    - ✓ Name of Co-Investigator/Co-Inventor: **Erfan Zal Nezhad**
      Position: **Doctor**
      Faculty/Department: **Engineering/Mechanical Engineering**
    - ✓ Name of Co-Investigator/Co-Inventor: **Shamala Devi Sekaran**
      Position: **Professor**
      Faculty/Department: **Medicine/Microbiology**

REFERENCES

Abarbanel, S., & Gottlieb, D. (1997). A Mathematical Analysis of the PML Method. *Journal of Computational Physics*, *134*(2), 357–363.

Abdelghani, A., Chovelon, J. M., Jaffrezic-Renault, N., Ronot-Trioli, C., Veillas, C., & Gagnaire, H. (1997). Surface plasmon resonance fibre-optic sensor for gas detection. *Sensors and Actuators B: Chemical*, *39*(1), 407–410.

Abdulhalim, I., Zourob, M., & Lakhtakia, A. (2008). Surface plasmon resonance for biosensing: a mini-review. *Electromagnetics*, *28*(3), 214–242.

Ahmet Arca. (2010). *The design and optimisation of nanophotonic devices using the Finite Element Method*. University of Nottingham.

Amotchkina, T. V, Trubetskov, M. K., Tikhonravov, A. V, Janicki, V., Sancho-Parramon, J., & Zorc, H. (2011). Comparison of two techniques for reliable characterization of thin metal-dielectric films. *Applied Optics*, *50*(33), 6189–97.

Ashley, J. C., & Emerson, L. C. (1974). Dispersion relations for non-radiative surface plasmons on cylinders. *Surface Science*, *41*(2), 615–618.

Azzam, R. M. A., & Bashara, N. M. (1987). *Ellipsometry and polarized light*. North-Holland. sole distributors for the USA and Canada, Elsevier Science Publishing Co., Inc.

Barnes, W. L., Dereux, A., & Ebbesen, T. W. (2003). Surface plasmon subwavelength optics. *Nature*, *424*(6950), 824–830.

Berini, P. (1999). Plasmon polariton modes guided by a metal film of finite width. *Optics Letters*, *24*(15), 1011–1013.

Berini, P. (2006). Figures of merit for surface plasmon waveguides. *Optics Express*, *14*(26), 13030–42.

Berini, P. (2008). Bulk and surface sensitivities of surface plasmon waveguides. *New Journal of Physics*, *10*(10), 105010.

Berini, P. (2009). Long-range surface plasmon polaritons. *Advances in Optics and Photonics*, *1*(3), 484.

Bhatia, P., & Gupta, B. D. (2012). Sensors and Actuators B : Chemical Fabrication and characterization of a surface plasmon resonance based fiber optic urea sensor for biomedical applications. *Sensors & Actuators: B. Chemical*, *161*(1), 434–438.

Bhatt, S., Gething, P. W., Brady, O. J., Messina, J. P., Farlow, A. W., Moyes, C. L., … others. (2013). The global distribution and burden of dengue. *Nature*.

Bohm, D., & Pines, D. (1951). A collective description of electron interactions. I. Magnetic interactions. *Physical Review*, *82*(5), 625.

Bohm, D., & Pines, D. (1953). A collective description of electron interactions: III. Coulomb interactions in a degenerate electron gas. *Physical Review*, *92*(3), 609.

Boltovets, P. M., Snopok, B. a, Boyko, V. R., Shevchenko, T. P., Dyachenko, N. S., & Shirshov, Y. M. (2004). Detection of plant viruses using a surface plasmon resonance via complexing with specific antibodies. *Journal of Virological Methods*, *121*(1), 101–6.

Bozhevolnyi, S. I. (2006). Effective-index modeling of channel plasmon polaritons. *Optics Express*, *14*(20), 9467–9476.

Brenner, S. C., & Scott, R. (2008). *The mathematical theory of finite element methods* (Vol. 15). Springer.

Brongersma, M. L., & Kik, P. G. (2007). *Surface plasmon nanophotonics* (Vol. 131). Springer Berlin.

Burke, J. J., Stegeman, G. I., & Tamir, T. (1986). Surface-polariton-like waves guided by thin, lossy metal films. *Physical Review B*, *33*(8), 5186.

Campbell, C. T., & Kim, G. (2007). SPR microscopy and its applications to high-throughput analyses of biomolecular binding events and their kinetics. *Biomaterials*, *28*(15), 2380–92.

Chadwick, B., & Gal, M. (1993). An optical temperature sensor using surface plasmons. *Japanese Journal of Applied Physics*, *32*(6A), 2716–2717.

Cheesbrough, M. (2006). *District laboratory practice in tropical countries* (Vol. 2). Cambridge university press.

Chen, S.-J., Chien, F. C., Lin, G. Y., & Lee, K. C. (2004). Enhancement of the resolution of surface plasmon resonance biosensors by control of the size and distribution of nanoparticles. *Optics Letters*, *29*(12), 1390–1392.

Chernozatonskii, L. A., Ermoshin, S. N., & Gramotnev, D. K. (1991). Coupled Gulyayev-Bleustein waves in a system of two different piezoelectrics separated by a gap. *Physics Letters A*, *154*(9), 465–470.

Chhatre, A., Solasa, P., Sakle, S., Thaokar, R., & Mehra, A. (2012). Colloids and Surfaces A : Physicochemical and Engineering Aspects Color and surface plasmon effects in nanoparticle systems : Case of silver nanoparticles prepared by microemulsion route. *Colloids and Surfaces A: Physicochemical and Engineering Aspects*, *404*, 83–92.

Chinowsky, T. M., Saban, S. B., & Yee, S. S. (1996). Experimental data from a trace metal sensor combining surface plasmon resonance with anodic stripping voltammetry. *Sensors and Actuators B: Chemical*, *35*(1), 37–43.

Courant, R., & others. (1943). Variational methods for the solution of problems of equilibrium and vibrations. *Bull. Amer. Math. Soc*, *49*(1), 1–23.

Crowther, J. R. (2000). *The ELISA guidebook* (Vol. 149). Springer.

DaCosta, R. S., Wilson, B. C., & Marcon, N. E. (2005). Optical techniques for the endoscopic detection of dysplastic colonic lesions. *Current Opinion in Gastroenterology*, *21*(1), 70–79.

Djurisic, A. B., Fritz, T., & Leo, K. (2000). Modelling the optical constants of organic thin films: impact of the choice of objective function. *Journal of Optics A: Pure and Applied Optics*, *2*(5), 458.

Document_not_found. (n.d.). Document not found ((Sang, L. S. Hoon, a Cuzzubbo, et al., 1998; Tricou et al., 2010)).

Dostálek, J., & Knoll, W. (2008). Biosensors based on surface plasmon-enhanced fluorescence spectroscopy (Review). *Biointerphases*, *3*(3), FD12–FD22.

Dragoman, M., & Dragoman, D. (2008). Plasmonics: Applications to nanoscale terahertz and optical devices. *Progress in Quantum Electronics*, *32*(1), 1–41.

Dussart, P., Petit, L., Labeau, B., Bremand, L., Leduc, A., Moua, D., … Baril, L. (2008). Evaluation of two new commercial tests for the diagnosis of acute dengue virus infection using NS1 antigen detection in human serum. *PLoS Neglected Tropical Diseases*, *2*(8), e280.

Dutra, N. R., de Paula, M. B., de Oliveira, M. D., de Oliveira, L. L., & De Paula, S. O. (2009). The laboratorial diagnosis of dengue: applications and implications. *Journal of Global Infectious Diseases*, *1*(1), 38–44.

Duzgun, A., Schuntner, C. A., Wright, I. G., Leatch, G., & Waltisbuhl, D. J. (1988). A sensitive ELISA technique for the diagnosis of< i> Anaplasma marginale</i> infections. *Veterinary Parasitology*, *29*(1), 1–7.

Economou, E. N. (1969). Surface plasmons in thin films. *Physical Review*, *182*(2), 539.

Englebienne, P., Hoonacker, A. Van, & Verhas, M. (2003). Surface plasmon resonance: principles, methods and applications in biomedical sciences. *Spectroscopy*, *17*(2,3), 255–273.

Fano, U. (1941). The theory of anomalous diffraction gratings and of quasi-stationary waves on metallic surfaces (Sommerfeld’s waves). *JOSA*, *31*(3), 213–222.

Fatemeh, D., Reza, Z. M., Mohammad, A., Salomeh, K., Reza, A. G., Hossein, S., … others. (2014). Rapid detection of coliforms in drinking water of Arak city using multiplex PCR method in comparison with the standard method of culture (Most Probably Number). *Asian Pacific Journal of Tropical Biomedicine*, *4*(5), 404.

Fox, A. M. (2001). *Optical properties of solids* (Vol. 3). Oxford university press.

Fry, S. R., Meyer, M., Semple, M. G., Simmons, C. P., Sekaran, S. D., Huang, J. X., … Cooper, M. a. (2011). The diagnostic sensitivity of dengue rapid test assays is significantly enhanced by using a combined antigen and antibody testing approach. *PLoS Neglected Tropical Diseases*, *5*(6), e1199.

Garg, R. (2008). *Analytical and computational methods in electromagnetics*. Artech house.

GE Healthcare. (2008). *Biacore 3000 Instrument Handbook*.

General Electric Company, Biacore. (2014).

Ghosh, G. (1998). *Handbook of Optical Constants of Solids: Handbook of Thermo-Optic Coefficients of Optical Materials with Applications*. Academic Press.

Gibson, W. C. (2007). *The method of moments in electromagnetics*. CRC press.

Girard, C., & Dereux, A. (1996). Near-field optics theories. *Reports on Progress in Physics*, *59*(5), 657.

Goodrich, T. T., Lee, H. J., & Corn, R. M. (2004). Direct detection of genomic DNA by enzymatically amplified SPR imaging measurements of RNA microarrays. *Journal of the American Chemical Society*, *126*(13), 4086–4087.

Gordon Ii, J. G., & Ernst, S. (1980). Surface plasmons as a probe of the electrochemical interface. *Surface Science*, *101*(1), 499–506.

Gramotnev, D. K. (2005). Adiabatic nanofocusing of plasmons by sharp metallic grooves: Geometrical optics approach. *Journal of Applied Physics*, *98*(10), 104302.

Gramotnev, D. K., & Vernon, K. C. (2007). Adiabatic nano-focusing of plasmons by sharp metallic wedges. *Applied Physics B*, *86*(1), 7–17.

Gubler, D. J., & Clark, G. G. (1995). Dengue/dengue hemorrhagic fever: the emergence of a global health problem. *Emerging Infectious Diseases*, *1*(2), 55.

Guzman, M. G., Jaenisch, T., Gaczkowski, R., Hang, V. T. T., Sekaran, S. D., Kroeger, A., … others. (2010). Multi-country evaluation of the sensitivity and specificity of two commercially-available NS1 ELISA assays for dengue diagnosis. *PLoS Neglected Tropical Diseases*, *4*(8), e811.

Hagness, S. C., & Taflove, A. (2000). Computational Electrodynamics: The Finite-Difference Time-Domain Method (Artech House Antennas And Propagation Library) A.

He, H., Yuan, Y., Wang, W., Chiou, N.-R., Epstein, A. J., & Lee, L. J. (2009). Design and testing of a microfluidic biochip for cytokine enzyme-linked immunosorbent assay. *Biomicrofluidics*, *3*(2), 22401.

Hertel, P. (2011). The Drude Model Model, (November).

Hessel, A., & Oliner, A. A. (1965). A new theory of Wood’s anomalies on optical gratings. *Applied Optics*, *4*(10), 1275–1297.

Homola, J. (2003). Present and future of surface plasmon resonance biosensors. *Analytical and Bioanalytical Chemistry*, *377*(3), 528–539.

Homola, J. (2008). Surface plasmon resonance sensors for detection of chemical and biological species. *Chemical Reviews*, *108*(2), 462–93.

Homola, J., Dostalek, J., Chen, S., Rasooly, A., Jiang, S., & Yee, S. S. (2002). Spectral surface plasmon resonance biosensor for detection of staphylococcal enterotoxin B in milk. *International Journal of Food Microbiology*, *75*(1), 61–69.

Homola, J. iˇrí. (2006a). Electromagnetic theory of surface plasmons. In *Surface Plasmon Resonance Based Sensors* (pp. 3–44). Springer.

Homola, J. iˇrí. (2006b). *Surface plasmon resonance based sensors* (Vol. 4). Springer.

Homola, J., Yee, S. S., & Gauglitz, G. (1999). Surface plasmon resonance sensors: review. *Sensors and Actuators B: Chemical*, *54*(1–2), 3–15.

Honório, N. A., Nogueira, R. M. R., Codeço, C. T., Carvalho, M. S., Cruz, O. G., Magalhães, M. de A. F. M., … others. (2009). Spatial evaluation and modeling of dengue seroprevalence and vector density in Rio de Janeiro, Brazil. *PLoS Neglected Tropical Diseases*, *3*(11), e545.

Huebner, K. H., Dewhirst, D. L., Smith, D. E., & Byrom, T. G. (2008). *The finite element method for engineers*. John Wiley & Sons.

Hunsperger, E. a, Yoksan, S., Buchy, P., Nguyen, V. C., Sekaran, S. D., Enria, D. a, … Peeling, R. W. (2009). Evaluation of commercially available anti-dengue virus immunoglobulin M tests. *Emerging Infectious Diseases*, *15*(3), 436–40.

Hutter, E., & Fendler, J. H. (2004). Exploitation of localized surface plasmon resonance. *Advanced Materials*, *16*(19), 1685–1706.

I. Nomadics, Sensiq website. (2014).

Initiative, P. D. V., & others. (2005). Dengue diagnostics: proceedings of a joint TDR/WHO and PDVI workshop: 4-6 October 2004, Geneva, Switzerland.

J. A. C. Weideman. (1994). Computation of the Complex Error Function.

Jönsson, U., Fägerstam, L., Ivarsson, B., Johnsson, B., Karlsson, R., Lundh, K., … Rönnberg, I. (1991). Real-time biospecific interaction analysis using surface plasmon resonance and a sensor chip technology. *Biotechniques*, *11*(5), 620–627.

Jung, C. C., Saban, S. B., Yee, S. S., & Darling, R. B. (1996). Chemical electrode surface plasmon resonance sensor. *Sensors and Actuators B: Chemical*, *32*(2), 143–147.

Kim, E., DeMarco, S. J., Marfatia, S. M., Chishti, A. H., Sheng, M., & Strehler, E. E. (1998). Plasma membrane Ca2+ ATPase isoform 4b binds to membrane-associated guanylate kinase (MAGUK) proteins via their PDZ (PSD-95/Dlg/ZO-1) domains. *Journal of Biological Chemistry*, *273*(3), 1591–1595.

Knoll, W. (1998). Interfaces and thin films as seen by bound electromagnetic waves. *Annual Review of Physical Chemistry*, *49*(1), 569–638.

Koubova, V., Brynda, E., Karasova, L., Škvor, J., Homola, J., Dostalek, J., … Rošick\`y, J. (2001). Detection of foodborne pathogens using surface plasmon resonance biosensors. *Sensors and Actuators B: Chemical*, *74*(1), 100–105.

Kretschmann, E., & Raether, H. (1968). Radiative decay of non radiative surface plasmons excited by light(Surface plasma waves excitation by light and decay into photons applied to nonradiative modes). *Zeitschrift Fuer Naturforschung, Teil A*, *23*, 2135.

Kumarasamy, V., Chua, S. K., Hassan, Z., Wahab, a H. a, Chem, Y. K., Mohamad, M., & Chua, K. B. (2007). Evaluating the sensitivity of a commercial dengue NS1 antigen-capture ELISA for early diagnosis of acute dengue virus infection. *Singapore Medical Journal*, *48*(7), 669–73.

Kumarasamy, V., Wahab, a H. A., Chua, S. K., Hassan, Z., Chem, Y. K., Mohamad, M., & Chua, K. B. (2007). Evaluation of a commercial dengue NS1 antigen-capture ELISA for laboratory diagnosis of acute dengue virus infection. *Journal of Virological Methods*, *140*(1-2), 75–9.

Kumbhat, S., Sharma, K., Gehlot, R., Solanki, A., & Joshi, V. (2010). Surface plasmon resonance based immunosensor for serological diagnosis of dengue virus infection. *Journal of Pharmaceutical and Biomedical Analysis*, *52*(2), 255–9.

Lazcka, O., Campo, F., & Munoz, F. X. (2007). Pathogen detection: a perspective of traditional methods and biosensors. *Biosensors and Bioelectronics*, *22*(7), 1205–1217.

Lee, K. (2008). *World Health Organisation*. Routledge.

Liedberg, B., Nylander, C., & Lundström, I. (1995). Biosensing with surface plasmon resonance—how it all started. *Biosensors and Bioelectronics*, *10*(8), i–ix.

Liedberg, B., Nylander, C., & Lunström, I. (1983). Surface plasmon resonance for gas detection and biosensing. *Sensors and Actuators*, *4*(0), 299–304.

Lim, V. (2009). Occupational infections. *Malaysian J Pathol*, *31*(1), 1–9.

Maier, S. A. (2007). *Plasmonics: fundamentals and applications*. Springer.

Margheri, G., D’Agostino, R., Becucci, L., Guidelli, R., Tiribilli, B., & Del Rosso, M. (2012). Surface plasmon resonance as detection tool for lipids lateral mobility in biomimetic membranes. *Biomedical Optics Express*, *3*(12), 3119–3126.

Margheri, G., Mannoni, A., & Quercioli, F. (1997). High-resolution angular and displacement sensing based on the excitation of surface plasma waves. *Applied Optics*, *36*(19), 4521–4525.

Martinos, S. S., & Economou, E. N. (1981). Excitation of surface plasmons in cylinders by electrons. *Physical Review B*, *24*, 6908–6914.

Martinos, S. S., & Economou, E. N. (1983). Virtual surface plasmons in cylinders. *Physical Review B*, *28*, 3173–3181.

Mathers, C. D., Fat, D. M., & Boerma, J. T. (2008). *The global burden of disease: 2004 update*. World Health Organization.

Mcdonnell, J. M. (2001). Surface plasmon resonance : towards an understanding of the, 572–577.

Meek, J. L. (1996). A brief history of the beginning of the finite element method. *International Journal for Numerical Methods in Engineering*, *39*, 3761–3774.

Mernagh, D. R., Janscak, P., Firman, K., & Kneale, G. G. (1998). Protein-Protein and Protein-DNA Interactions in the Type I. Restriction Endonuclease R. EcoR124I. *Biological Chemistry*, *379*(4-5), 497–504.

Mizutani, U. (2001). *Introduction to the electron theory of metals*. Cambridge University Press.

Mouvet, C., Harris, R. D., Maciag, C., Luff, B. J., Wilkinson, J. S., Piehler, J., … Ismail, G. (1997). Determination of simazine in water samples by waveguide surface plasmon resonance. *Analytica Chimica Acta*, *338*(1), 109–117.

Murray, N. E. A., Quam, M. B., & Wilder-Smith, A. (2013). Epidemiology of dengue: past, present and future prospects. *Clinical Epidemiology*, *5*, 299.

Naimushin, A. N., Soelberg, S. D., Nguyen, D. K., Dunlap, L., Bartholomew, D., Elkind, J., … Furlong, C. E. (2002). Detection of Staphylococcus aureus enterotoxin B at femtomolar levels with a miniature integrated two-channel surface plasmon resonance (SPR) sensor. *Biosensors & Bioelectronics*, *17*(6-7), 573–84.

Newton, R. G. (1982). *Scattering theory of waves and particles*. DoverPublications. com.

Novotny, L., & Hecht, B. (2012). *Principles of nano-optics*. Cambridge university press.

Nunes, M. R. T., Nunes Neto, J. P., Casseb, S. M. M., Nunes, K. N. B., Martins, L. C., Rodrigues, S. G., … Vasconcelos, P. F. C. (2011). Evaluation of an immunoglobulin M-specific capture enzyme-linked immunosorbent assay for rapid diagnosis of dengue infection. *Journal of Virological Methods*, *171*(1), 13–20.

Nylander, C., Liedberg, B., & Lind, T. (1983). Gas detection by means of surface plasmon resonance. *Sensors and Actuators*, *3*, 79–88.

Oliveira, L. C., Moreira, S., Thirstrup, C., Uwe, E., Melcher, K., Marcus, A., … Neff, H. (2013). A Surface Plasmon Resonance Biochip Wavelength Interrogation Modes, *62*(5), 1223–1232.

Ordal, M. A., Long, L. L., Bell, R. J., Bell, S. E., Bell, R. R., Alexander Jr, R. W., … others. (1983). Optical properties of the metals al, co, cu, au, fe, pb, ni, pd, pt, ag, ti, and w in the infrared and far infrared. *Applied Optics*, *22*(7), 1099–1119.

Organization, W. H., & others. (2011). Comprehensive guidelines for prevention and control of dengue and dengue haemorrhagic fever. *WHO Regional Publication SEARO*, (29).

Osman, O., Fong, M. Y., & Devi, S. (2007). Short Communication A Preliminary Study of Dengue Infection in Brunei, *60*, 205–208.

Otto, A. (1968). Excitation of nonradiative surface plasma waves in silver by the method of frustrated total reflection. *Zeitschrift F{ü}r Physik*, *216*(4), 398–410.

Palik, E. D. (1998). *Handbook of Optical Constants of Solids: Index* (Vol. 3). Access Online via Elsevier.

Peeling, R. W., Artsob, H., Pelegrino, J. L., Buchy, P., Cardosa, M. J., Devi, S., … others. (2010). Evaluation of diagnostic tests: dengue. *Nature Reviews Microbiology*, *8*, S30–S37.

Pfeiffer, C. A., Economou, E. N., & Ngai, K. L. (1974). Surface polaritons in a circularly cylindrical interface: surface plasmons. *Physical Review B*, *10*(8), 3038.

Piliarik, M., Sípová, H., Kvasnička, P., Galler, N., Krenn, J. R., & Homola, J. (2012). High-resolution biosensor based on localized surface plasmons. *Optics Express*, *20*(1), 672–80.

Pines, D. (1953). A collective description of electron interactions: IV. Electron interaction in metals. *Physical Review*, *92*(3), 626.

Pines, D., & Bohm, D. (1952). A collective description of electron interactions: II. Collective vs individual particle aspects of the interactions. *Physical Review*, *85*(2), 338.

Pockrand, I., Swalen, J. D., Gordon II, J. G., & Philpott, M. R. (1978). Surface plasmon spectroscopy of organic monolayer assemblies. *Surface Science*, *74*(1), 237–244.

Powell, C. J., & Swan, J. B. (1959). Origin of the characteristic electron energy losses in aluminum. *Physical Review*, *115*(4), 869.

Powell, C. J., & Swan, J. B. (1960). Effect of oxidation on the characteristic loss spectra of aluminum and magnesium. *Physical Review*, *118*(3), 640.

Prade, B., Vinet, J. Y., & Mysyrowicz, A. (1991). Guided optical waves in planar heterostructures with negative dielectric constant. *Phys. Rev. B*, *44*(24), 13556–13572.

Prasad, P. N. (2004). *Nanophotonics*. Wiley. com.

Qi, Z., Honma, I., & Zhou, H. (2006). Humidity sensor based on localized surface plasmon resonance of multilayer thin films of gold nanoparticles linked with myoglobin. *Optics Letters*, *31*(12), 1854–1856.

Quail, J. C., & Simon, H. J. (1984). Second-harmonic generation with phase-matched long-range and short-range surface plasmons. *Journal of Applied Physics*, *56*(9), 2589–2591.

Raether, H. (1988a). Surface plasmons on gratings. *Surface Plasmons on Smooth and Rough Surfaces and on Gratings*, 91–116.

Raether, H. (1988b). *Surface plasmons on smooth surfaces*. Springer.

Rakic, A. D., Djurisic, A. B., Elazar, J. M., & Majewski, M. L. (1998). Optical properties of metallic films for vertical-cavity optoelectronic devices. *Applied Optics*, *37*(22), 5271–83.

Ramirez, A. H., Moros, Z., Comach, G., Zambrano, J., Bravo, L., Pinto, B., … Liprandi, F. (2009). Evaluation of dengue NS1 antigen detection tests with acute sera from patients infected with dengue virus in Venezuela. *Diagnostic Microbiology and Infectious Disease*, *65*(3), 247–253.

Ranjit, S., & Kissoon, N. (2011). Dengue hemorrhagic fever and shock syndromes*. *Pediatric Critical Care Medicine*, *12*(1), 90–100.

Reichert, Inc. , Reichert Surface Plasmon Resonance (SPR) Systems. (2014).

Rigau-Pérez, J. G., Clark, G. G., Gubler, D. J., Reiter, P., Sanders, E. J., & Vance Vorndam, A. (1998). Dengue and dengue haemorrhagic fever. *The Lancet*, *352*(9132), 971–977.

Ritchie, R. H. (1957). Plasma losses by fast electrons in thin films. *Physical Review*, *106*(5), 874.

Rosenauer, A. (2003). *Transmission electron microscopy of semiconductor nanostructures: an analysis of composition and strain state* (Vol. 2403). Springer.

Ruiz, E. G., Garces, I., Aldea, C., Lopez, M. A., Mateo, J., Alonso-Chamarro, J., & Alegret, S. (1993). Industrial process sensor based on surface plasmon resonance (SPR) 1. Distillation process monitoring. *Sensors and Actuators A: Physical*, *37*, 221–225.

Sabatino, L., Botto, N., Borghini, A., Turchi, S., & Andreassi, M. G. (2013). Development of a new multiplex quantitative real-time PCR assay for the detection of the mtDNA4977 deletion in coronary artery disease patients: A link with telomere shortening. *Environmental and Molecular Mutagenesis*, *54*(5), 299–307.

Sadiku, M. N. O. (2010). *Numerical techniques in electromagnetics*. CRC press.

Sang, C. T., Hoon, L. S., Cuzzubbo, a, & Devine, P. (1998). Clinical evaluation of a rapid immunochromatographic test for the diagnosis of dengue virus infection. *Clinical and Diagnostic Laboratory Immunology*, *5*(3), 407–9.

Sang, C. T., Hoon, L. S., Cuzzubbo, A., & Devine, P. (1998). Clinical evaluation of a rapid immunochromatographic test for the diagnosis of dengue virus infection. *Clinical and Diagnostic Laboratory Immunology*, *5*(3), 407–409.

Schaller, J. K., Czepluch, R., & Stojanoff, C. G. (1997). Plasmon spectroscopy for high resolution angular measurements. In *Proc. SPIE* (Vol. 3098, pp. 476–486).

Schilling, S., Ludolfs, D., Van An, L., & Schmitz, H. (2004). Laboratory diagnosis of primary and secondary dengue infection. *Journal of Clinical Virology*, *31*(3), 179–184.

Schmidt, A. G., Lee, K., Yang, P. L., & Harrison, S. C. (2012). Small-molecule inhibitors of dengue-virus entry. *PLoS Pathogens*, *8*(4), e1002627.

Schulz, L. G. (1954). The optical constants of silver, gold, copper, and aluminum. I. The absorption coefficient k. *JOSA*, *44*(5), 357–362.

Schulz, L. G., & Tangherlini, F. R. (1954). Optical constants of silver, gold, copper, and aluminum. II. The index of refraction n. *JOSA*, *44*(5), 362–367.

Seydack, M. (2005). Nanoparticle labels in immunosensing using optical detection methods. *Biosensors and Bioelectronics*, *20*(12), 2454–2469.

Shalabney, A., & Abdulhalim, I. (2012). Figure-of-merit enhancement of surface plasmon resonance sensors in the spectral interrogation. *Optics Letters*, *37*(7), 1175–7.

Shalaev, V. M., & Kawata, S. (2006). *Nanophotonics with surface plasmons*. Elsevier.

Shamala, D. (2008). Dengue: Breakbone fever, hemorrhagia or shock. *JUMMEC*, *11*(2), 39–52.

Shamala, D. S. (2005). DENGUE AND DENGUE HAEMORRHAGIC FEVER IN MALAYSIA. *JUMMEC JUMMEC*, 11.

Sharma, A. K., Jha, R., & Gupta, B. D. (2007). Fiber-optic sensors based on surface plasmon resonance: a comprehensive review. *Sensors Journal, IEEE*, *7*(8), 1118–1129.

Shu, P.-Y., Chen, L.-K., Chang, S.-F., Yueh, Y.-Y., Chow, L., Chien, L.-J., … Huang, J.-H. (2003). Comparison of capture immunoglobulin M (IgM) and IgG enzyme-linked immunosorbent assay (ELISA) and nonstructural protein NS1 serotype-specific IgG ELISA for differentiation of primary and secondary dengue virus infections. *Clinical and Diagnostic Laboratory Immunology*, *10*(4), 622–630.

Shu, P.-Y., & Huang, J.-H. (2004). Current advances in dengue diagnosis. *Clinical and Diagnostic Laboratory Immunology*, *11*(4), 642–650.

Skullsinthestars. (2010). Optics basics: surface plasmons. Retrieved from http://skullsinthestars.com/2010/09/21/optics-basics-surface-plasmons/

Slavík, R., & Homola. (2007). Ultrahigh resolution long range surface plasmon-based sensor. *Sensors and Actuators B: Chemical*, *123*(1), 10–12.

Sólyom, J. (2010). *Fundamentals of the Physics of Solids: Volume 3-Normal, Broken-Symmetry, and Correlated Systems* (Vol. 3). Springer.

Sommerfeld, A. (1909). Propagation of waves in wireless telegraphy. *Ann. Phys*, *28*(3), 665–736.

Special Programme for Research, Training in Tropical Diseases, W. H. O. (2009). *Dengue: guidelines for diagnosis, treatment, prevention and control*. World Health Organization.

Stenzel, O., Wilbrandt, S., Stendal, A., Beckers, U., Voigtsberger, K., & Von Borczyskowski, C. (1995). The incorporation of metal clusters into thin organic dye layers as a method for producing strongly absorbing composite layers: an oscillator model approach to resonant metal cluster absorption. *Journal of Physics D: Applied Physics*, *28*(10), 2154.

Stern, E. A., & Ferrell, R. A. (1960). Surface plasma oscillations of a degenerate electron gas. *Physical Review*, *120*(1), 130.

Tanious, F. a, Nguyen, B., & Wilson, W. D. (2008). Biosensor-surface plasmon resonance methods for quantitative analysis of biomolecular interactions. *Methods in Cell Biology*, *84*(07), 53–77.

Turhan-Sayan, G., & others. (2003). Temperature effects on surface plasmon resonance: design considerations for an optical temperature sensor. *Journal of Lightwave Technology*, *21*(3), 805.

Vaughn, D. W., Nisalak, A., Kalayanarooj, S., Solomon, T., Dung, N. M., Cuzzubbo, A., & Devine, P. L. (1998). Evaluation of a rapid immunochromatographic test for diagnosis of dengue virus infection. *Journal of Clinical Microbiology*, *36*(1), 234–238.

Verma, R., Gupta, B. D., & Jha, R. (2011). Sensors and Actuators B : Chemical Sensitivity enhancement of a surface plasmon resonance based biomolecules sensor using graphene and silicon layers. *Sensors & Actuators: B. Chemical*, *160*(1), 623–631.

Vernon, K. C., Gramotnev, D. K., & Pile, D. F. P. (2007). Adiabatic nanofocusing of plasmons by a sharp metal wedge on a dielectric substrate. *Journal of Applied Physics*, *101*(10), 104312.

Vial, A. (2007). Implementation of the critical points model in the recursive convolution method for modelling dispersive media with the finite-difference time domain method. *Journal of Optics A: Pure and Applied Optics*, *9*(7), 745–748.

Vial, A., & Laroche, T. (2007). Description of dispersion properties of metals by means of the critical points model and application to the study of resonant structures using the FDTD method. *Journal of Physics D: Applied Physics*, *40*(22), 7152–7158.

Vo-Dinh, T. (2008). Nanobiosensing using plasmonic nanoprobes. *Selected Topics in Quantum Electronics, IEEE Journal of*, *14*(1), 198–205.

Vogel, M. W. (2009). Theoretical and numerical investigation of plasmon nanofocusing in metallic tapered rods and grooves.

Volakis, J. L., Chatterjee, A., & Kempel, L. C. (1998). *Finite Element Metheod For Electromagnetics*. Universities Press.

Wang, S. M., & Sekaran, S. D. (2010). Evaluation of a commercial SD dengue virus NS1 antigen capture enzyme-linked immunosorbent assay kit for early diagnosis of dengue virus infection. *Journal of Clinical Microbiology*, *48*(8), 2793–2797.

Watanabe, K. (2011). Model for measurement of water layer thickness under lipid bilayers by surface plasmon resonance. *Biomedical Optics Express*, *2*(5), 1115–20.

Weiss, M. N., Srivastava, R., & Groger, H. (1996). Experimental investigation of a surface plasmon-based integrated-optic humidity sensor. *Electronics Letters*, *32*(9), 842–843.

Wijaya, E., Lenaerts, C., Maricot, S., Hastanin, J., Habraken, S., Vilcot, J.-P., … Szunerits, S. (2011). Surface plasmon resonance-based biosensors: From the development of different SPR structures to novel surface functionalization strategies. *Current Opinion in Solid State and Materials Science*, *15*(5), 208–224.

Wood, R. W. (1902). XLII. On a remarkable case of uneven distribution of light in a diffraction grating spectrum. *The London, Edinburgh, and Dublin Philosophical Magazine and Journal of Science*, *4*(21), 396–402.

Xu, J., Wan, J., Yang, S., Zhang, S., Xu, N., Li, N., … Liu, W. (2012). A surface plasmon resonance biosensor for direct detection of the rabies virus. *Acta Veterinaria Brno*, *81*(2), 107–111.

Yager, P., Domingo, G. J., & Gerdes, J. (2008). Point-of-care diagnostics for global health. *Annu. Rev. Biomed. Eng.*, *10*, 107–144.

Yamamoto, M. (2008). Surface Plasmon Resonance (SPR) Theory : Tutorial.

Yonzon, C. R., Jeoung, E., Zou, S., Schatz, G. C., Mrksich, M., & Van Duyne, R. P. (2004). A comparative analysis of localized and propagating surface plasmon resonance sensors: the binding of concanavalin A to a monosaccharide functionalized self-assembled monolayer. *Journal of the American Chemical Society*, *126*(39), 12669–12676.

Young, P. R., Hilditch, P. a, Bletchly, C., & Halloran, W. (2000). An antigen capture enzyme-linked immunosorbent assay reveals high levels of the dengue virus protein NS1 in the sera of infected patients. *Journal of Clinical Microbiology*, *38*(3), 1053–7.

Zayats, A. V., Smolyaninov, I. I., & Maradudin, A. a. (2005). Nano-optics of surface plasmon polaritons. *Physics Reports*, *408*(3-4), 131–314.

Zenneck, J. (1907). Propagation of plane EM waves along a plane conducting surface. *Ann. Phys.(Leipzig)*, *23*(1), 907.

Zhou, C., Friedt, J.-M., Angelova, A., Choi, K.-H., Laureyn, W., Frederix, F., … Borghs, G. (2004). Human immunoglobulin adsorption investigated by means of quartz crystal microbalance dissipation, atomic force microscopy, surface acoustic wave, and surface plasmon resonance techniques. *Langmuir*, *20*(14), 5870–5878.

Ziegel, E., Press, W., Flannery, B., Teukolsky, S., & Vetterling, W. (1987). *Numerical Recipes: The Art of Scientific Computing*. *Technometrics* (Vol. 29, p. 501).

Zourob, M., & Lakhtakia, A. (2010). *Optical Guided-wave Chemical and Biosensors: I* (Vol. 1). Springer.